

1 **Interleukin-1 prevents SARS-CoV-2-induced membrane fusion to**
2 **restrict viral transmission via induction of actin bundles**

3 Xu Zheng^{1,#}, Shi Yu^{1,#,\$}, Yanqiu Zhou^{2,#}, Kuai Yu^{3,#}, Yuhui Gao¹, Mengdan Chen¹, Dong Duan^{1,4},
4 Yunyi Li², Xiaoxian Cui², Jiabin Mou², Yuying Yang², Xun Wang⁵, Min Chen^{2,*}, Yaming Jiu^{1,*},
5 Jincun Zhao^{3,*}, Guangxun Meng^{1,4,*}

6 ¹The Center for Microbes, Development and Health, Key Laboratory of Immune Response and
7 Immunotherapy, Shanghai Institute of Immunity and Infection, Chinese Academy of Sciences,
8 University of Chinese Academy of Sciences, Shanghai, 200031, China.

9 ²Shanghai Municipal Center for Disease Control and Prevention, Shanghai, 200336, China.

10 ³The First Affiliated Hospital of Guangzhou Medical University, State Key Laboratory of
11 Respiratory Disease, National Clinical Research Center for Respiratory Disease, Guangzhou
12 Institute of Respiratory Health, Guangzhou, 510182, China.

13 ⁴Pasteurien College, Soochow University, Suzhou, Jiangsu, 215006, China.

14 ⁵Shanghai Blood Center, Shanghai, 200051, China.

15 *Corresponding author. Email: Guangxun Meng, gxmeng@ips.ac.cn; Jincun Zhao,
16 zhaojincun@gird.cn; Yaming Jiu, ymjiu@ips.ac.cn; Min Chen, chenmin@scdc.sh.cn

17 #Authors contributed equally

18 ^{\$}Present address: Guangzhou National Laboratory, Guangzhou International Bio Island,
19 Guangzhou, Guangdong, 510005, China.

20 **Author Contributions:** Conceptualization, X.Z., S.Y. and G.M.; Methodology, X.Z., S.Y., Y.J.
21 and G.M.; Investigation, X.Z., S.Y., Y.Z., K.Y., Y.G., Me.C., D.D., Y.L., J.M., X.C., Y.Y., X.W., Y.J.
22 and J.Z.; Writing – Original Draft, X.Z., S.Y.; Writing – Review & Editing, X.Z., S.Y., Y.J. and
23 G.M.; Funding Acquisition, Y.Z., Y.J., M.C. J.Z and G.M.; Resources, Y.J., M.C. J.Z and G.M.;
24 Supervision, G.M.

25 **Competing Interest Statement:** Authors declare that they have no competing interests.

26 **Keywords:** SARS-CoV-2, innate immune cell, Interlukin-1, cell-cell fusion, actin bundle.

27 **Abstract**

28 Innate immune responses triggered by severe acute respiratory syndrome coronavirus 2 (SARS-
29 CoV-2) infection play pivotal roles in the pathogenesis of COVID-19, while host factors including
30 pro-inflammatory cytokines are critical for viral containment. By utilizing quantitative and
31 qualitative models, we discovered that soluble factors secreted by human monocytes potently
32 inhibit SARS-CoV-2-induced cell-cell fusion in viral-infected cells. Through cytokine screening, we
33 identified that interleukin-1 β (IL-1 β), a key mediator of inflammation, inhibits syncytia formation
34 mediated by various SARS-CoV-2 strains. Mechanistically, IL-1 β activates RhoA/ROCK signaling
35 through a non-canonical IL-1 receptor-dependent pathway, which drives the enrichment of actin
36 bundles at the cell-cell junctions, thus prevents syncytia formation. Notably, *in vivo* infection
37 experiments in mice confirms that IL-1 β significantly restricted SARS-CoV-2 spreading in the lung
38 epithelia. Together, by revealing the function and underlying mechanism of IL-1 β on SARS-CoV-
39 2-induced cell-cell fusion, our study highlights an unprecedented antiviral function for cytokines
40 during viral infection.

41 **Main Text**

42

43 **Introduction**

44 The COVID-19 pandemic caused by severe acute respiratory syndrome coronavirus 2 (SARS-
45 CoV-2) infection has spread globally, with at least 755 million people diagnosed and the death toll
46 is over 6.8 million. SARS-CoV-2 variants of concern, including Alpha, Beta, Delta, and Omicron,
47 continue to evolve and increase transmissibility and the ability to escape host immune responses.
48 These variants have brought huge challenges to the design and development of vaccines and
49 therapeutic reagents (Zhou et al., 2020). In order to discover novel strategies to control the virus,
50 it is important to understand host responses to SARS-CoV-2 infection.

51 SARS-CoV-2 infection induces cell-cell fusion (also known as syncytia formation) in multiple cell
52 types including lung epithelial cells, neurons and glia (Martínez-Mármol et al., 2023). Syncytia of
53 SARS-CoV-2 infected cells with neighboring cells could potentially contribute to increased viral
54 transmission and pathogenicity in the infected host (Rajah, Bernier, Buchrieser, & Schwartz,
55 2022), which also makes the virus insensitive to extracellular neutralizing antibodies (Li et al.,
56 2022; Yu et al., 2023). Moreover, syncytia formation among pneumocytes with long-term
57 persistence of viral RNA has been observed in the lung autopsy of deceased COVID-19 donors,
58 which may contribute to prolonged clearance of the virus and long COVID symptoms (Bussani et
59 al., 2020). Therefore, inhibiting syncytia formation is critical to ensure viral clearance and to
60 control viral transmission.

61 It has been reported that SARS-CoV-2 mediated syncytia formation is effectively inhibited by
62 multiple interferon (IFN)-stimulating genes (ISGs) (Pfaender et al., 2020; Wang et al., 2020).
63 However, low IFN levels with impaired ISG responses were observed during early SARS-CoV-2
64 infection, which may have compromised the antiviral responses of IFN in severe COVID-19
65 patients (Blanco-Melo et al., 2020; Hadjadj et al., 2020). Thus, identifying other endogenous host
66 factors that regulate syncytia formation is of great significance for harnessing the transmission of
67 SARS-CoV-2.

68 Of note, a variety of cells are involved in the host responses to SARS-CoV-2 infection (Ren et al.,
69 2021). Lung epithelial cells are the primary target of SARS-CoV-2 infection and transmission,
70 which subsequently recruit and activate innate immune cells, leading to COVID-19 pathology
71 (Barnett et al., 2023). In such process, tissue-resident macrophages and circulating monocytes
72 contribute to local and systemic inflammation largely through releasing inflammatory cytokines
73 (Sefik et al., 2022). Among these cytokines induced by SARS-CoV-2, the combination of TNF- α
74 and IFN- γ induces inflammatory cell death, resulting in clear tissue damage, while other cytokines'
75 function remains obscure (Karki et al., 2021). In addition, when corticosteroids were applied to
76 suppress the inflammatory response in patients infected by SARS-CoV (N. Lee et al., 2004) or
77 MERS-CoV (Arabi et al., 2018), the clearance of viral RNA was obviously delayed, suggesting the
78 importance of innate immune factors in viral clearance.

79 Innate immune cells express toll-like receptors (TLRs), and TLR-mediated signaling induces
80 robust production of inflammatory cytokines (Medzhitov, 2001). In the current work, we screened
81 the role of soluble pro-inflammatory cytokines on the SARS-CoV-2 spike-induced cell-cell fusion.
82 Notably, we identified that IL-1 β , which is the key factor of inflammatory response, inhibited
83 SARS-CoV-2 spike-induced syncytia formation in various cells by activating RhoA/ROCK
84 pathway to initiate actin bundle formation at cell-cell interface between SARS-CoV-2 infected
85 cells and neighboring cells. Importantly, IL-1 β significantly reduced SARS-CoV-2 transmission
86 among lung epithelia in experimental mice *in vivo*. Therefore, our data highlight an important role
87 for pro-inflammatory cytokines against viral infection.

88 Results

89 Host factors secreted by activated innate immune cells inhibit SARS-CoV-2-induced cell- 90 cell fusion

91 We have previously established quantitative and qualitative models for SARS-CoV-2 spike-
92 induced cell-cell fusion by bioluminescence assay, immunoblotting and fluorescence imaging (Yu
93 et al., 2022). In order to explore the potential effect of cytokines on SARS-CoV-2-induced cell-cell
94 fusion, human monocyte cell line THP-1 and human peripheral blood mononuclear cells (PBMCs)
95 were used in this study. We applied several TLR ligands to stimulate such innate immune cells
96 and collected the cell culture supernatants for subsequent experiments (**Figure 1A**). Of note, cell
97 culture supernatants of THP-1 cells stimulated by TLR ligands significantly reduced the
98 bioluminescence signal, while neither untreated THP-1 cell culture supernatant nor the medium
99 control had any effect on the bioluminescence signal reflecting cell-cell fusion (**Figure 1B**).
100 SARS-CoV-2 spike engagement of ACE2 primed the cleavage of S2' fragment in target cells, a
101 key proteolytic event coupled with spike-mediated membrane fusion (Yu et al., 2022). In parallel
102 with bioluminescence assay, a large amount of enriched S2' cleavage was detected in HEK293T-
103 Spike and HEK293T-ACE2 co-cultured group and co-culture incubated with untreated THP-1 cell
104 culture supernatant, while S2' cleavage was clearly reduced upon treatment with TLR ligands-
105 stimulated THP-1 cell culture supernatants (**Figure 1C**). Syncytia formation was also visualized
106 using cells co-expressing spike and a ZsGreen fluorescent reporter. The area of syncytium were
107 significantly reduced by the treatment with TLR ligands-stimulated THP-1 cell culture
108 supernatants (**Figure 1D and Figure 1—figure supplement 1A**). Considering the presence of
109 TLR ligands in such cell culture supernatants, we tested their potential direct effects. As expected,
110 TLR ligands alone did not reduce the bioluminescence signal and S2' cleavage compared to the
111 control groups, as well as no effect on syncytia formation (**Figure 1—figure supplement 1B-E**).

112 Concurrently, we also tested the effect of PBMCs culture supernatants on SARS-CoV-2 spike-
113 induced cell-cell fusion. Consistent with the results from THP-1 cells, TLR ligands stimulated
114 PBMCs culture supernatants treatment also strongly reduced the bioluminescence signal, S2'
115 cleavage, and the area of syncytium compared with the medium group (**Figure 1—figure
116 supplement 1F-I**). These results thus suggested that activated innate immune cells released
117 host factors to inhibit SARS-CoV-2 spike-induced cell-cell fusion.

118 To validate the effect of innate immune cell culture supernatants on cell-cell fusion in authentic
119 SARS-CoV-2 infection, we pre-treated ACE2-expressing cells with THP-1 cell culture
120 supernatants before inoculation with SARS-CoV-2 B.1.617.2 (Delta) or wild type (WT) strains.
121 Cell lysates were used for the detection of SARS-CoV-2 spike and N protein 24 hours post
122 infection (hpi) (**Figure 1E**). Result of this experiment revealed that TLR ligands-stimulated-THP-1
123 cell culture supernatants reduced S2' cleavage and N protein during Delta or WT SARS-CoV-2
124 infection in HEK293T-ACE2 cells, while untreated THP-1 cell culture supernatant had no effect
125 (**Figure 1F and Figure 1—figure supplement 2A**). In addition, TLR ligands-stimulated-THP-1
126 cell culture supernatants reduced the area of syncytium induced by Delta or WT SARS-CoV-2
127 infection (**Figure 1—figure supplement 2B and C**). Furthermore, we infected the human colon
128 epithelial carcinoma cell line Caco-2 with WT SARS-CoV-2, and found that S2' cleavage and N
129 protein were reduced after TLR ligands-stimulated-THP-1 cell culture supernatants pre-treatment
130 (**Figure 1G**). Accordingly, immunofluorescent staining also showed that TLR ligands-stimulated-
131 THP-1 cell culture supernatants significantly reduced the area of syncytium during SARS-CoV-2
132 infection in Caco-2 cells (**Figure 1H and I**). Therefore, these data suggested that host factors
133 secreted by activated innate immune cells inhibit authentic SARS-CoV-2 induced cell-cell fusion.

134 **IL-1 β inhibits SARS-CoV-2-induced cell-cell fusion**

135 To explore which host factor(s) inhibited SARS-CoV-2 induced cell-cell fusion, we first detected
136 mRNA levels of different cytokines in THP-1 cells stimulated by TLR ligands. It was found that the
137 expression levels of *IL1A*, *IL1B*, *IL6* and *IL8* were significantly increased upon TLR ligands
138 stimulation, while *IL4*, *IL12A*, *IFNA1*, *IFNB1* and *IFNG* mRNA levels were not changed or
139 undetected (**Figure 2—figure supplement 1A**). In addition, we also detected the mRNA levels of
140 cytokine receptors in HEK293T modelling cells, confirming that *IL1R1*, *IL4R*, *IL6ST*, *IL8RA*,
141 *IFNAR1*, *IFNGR1* were expressed in such cells, while *IL2RA* and *IL12RB1* were undetectable
142 (**Figure 2—figure supplement 1B**).

143 We next selected recombinant IL-1 α , IL-1 β , IL-6, and IL-8 to test whether individual cytokine may
144 play a role in affecting SARS-CoV-2 spike induced cell-cell fusion (**Figure 2A**). Interestingly, IL-
145 1 α and IL-1 β significantly reduced the bioluminescence signal compared to the control group,
146 while IL-6 and IL-8 had little or no effect (**Figure 2B**). In addition, fluorescence images of cells
147 expressing ZsGreen reporter also confirmed that IL-1 α and IL-1 β significantly inhibited SARS-
148 CoV-2 spike induced syncytia formation (**Figure 2—figure supplement 1C and D**). Furthermore,
149 IL-1 β and IL-1 α both reduced the bioluminescence signal and S2' cleavage (**Figure 2 C and D**,
150 **and Figure 2—figure supplement 2A**) in cell lysates in a dose-dependent manner. Moreover,
151 the syncytia formation was inhibited with increasing concentrations of IL-1 β or IL-1 α (**Figure 2—**
152 **figure supplement 2B-E**). Intriguingly, when we added both IL-1 α and IL-1 β , there was no
153 synergistic inhibition on cell-cell fusion compared to either cytokine alone (**Figure 2—figure**
154 **supplement 2F-H**), suggesting a saturation of IL-1 receptor binding to these homologues. Since
155 both IL-1 α and IL-1 β activate the downstream pathway through the same receptor IL-1R1, these
156 data suggested that IL-1 α or IL-1 β may inhibit cell-cell fusion through the same pathway.
157 Considering the higher mRNA level of *IL1B* than *IL1A*, as well as the classical release pathway of
158 IL-1 β from innate immune cells (Weber, Wasiliew, & Kracht, 2010), we applied IL-1 β for further
159 experiments.

160 In order to validate the effect of IL-1 β on cell-cell fusion during authentic SARS-CoV-2 infection,
161 we pre-treated ACE2-expressing cells with IL-1 β before inoculating Delta or WT authentic SARS-
162 CoV-2. Cell lysates were used for the detection of SARS-CoV-2 spike and N protein 24 hpi
163 (**Figure 2E**). To this end, it was found that IL-1 β reduced S2' cleavage and N protein compared to
164 the control group during such infection both in HEK293T-ACE2 (**Figure 2F and Figure 2—figure**
165 **supplement 3A**) and Caco-2 cells (**Figure 2G**). Meanwhile, IL-1 β inhibited authentic SARS-CoV-
166 2 induced syncytia formation (**Figure 2H and I, and Figure 2—figure supplement 3B and C**).
167 Thus, these results verified that IL-1 β inhibits authentic SARS-CoV-2 induced cell-cell fusion in
168 various target cells.

169 As expected, innate immune cells activated by TLR ligands secreted IL-1 β into the cell culture
170 supernatants (**Figure 2—figure supplement 4A and B**). We employed IL-1 receptor antagonist
171 (IL-1RA) to block IL-1 receptor on target cells, and found that IL-1RA treatment reduced the
172 inhibitory effect of PGN-stimulated-THP-1 cell culture supernatant on cell-cell fusion (**Figure 2J**
173 **and Figure 2—figure supplement 4C**). With another note, TLR2 was essential for THP-1 cells
174 to release IL-1 β in response to TLR2 ligands (**Figure 2—figure supplement 4D**). More
175 importantly, the cell culture supernatants of TLR2-knockout THP-1 cells stimulated by TLR2
176 Ligands had no effect on the bioluminescence signal, while the cell culture supernatants from WT
177 THP-1 cells stimulated by the same TLR2 Ligands significantly reduced the bioluminescence
178 signal (**Figure 2—figure supplement 4E**). In addition, pre-treatment with TAK1 inhibitor (5Z-7) or
179 IKK β inhibitor (TPCA1) in WT THP-1 cells prevented IL-1 β secretion after PGN stimulation
180 (**Figure 2—figure supplement 4F**), as well as eliminated the inhibitory effect of PGN-stimulated
181 WT THP-1 cell culture supernatant on SARS-CoV-2 spike-induced cell-cell fusion (**Figure 2—**
182 **figure supplement 4G**). In parallel, pre-treatment with these inhibitors in PBMCs showed the

183 same results (**Figure 2—figure supplement 4H and I**). These data suggested that TLR-
184 knockout or inhibitors targeting the respective TLR signaling prevented innate immune cells from
185 releasing IL-1 β into supernatants, which led to failed inhibition of SARS-CoV-2 spike induced cell-
186 cell fusion. These findings thus further verify that IL-1 β is an important host factor inhibiting
187 SARS-CoV-2 induced cell-cell fusion.

188 To investigate the effector function of IL-1 on cells expressing SARS-CoV-2 spike (donor cells)
189 and neighboring cells expressing ACE2 (acceptor cells), we pre-treated HEK293T-S or
190 HEK293T-ACE2 cells or both with IL-1 β , then co-cultured after washing with PBS; cells were then
191 analyzed by the quantitative and qualitative models (**Figure 2—figure supplement 5A**). Notably,
192 pre-treatment of either HEK293T-S or HEK293T-ACE2 cells with IL-1 β alone reduced
193 bioluminescence signal and S2' cleavage; when IL-1 β pre-treatment on both HEK293T-S and
194 HEK293T-ACE2 cells was applied, bioluminescence signal and S2' cleavage were further
195 reduced (**Figure 2—figure supplement 5B**). Furthermore, we also applied Vero E6-
196 overexpressing ACE2 cell line (Vero E6-ACE2) and human Calu-3 cells as acceptor cells; and
197 found that pre-treatment of either HEK293T-S or Vero E6-ACE2 cells with IL-1 β alone reduced
198 part of S2' cleavage, while IL-1 β pre-treatment of both HEK293T-S and Vero E6-ACE2 cells led
199 to further reduction of S2' cleavage (**Figure 2—figure supplement 5C**), and the same results
200 were observed in the case of Calu-3 as acceptor cells (**Figure 2—figure supplement 5D**).
201 Accordingly, fluorescence imaging also showed that IL-1 β significantly reduced the area of
202 syncytia (**Figure 2—figure supplement 6A and B**). Notably, IL-1 β reduced the bioluminescence
203 signal and S2' cleavage in different SARS-CoV-2 variants (**Figure 2—figure supplement 6C-E**).
204 Therefore, these results suggest that IL-1 β acts on both donor and acceptor cells to inhibit SARS-
205 CoV-2 spike-induced cell-cell fusion in various cell lines.

206 Of note, SARS-CoV (Belouzard, Chu, & Whittaker, 2009) and MERS-CoV (Straus et al., 2020)
207 spike proteins also induce cell-cell fusion in target cells. Therefore, we further explored whether
208 IL-1 β was also able to inhibit SARS-CoV and MERS-CoV spike-induced cell-cell fusion in ACE2-
209 or Dipeptidyl peptidase-4 (DPP4)-expressing cells by bioluminescence assay, immunoblotting
210 and a modified *stop-mCherry* fluorescent model, wherein mCherry reporter is only expressed
211 when Cre excises the Stop cassette inside the fused syncytia (**Figure 2—figure supplement 7A**).
212 Similar to SARS-CoV-2 spike-induced cell-cell fusion, IL-1 β also reduced bioluminescence signal
213 (**Figure 2—figure supplement 7B and C**), S2' cleavage (**Figure 2—figure supplement 7D and**
214 **E**) and the area of syncytium (**Figure 2—figure supplement 7F and G**) in these cell-cell fusion
215 systems. Thus, IL-1 β possesses a broad spectrum to inhibit cell-cell fusion induced by different
216 coronaviruses.

217 **IL-1 β inhibits SARS-CoV-2-induced cell-cell fusion through IL-1R1/MyD88/IRAK/TRAF6** 218 **pathway**

219 To investigate the mechanism of IL-1 β inhibition on SARS-CoV-2 induced cell-cell fusion, we
220 performed gene knockout using CRISPR-Cas9 technology, in conjunction with inhibitors targeting
221 the IL-1 receptor pathway (**Figure 3A**). First of all, in the presence of IL-1RA, IL-1 β was unable to
222 reduce bioluminescence signal and S2' cleavage (**Figure 3B**). Next, as MyD88 is the
223 downstream adaptor for IL-1R1, we generated MyD88 knockout HEK293T cell line, wherein IL-1 β
224 was unable to reduce bioluminescence signal (**Figure 3C**) and S2' cleavage (**Figure 3—figure**
225 **supplement 1A**). In addition, we found that IL-1 β was unable to reduce bioluminescence signal
226 and S2' cleavage in the presence of IRAK1/4 inhibitor (**Figure 3D**). Furthermore, IL-1 β was
227 unable to reduce bioluminescence signal (**Figure 3E**) and S2' cleavage (**Figure 3—figure**
228 **supplement 1B**) in TRAF6 knockout HEK293T cell line. These results suggested that IL-1 β
229 inhibits SARS-CoV-2 spike induced cell-cell fusion through IL-1R1-MyD88-IRAK-TRAF6 pathway.

230 Intriguingly, when we tested TAK1, a downstream molecule of TRAF6 for the potential
231 involvement in the signaling, it was found that IL-1 β still reduced bioluminescence signal and S2'
232 cleavage in TAK1 knockout (sgMAP3K7) HEK293T cell line (**Figure 3—figure supplement 2A**).

233 Moreover, we found that in the presence of TPCA1, an IKK β inhibitor, IL-1 β still inhibited
234 bioluminescence signal and S2' cleavage as well (**Figure 3—figure supplement 2B**). In addition,
235 although IL-1 β upregulated the mRNA transcription levels of NF- κ B pathway-related genes, such
236 as *RELB*, *NFKBIA*, and *NFKB1* (**Figure 3—figure supplement 2C**), IL-1 β still reduced the
237 bioluminescence signal after these NF- κ B pathway-related genes knockout (**Figure 3—figure**
238 **supplement 2D**). Taken together, these results demonstrated that IL-1 β inhibits SARS-CoV-2
239 spike induced cell-cell fusion independent from the TAK1-IKK β -NF- κ B signaling cascade.

240 Furthermore, we validated these findings in authentic SARS-CoV-2 infected Caco-2 and Calu-3
241 cells. Consist with the results from HEK293T cells, IL-1 β failed to reduce S2' cleavage and N
242 protein in the presence of IRAK1/4 inhibitor, whereas it still reduced S2' cleavage and N protein in
243 the presence of the IKK β inhibitor TPCA1 in Caco-2 (**Figure 3F**) and Calu-3 cells (**Figure 3G**).

244 **IL-1 β inhibits SARS-CoV-2-induced cell-cell fusion through RhoA/ROCK mediated actin** 245 **bundle formation at the cell-cell junction**

246 It has been reported that IL-1 β activates RhoA signaling via MyD88 and IRAK, which is a
247 pathway independent from IKK β (Chen, Zuraw, Liu, Huang, & Pan, 2002). As a major
248 downstream effector of RhoA, ROCK phosphorylates substrates that are involved in the
249 regulation of the actin cytoskeleton, cell attachment, and cell motility (Riento & Ridley, 2003).
250 Therefore, we set out to detect the active level of RhoA through pull-down assay. To this end, we
251 verified that IL-1 β activated RhoA signaling in sgControl HEK293T cells but not in sgMyD88- or
252 sgTRAF6-HEK293T cells (**Figure 4A**). To directly visualize the distribution of endogenous GTP-
253 RhoA (active RhoA), we used a location biosensor derived from the carboxy terminus of anillin
254 (GFP-AHPH) (Priya et al., 2015; Sun et al., 2015). Interestingly, IL-1 β significantly increased the
255 fluorescence intensity of GFP-AHPH in sgControl HEK293T cells, but had no effect in sgMyD88-
256 and sgTRAF6-HEK293T cells (**Figure 4 B and C**).

257 To investigate whether IL-1 β inhibits SARS-CoV-2 spike-induced cell-cell fusion through the
258 RhoA/ROCK pathway, we co-transfected GFP-AHPH in ACE2-expressing cells, then co-cultured
259 with S-expressing cells at different time points. In the process of syncytia formation, cell-cell
260 contact established between S-expressing cells and ACE2-expressing cells, and GFP-AHPH
261 localized distally from cell-cell junction in the early stage of syncytia formation. With the
262 enlargement of syncytium, GFP-AHPH is visualized at the periphery of syncytium (**Figure 4D, top**
263 **panel and Figure 4—figure supplement 1A**). However, in IL-1 β treated group, GFP-AHPH foci
264 is enriched to the cell-cell junction in the early stage. Over time, GFP-AHPH was recruited more
265 to the cell-cell junction between S-expressing cells and ACE2-expressing cells, preventing further
266 cell-cell fusion (**Figure 4D, bottom panel and Figure 4—figure supplement 1B**). Cartoon
267 schematics inserted in the imaging data illustrate such findings in a modeled manner.

268 It has been reported that RhoA initiates actin arc formation (Dupraz et al., 2019; Stern et al.,
269 2021), so we further explored the changes of actin cytoskeleton during SARS-CoV-2 spike-
270 induced cell-cell fusion. We co-transfected constitutively activated RhoA L63 (Nobes & Hall,
271 1999) (RhoA-CA) plasmid with spike or ACE2 in HEK293T cells, and found that constitutive
272 activation of RhoA enriches actin filaments (F-actin) at cell-cell junction (**Figure 4E and Figure**
273 **4—figure supplement 2A**) and clearly reduces the bioluminescence signal and S2' cleavage in a
274 dose-dependent manner (**Figure 4—figure supplement 2B**). Moreover, we observed that F-
275 actin at cell-cell junction between S-expressing cells and ACE2-expressing cells was gradually
276 disappeared along with cell-cell fusion in the early stages of syncytia formation. With the
277 formation and enlargement of syncytium, F-actin of syncytium is preferably distributed
278 peripherally (**Figure 4F, top panel and Figure 4—figure supplement 2C**). However, IL-1 β
279 activated RhoA to initiate actin bundles formation at cell-cell junction, the formation of these actin
280 bundles potentially generates barriers and prevents membrane fusion between S-expressing cells
281 and ACE2-expressing cells. Even with the prolonged co-culture time, IL-1 β -induced actin bundles
282 formed at cell junctions consistently inhibited further syncytia formation (**Figure 4F, middle panel**

283 **and Figure 4—figure supplement 2D)**. Of note, ROCK inhibitor Y-27632 prevents the formation
284 of actin bundles (van der Heijden et al., 2008; Watanabe, Kato, Fujita, Ishizaki, & Narumiya,
285 1999). Here, we found that the ROCK inhibitor Y-27632 treatment prevented the formation of IL-
286 1 β -induced actin bundles at cell-cell junctions, thus promoted membrane fusion and cytoplasmic
287 exchange between S-expressing cells and ACE2-expressing cells and restored syncytia
288 formation (**Figure 4F, bottom panel and Figure 4—figure supplement 3A**).

289 Importantly, upon authentic SARS-CoV-2 infection, we observed consistent results:
290 immunofluorescence staining showed GFP-AHPH moving to the opposite of cell-cell junction and
291 located peripherally with syncytia formation (**Figure 5A, top panel and Figure 5—figure
292 supplement 1A**), while upon IL-1 β treatment, GFP-AHPH located to the cell-cell junction of
293 infected cells and neighboring cells (**Figure 5A, bottom panel and Figure 5—figure
294 supplement 1B**). In parallel, staining results showed that F-actin at the cell-cell junction were
295 disassembled during authentic SARS-CoV-2 infection; with the formation of syncytium, F-actin
296 was mainly distributed peripherally. However, actin bundles formed at cell-cell junction upon IL-1 β
297 inhibition of membrane fusion and further syncytia formation (**Figure 5B and Figure 5—figure
298 supplement 1C-E**). Together, these data revealed that IL-1 β induced the formation of actin
299 bundles at the cell-cell junction of SARS-CoV-2 infected cells and neighboring cells through
300 RhoA/ROCK pathway, which inhibited SARS-CoV-2 induced cell-cell fusion.

301 To further investigate the role of RhoA/ROCK pathway in inhibiting SARS-CoV-2 induced cell-cell
302 fusion, we found that HEK293T-ACE2 (**Figure 5C**), Caco-2 (**Figure 5—figure supplement 2A**)
303 and Calu-3 cells (**Figure 5D**) expressing RhoA-CA clearly reduced S2' cleavage and N protein
304 compared to the control group during authentic SARS-CoV-2 infection. Meanwhile, we observed
305 that constitutive activation of RhoA enriches actin bundles at cell-cell junction, thus preventing
306 SARS-CoV-2 induced cell-cell fusion in authentic SARS-CoV-2 infected Caco-2 (**Figure 5—
307 figure supplement 2B and C**) and Calu-3 cells (**Figure 5E and Figure 5—figure supplement
308 2D**). In addition, we examined the potential effect of RhoA-CA on ACE2 and found that it did not
309 affect Spike protein binding to ACE2 (**Figure 5—figure supplement 2E**), nor ACE2 distribution
310 on the cell surface (**Figure 5—figure supplement 2F and G**). We also observed that IL-1 β
311 treatment did not change ACE2 or Spike protein distribution on the cell surface (**Figure 5—figure
312 supplement 3A-D**).

313 Notably, ROCK inhibitor Y-27632 treatment increased bioluminescence signal and S2' cleavage
314 in a dose-dependent manner, promoting syncytia formation. When treated with lower
315 concentrations of Y-27632, IL-1 β eliminated Y-27632-enhanced cell-cell fusion. However, IL-1 β
316 was unable to inhibit cell-cell fusion in the presence of higher concentrations of Y-27632 (**Figure
317 5—figure supplement 3E**). Furthermore, we verified that IL-1 β was unable to reduce S2'
318 cleavage and N protein in the presence of Y-27632 in authentic SARS-CoV-2 infected Caco-2
319 (**Figure 5—figure supplement 3F**), Calu-3 cells (**Figure 5F**) and primary human lung cells
320 (**Figure 5G**). Immunofluorescence results also confirmed that the elimination of IL-1 β induced
321 actin bundles by Y-27632 in Caco-2 (**Figure 5—figure supplement 3G and 4A**) and Calu-3 cells
322 (**Figure 5H and Figure 5—figure supplement 4B**). These results indicated that preventing the
323 formation of RhoA/ROCK mediated actin bundles at cell-cell junction promotes SARS-CoV-2
324 induced cell-cell fusion.

325 **IL-1 β restricts SARS-CoV-2 transmission via induction of actin bundles *in vivo***

326 To demonstrate the role of IL-1 β in controlling SARS-CoV-2 transmission *in vivo*, BALB/c mice
327 were infected with authentic SARS-CoV-2 B.1.351 after IL-1 β or IL-1RA+IL-1 β pre-treatment
328 (**Figure 6—figure supplement 1A**). Interestingly, the results of this experiment showed that in
329 mice with IL-1 β treatment, the body weight loss was less than in the PBS control group, while IL-
330 1 β was unable to improve body weight in the presence of IL-1RA (**Figure 6—figure supplement
331 1B**). According to hematoxylin and eosin (H&E) staining, tissue histopathology analysis
332 demonstrated that the mice with IL-1 β treatment carry less pulmonary injury compared to the

333 PBS control and IL-1RA+IL-1 β groups (**Figure 6 A and B**). In addition, the expression level of
334 SARS-CoV-2 N gene in the lung from IL-1 β -treated mice was significantly lower than in the PBS
335 control and IL-1RA+IL-1 β -treated mice (**Figure 6C**). In addition, immunohistochemistry staining
336 showed that the infected area in the epithelial linings of lung tissue was significantly reduced by
337 IL-1 β treatment compared to the PBS control and IL-1RA+IL-1 β groups (**Figure 6 D and E**),
338 indicating that IL-1 β restricted the transmission of SARS-CoV-2 in the lung. Moreover,
339 fluorescence staining showed that SARS-CoV-2 infected lung epithelial cells fused with
340 neighboring cells, promoting viral transmission in the airway epithelial cells, while IL-1 β induced
341 the formation of actin bundles to restrict the syncytia formation and further viral transmission
342 (**Figure 6F and Figure 6—figure supplement 1C and D**). In addition, we found that IL-1 β -
343 treated mice have no significant changes in body weight, nor liver and spleen weight compared to
344 control mice (**Figure 6—figure supplement 2A-D**), indicating that this dose of IL-1 β did not
345 cause toxicity *in vivo* in the mice. Of note, when we isolated tissue cells from the IL-1 β -treated
346 mice and infected with authentic SARS-CoV-2, it was found that S2' cleavage and N protein were
347 strongly reduced in IL-1 β -treated mice-derived lung and intestine tissue cells compared to control
348 (**Figure 6G and Figure 6—figure supplement 2E**), suggesting that IL-1 β may have protective
349 effects on various tissue cells against SARS-CoV-2 infection *in vivo*.

350 To further verify the function and mechanism of IL-1 β in controlling SARS-CoV-2 transmission *in*
351 *vivo*, BALB/c mice were infected with authentic SARS-CoV-2 B.1.351 after IL-1 β or ROCK
352 inhibitor Y-27632+IL-1 β pre-treatment (**Figure 7—figure supplement 1A**). Similar to IL-1RA, Y-
353 27632 compromised the effect of IL-1 β in preventing weight loss (**Figure 7—figure supplement**
354 **1B**). In addition, H&E staining showed that Y-27632 treatment aggravated lung injury in IL-1 β -
355 treated mice upon SARS-CoV-2 infection (**Figure 7 A and B**), although Y-27632+IL-1 β did not
356 cause weight loss or lung injury in uninfected mice (**Figure 7—figure supplement 1C and D**).
357 Moreover, Y-27632 treatment increased the expression level of SARS-CoV-2 N gene (**Figure 7C**)
358 and infected area (**Figure 7D and E**) in the lungs of IL-1 β -treated mice. Importantly, Y-27632
359 treatment prevented the formation of IL-1 β -induced actin bundles at cell-cell junctions, thus
360 promoted syncytia formation and further viral transmission (**Figure 7F and Figure 7—figure**
361 **supplement 2A and B**). Furthermore, we treated BALB/c mice with PBS, IL-1 β or Y-27632 + IL-
362 1 β (**Figure 7—figure supplement 2C**), then isolated the lung tissue cells for authentic SARS-
363 CoV-2 infection. Here it was found that S2' cleavage and N protein were clearly reduced in IL-1 β
364 treated mice compared to control at day 2, while Y-27632 treatment abolished the inhibitory effect
365 of IL-1 β (**Figure 7—figure supplement 2D**). Of note, the lung tissue cells in IL-1 β -treated mice
366 remained resistant to SARS-CoV-2 infection at day 7, while the protective effect of IL-1 β was
367 abolished by Y-27632 treatment (**Figure 7G**). Taken together, IL-1 β prevents the transmission of
368 SARS-CoV-2 through inducing the formation of actin bundles via the RhoA/ROCK pathway *in*
369 *vivo*.

370 Discussion

371

372 In the present study, we explored the function of innate immune factors against SARS-CoV-2
373 infection. Notably, IL-1 β inhibited various SARS-CoV-2 variants and other beta-coronaviruses
374 spike-induced cell-cell fusion. Mechanistically, IL-1 β activates and enriches RhoA to the cell-cell
375 junction between SARS-CoV-2-infected cells and neighboring cells via the IL-1R-mediated signal
376 to initiate actin bundle formation, preventing cell-cell fusion and viral spreading (**Figure 7—figure**
377 **supplement 3**). These findings revealed a critical function for pro-inflammatory cytokines to
378 control viral infection.

379 Elevated IL-1 β levels in severe COVID-19 patients is central to innate immune response as it
380 induces the expression of other pro-inflammatory cytokines (Tahtinen et al., 2022). In addition, IL-
381 1 α is also secreted during SARS-CoV-2 infection (Xiao et al., 2021). Of note, several therapeutic
382 strategies have employed the inhibition of IL-1 signal in an attempt to treat SARS-CoV-2 infection
383 (Huet et al., 2020; Ucciferri et al., 2020). Intriguingly, although anakinra, a recombinant human IL-
384 1 receptor antagonist, improved clinical outcomes and reduced mortality in severe COVID-19
385 patients (Cavalli et al., 2020), it did not reduce mortality in mild-to-moderate COVID-19 patients,
386 and even increased the probability of serious adverse events (Tharoux et al., 2021). With another
387 note, IL-1 blockade significantly decreased the neutralizing activity of serous anti-SARS-CoV-2
388 antibodies in severe COVID-19 patients (Della-Torre et al., 2021). According to our finding that
389 both IL-1 β and IL-1 α are able to inhibit SARS-CoV-2-induced cell-cell fusion, inhibition of IL-1
390 signaling may have abolished the antiviral function of IL-1, thus failing to restrict virus-induced
391 syncytia formation and transmission.

392 Notably, IL-1 β plays a key role in triggering vaccine-induced innate immunity, suggesting that
393 innate immune responses play important roles in the antiviral defense by enhancing the
394 protective efficacy of vaccines (Eisenbarth, Colegio, O'Connor, Sutterwala, & Flavell, 2008;
395 Tahtinen et al., 2022). In addition, vaccination with *Bacillus Calmette-Guérin* (BCG) has been
396 reported to confer nonspecific protection against heterologous pathogens, including protection
397 against SARS-CoV-2 infection in humans and mice (Hilligan et al., 2022; A. Lee et al., 2023;
398 Rivas et al., 2021). Moreover, Lipid nanoparticle (LNP) in mRNA vaccine (Han et al., 2023) and
399 penton base in adenovirus vaccine (Di Paolo et al., 2009) can both activate innate immune cells
400 to amplify the protective effect of vaccines, which may also be attributed to IL-1 β -mediated
401 inhibition of SARS-CoV-2-induced cell-cell fusion on top of adaptive immune responses induced
402 by the vaccines.

403 With another note, patients with inherited MyD88 or IRAK4 deficiency have been reported to be
404 selectively vulnerable to COVID-19 pneumonia. It was found that these patients' susceptibility to
405 SARS-CoV-2 can be attributed to impaired type I IFN production, which do not sense the virus
406 correctly in the absence of MyD88 or IRAK4 (García-García et al., 2023). In our study, MyD88 or
407 IRAK4 deficiency abolished the inhibitory effect of IL-1 β on SARS-CoV-2 induced cell-cell fusion,
408 suggesting that these innate immune molecules are critical to contain SARS-CoV-2 infection, and
409 this may be another mechanism accounting for the disease of those patients. Moreover, MyD88
410 signaling was essential for BCG-induced innate and type 1 helper T cell (TH1 cell) responses and
411 protection against SARS-CoV-2, which is consistent with our findings.

412 Of note, cell-cell fusion is not limited to the process of viral infection, both normal and cancerous
413 cells can utilize this physiological process in tissue regeneration or tumor evolution (Delespaul et
414 al., 2020; Powell et al., 2011). For example, myoblast fusion is the key process of skeletal muscle
415 terminal differentiation, inactivation of RhoA/ROCK signaling is crucial for myoblast fusion
416 (Nishiyama, Kii, & Kudo, 2004). Our current work revealed that inhibition of RhoA/ROCK signaling
417 promoted virus-induced cell-cell fusion, possibly due to the virus hijacking of such biological
418 process. In turn, activated RhoA/ROCK signaling inhibits virus-induced cell-cell fusion, so it can
419 be targeted for future therapeutic development to control viral transmission. Cell-cell fusion is
420 mediated by actin cytoskeletal rearrangements, the dissolution of F-actin focus is essential for

421 cell-cell fusion; in contrast, syncytia formation cannot proceed if disassembly of actin filaments or
422 bundles is prevented (Doherty et al., 2011; Rodríguez-Pérez et al., 2021). We uncovered that
423 preventing actin bundles dissolution inhibited virus-induced cell-cell fusion, and IL-1 β induced
424 RhoA/ROCK signal promotes actin bundle formation at cell-cell junctions. As RhoA is ubiquitously
425 expressed by all cell types, it is currently unclear whether IL-1-mediated RhoA activation is
426 specific towards viral infection-associated cytoskeleton modification, or may regulate other RhoA-
427 related processes, which is a limitation of the current work and remains to be investigated in
428 future.

429 In summary, this study demonstrated the function and mechanism of IL-1 β in inhibiting SARS-
430 CoV-2 induced syncytia formation, and highlighted the function of innate immune factors including
431 cytokines against coronaviruses transmission, thus provide potential therapeutic targets for viral
432 control.

433 **Materials and Methods**

434 **Reagents and plasmids**

435 The antibodies used for immunoblotting include: rabbit anti-SARS-CoV-2 S2 (Sino Biological,
436 40590-T62, 1:2000), mouse anti-SARS-CoV-2 N (Sino Biological, 40143-MM05, 1:1000), rabbit
437 anti-ACE2 (Proteintech, 21115-1-AP, 1:2000), rabbit anti-MERS-CoV S2 (Sino Biological, 40070-
438 T62, 1:1000), rabbit anti-MyD88 (Cell Signaling Technology, 4283, 1:1000), rabbit anti-TRAF6
439 (Abcam, ab33915, 1:5000), rabbit anti-TAK1 (Cell Signaling Technology, 4505, 1:1000), mouse
440 anti-Myc-Tag (Abclonal, AE010,1:2000), HRP-conjugated β -tubulin (Abclonal, AC030, 1:5000),
441 mouse anti- β -actin (Proteintech, 66009-1-Ig, 1:5000), anti-rabbit/anti-mouse (Jackson Immuno
442 Research, 111-035-003, 1:5000). The antibodies and reagents used for immunofluorescence
443 include: rabbit anti-SARS-CoV-2 S2 (Sino Biological, 40590-T62, 1:200), mouse anti-SARS-CoV-
444 2 N (Sino Biological, 40143-MM05, 1:200), rabbit anti-ACE2 (Proteintech, 21115-1-AP, 1:200),
445 mouse anti-HA-Tag (Abclonal, AE008, 1:200). Actin-Tracker Green-488 (Beyotime,
446 C2201S,1:100), goat anti-mouse IgG-555 (Invitrogen, A-21424, 1: 400) and goat anti-rabbit IgG-
447 647 (Invitrogen, A-21236, 1: 400), DAPI (Abcam, ab228549, 1:2000) and antifade mounting
448 medium (vectorlabs, H-1400-10). Purified LTA from *S. aureus* (Invitrogen, tlr1-pslta), Pam3CSK4
449 (Invitrogen, tlr1-pms), Peptidoglycan from *S. aureus* (Sigma-Aldrich, 77140), LPS (Invitrogen, tlr1-
450 eklps), TPCA1 (Selleck, S2824), 5Z-7-Oxozeaenol (Sigma-Aldrich, O9890), IRAK1/4 inhibitor
451 (Selleck, S6598), Y-27632 (Selleck, S6390). Inhibitors were dissolved in dimethyl sulfoxide
452 (DMSO, Sigma-Aldrich, D2650), and DMSO was added as solvent control. Recombinant human
453 IL-1 α (200-01A), human IL-1 β (200-01B), mouse IL-1 β (211-11B), human IL-1RA (200-01RA),
454 human IL-6 (200-06) and human IL-8 (200-08M) were purchased from Peprotech. Mouse IL-1RA
455 (769706) was purchased from BioLegend. IL-1 β concentrations in supernatants from THP-1 and
456 PBMCs were determined using ELISA kit, according to the manufacturer's instructions (R&D
457 Systems, DY201). RhoA pull-down activation assay Biochem kit (BK036-S) was purchased from
458 Cytoskeleton, Inc. Collagenase, type I (17100017) was purchased from Gibco and B-ALI Growth
459 Media (00193516) was purchased from Lonza Bioscience.

460 SARS-CoV-2 spike (Wild type, GenBank: QHD43419.1) was homo sapiens codon-optimized and
461 generated *de novo* into pVAX1 vector by recursive polymerase chain reaction (PCR). WT, Alpha,
462 Beta and Delta variants containing point and deletion mutations were generated via stepwise
463 mutagenesis using spike construct containing the truncated 19 amino acids at the C-terminal
464 (CT Δ 19). The latest human codon optimized Omicron was purchased from Genescripts, and
465 subcloned into the pVAX1 backbone with CT Δ 19 for comparison. Human ACE2 assembled in a
466 pcDNA4.0 vector was used for transient expression of ACE2. GFP-AHPH (Addgene plasmid #
467 71368; <http://n2t.net/addgene:71368>; RRID: Addgene_71368) and pRK5myc RhoA L63
468 (Addgene plasmid # 15900; <http://n2t.net/addgene:15900>; RRID: Addgene_15900) were from
469 Addgene.

470 **Cell culture and stimulation**

471 HEK293T cells were purchased from the National Science & Technology Infrastructure (NSTI)
472 cell bank (www.cellbank.org.cn). Human colon epithelial carcinoma cell line Caco-2 (catalog no.
473 SCSP-5027) cells were obtained from Cell Bank/Stem Cell Bank, Chinese Academy of Sciences.
474 Human lung cancer cell line Calu-3 and Vero E6-ACE2 cells were gifted from Prof. Dimitri
475 Lavillette (Applied Molecular Virology Laboratory, Discovery Biology Department, Institut Pasteur
476 Korea). Human monocytic cell line THP-1 (TIB-202; ATCC) was authenticated at Genetic Testing
477 Biotechnology Corporation (Suzhou, China) using Short Tandem Repeat (STR) analysis as
478 described in 2012 in ANSI Standard (ASN-0002) by the ATCC Standards Development
479 Organization. HEK293T and Vero E6-ACE2 cells were cultured in Gibco Dulbecco's Modified
480 Eagle Medium (DMEM) (GE Healthcare) supplemented with 10% fetal bovine serum (FBS)
481 (Sigma) and 1% Penicillin/streptomycin (P/S) (Life Technologies) at 37°C with 5% CO₂ in a
482 humidified incubator. Caco-2 and Calu-3 cells were cultured in Minimum Essential Medium (MEM)

483 supplemented with 10% FBS, 1% non-essential amino acids and 1% P/S at 37°C with 5% CO₂ in
484 a humidified incubator. THP-1 cells were cultured in Roswell Park Memorial Institute (RPMI) 1640
485 supplemented with 10% FBS, 1% P/S and 50 µM 2-ME at 37°C with 5% CO₂ in a humidified
486 incubator. All cells were routinely tested for mycoplasma contamination; passages between 4th to
487 25th were used. Human PBMCs were isolated from the peripheral blood of healthy donors
488 (Shanghai Blood Center). This study was performed in accordance with the International Ethical
489 Guidelines for Biomedical Research Involving Human Subjects and the principles expressed in
490 the Declaration of Helsinki. Briefly, fresh human PBMCs were separated using Ficoll-Paque
491 PLUS reagent (cytiva, 17144003) at 1200 g for 10 min at room temperature with SepMate™-50
492 (SepMate, 86450). PBMCs were washed three times with filtered PBS containing 0.5% BSA and
493 2 mM EDTA. PBMCs were counted and resuspended in RPMI 1640 medium supplemented with
494 1% FBS and 1% P/S.

495 For stimulation, THP-1 cells were seeded at 2×10^6 cells per ml in FBS free RPMI 1640 and
496 PBMCs were seeded at 1×10^7 cells per ml in 1% FBS RPMI 1640, then stimulated with LTA (10
497 µg/ml), Pam3CSK4 (1 µg/ml), PGN (2 µg/ml), LPS (1 µg/ml) for 24 hours, cell culture
498 supernatants were collected after centrifugation at 2000 g for 5 min for subsequent experiments.

499 **Transient transfection and cell-cell fusion assays**

500 For transient transfections, HEK293T cells were seeded in 24-well plates at 0.5×10^6 cells /mL
501 overnight. 250 ng plasmids encoding SARS-CoV-2 spike mutants or ACE2 variants were
502 packaged in Lipofectamine 2000 (Life technologies) and transfected for 24 hours. For luciferase
503 assays, Spike-mediated membrane fusion, a *Cre-loxp* Firefly luciferase (*Stop-Luc*) co-expression
504 system was introduced to enable the detection of DNA recombination events during cell-cell
505 fusion. 200 ng Cre plasmids were co-transfected into HEK293T-S cells and 200 ng *Stop-Luc*
506 plasmid were co-transfected into HEK293T ± ACE2 cells, respectively. For visualization of
507 syncytia formation, 100 ng ZsGreen plasmid was co-transfected with spike variants. HEK293T
508 cells in the 24-well plates were then detached using ice-cold calcium-free PBS in the absence of
509 trypsin and centrifuged at 600 g for 4 min.

510 For cell-cell fusion assays, cell pellets were resuspended into complete DMEM and mixed with
511 control HEK293T cells, or HEK293T-ACE2, Vero E6-ACE2 or Calu-3 cells at 1:1 ratio before
512 adhesion to the 48-well or 96-well plates, cell mixes were incubated for 16 hours at 37°C.
513 Quantification of cell-cell fusion was performed by measuring luciferase expression as relative
514 luminescence units (RLU) 1 min by mixing cell lysates with the Bright-Glo luciferase substrate
515 (E2610, Promega) on a Synergy H1 plate reader (Biotek). Fluorescent images showing syncytia
516 formation were captured at endpoint using a 10x objective and 12-bit monochrome CMOS
517 camera installed on the IX73 inverted microscope (Olympus). Attached cells and syncytia were
518 lysed in a NP40 lysis buffer containing 0.5% (v/v) NP40, 25 mM Tris pH 7.3, 150 mM NaCl, 5%
519 glycerol and 1x EDTA-free protease inhibitor cocktail (PIC) (Roche).

520 **Immunoblotting**

521 Tissue culture plates containing adherent syncytia and cell mixes were directly lysed on ice in 2x
522 reducing Laemmli loading buffer before boiled at 95°C for 5 min. Protein samples were separated
523 by standard Tris-glycine SDS-PAGE on 7.5% or 9.5% Tris-glycine polyacrylamide gels. Proteins
524 were then transferred onto 0.45 µm PVDF membranes (Millipore) for wet transfer using Towbin
525 transfer buffer. All membranes were blocked in PBS supplemented with 0.1% Tween20 (PBST)
526 and 2.5% bovine serum albumin (BSA) or 5% non-fat dry milk, before overnight incubation in
527 primary antibodies at 4°C. Blots were labelled with HRP-tagged secondary antibodies (Jackson
528 ImmnuoResearch) and visualized with PicoLight substrate enhanced chemiluminescence (ECL)
529 solution (Epizyme Scientific). Immunoblot images were captured digitally using a 5200
530 chemiluminescent imaging system (Tanon) with molecular weight markers indicated.

531 **Real time PCR**

532 0.5 x 10⁶ cells/mL HEK293T cells were seeded in 24 well plates overnight. After the cells were
533 about 80% covered, specified stimulant was added. Upon harvesting, cells were washed with
534 PBS for three times, and 1 mL TRIzol Reagent (15596018; Thermo Fisher Scientific) was added
535 for full lysis at room temperature for 5 min. 250 µL chloroform was added, fully mixed at room
536 temperature for 5 min, centrifuged at 10000 r/min, 4°C for 10 min. After carefully removing the
537 aqueous phase using a pipette into another 1.5 mL Eppendorf tube, some of the aqueous phase
538 (about 1 mm above DNA layer to prevent DNA contamination) was remained. 550 µL isopropanol
539 was added in the aqueous phase and mixed gently, then placed at -20°C for 30 min. The tubes
540 were centrifuged at 14000 r/min, 4°C for 20 min, and washed with 75% ethanol twice before
541 dissolved in 30 µL DEPC water. RNA was reverse transcribed to cDNA using a GoSript Reverse
542 Transcription Kit (Promega). Real-time PCR was performed using SYBR Green Realtime PCR
543 Master Mix (TOYOBO) on ABI QuantStudio 6 flex Real-time PCR System (Thermo Fisher
544 Scientific). The RT-qPCR Primer sequences for targeting genes are displayed in Table S1. Target
545 genes' relative quantification was normalized to GAPDH as relative unit (RU).

546 **CRISPR/Cas9-Mediated Gene Targeting**

547 Gene-deficient THP-1 or HEK293T cells were generated using CRISPR/Cas9-mediated gene
548 targeting technology. Briefly, LentiCRISPR v2 (52961; addgene) containing sgRNA specifically
549 targeting indicated genes were constructed. The sgRNA sequences for targeting respective
550 genes are displayed in Table S2. The Lentiviral particles were produced in HEK293T cells by
551 transfection with LentiCRISPR v2-sg gene, psPAX2, VSV-G at 2:1.5:1 ratio using Lipofectamine
552 2000. The lentiviral particles were employed to infect THP-1 or HEK293T cells. One day post
553 infection, the cells were subjected to puromycin selection at a concentration of 2 µg/ml for 72
554 hours. Survived cells were subjected to limiting dilution in 96-well plates to obtain single clones
555 stably knocking-out respective genes.

556 **RhoA pull-down assay**

557 RhoA pull-down activation assay Biochem kit was applied for this experiment. In brief, after 1
558 ng/mL IL-1β treatment for 30 min, HEK293T cells were placed on ice and the culture media was
559 aspirated off before washing cells with ice cold PBS, then washed cells were transferred into 1.5
560 mL Eppendorf tubes followed with a centrifugation 600 g, 4°C for 5 min. Then the cell lysis buffer
561 with protease inhibitor cocktail was added. The tubes were immediately centrifuged at 10000 g,
562 4°C for 1 min, then 20 µL of the lysate was saved for total RhoA, and the remaining lysate was
563 used for pull-down assay. For pull-down assay, 10 µL rhotekin-RBD beads were mixed with 600
564 µg total protein, then the tubes were incubated at 4°C on a rotator for 1 hour before centrifuged at
565 5000 g, 4°C for 1 min. Next, 90% of the supernatant were carefully removed before washing
566 beads with 500 µL wash buffer. Then the tubes were centrifuged at 5000 g, 4°C for 3 min, and
567 supernatant was carefully removed before adding 20 µL of 2 x Laemmli sample buffer, then the
568 beads were thoroughly resuspended and boiled for 2 min and analyzed through Immunoblotting.

569 **Immunostaining and confocal microscopy**

570 HEK293T-ACE2 cells were seeded onto sterilized poly-D-lysine (100 ug/mL) (Beyotime, ST508)
571 treated 12 mm coverslips (fisher scientific, 1254580) in 24-well plates. After co-culture with
572 HEK293T-S, cells were washed with PBS once before fixing with 4% (w/v) paraformaldehyde
573 (PFA) for 20 min. Then, cells were washed twice with PBS and permeabilized with 0.1% Triton at
574 room temperature for 10 min (For WGA staining, cells were not treated with Triton). Next, cells
575 were washed twice with PBS and blocked with Immunol Staining Blocking Buffer (Beyotime,
576 P0102) at room temperature for 1 hour. Primary antibodies were incubated at room temperature
577 for 1 hour. Coverslips were then washed twice with PBS before incubation with Actin-Tracker
578 Green-488 or secondary antibodies for 1 hour at room temperature. Coverslips were washed

579 twice with PBS before DAPI staining for 10 min or being mounted in antifade mounting medium.
580 Fluorescent images covering various areas on the coverslips were captured at 12-bit depth in
581 monochrome using a 100x oil immersion objective on the Olympus SpinSR10 confocal
582 microscope and subsequently processed using imageJ software (NIH) with scale bars labeled.

583 **Authentic SARS-CoV-2 Infection of cells**

584 All experiments involving authentic SARS-CoV-2 virus *in vitro* were conducted in the biosafety
585 level 3 (BSL3) laboratory of the Shanghai municipal center for disease control and prevention
586 (CDC). The experiments and protocols in this study were approved by the Ethical Review
587 Committee of the Shanghai CDC. Briefly, HEK293T-ACE2 or Caco-2 cells were seeded into 24-
588 well or 96-well plates at a density of 4×10^5 cells per mL overnight, then pre-treated with different
589 reagents for 1 hour before infection with 0.5 multiplicity of infection (MOI) Delta or WT authentic
590 SARS-CoV-2 (B.1.617.2 and WT) for 24 hours. Calu-3 cells were seeded into 24-well or 96-well
591 plates at a density of 4×10^5 cells per mL overnight, infected with 0.5 MOI WT authentic SARS-
592 CoV-2 for 1 hour, then washed with PBS before treating with different reagents for 24 hours.
593 Brightfield images were captured to indicate the syncytia formation, cell lysates were collected for
594 spike S2' cleavage and N protein immunoblots.

595 For primary mouse tissue cells, specific pathogen-free 6-week-old female BALB/c mice were
596 lightly anesthetized with isoflurane and intranasal treated with PBS, mL-1 β (1 μ g/kg) or Y-27632
597 (1 mg/kg) + mL-1 β (1 μ g/kg) at day 0, then mice were Intraperitoneal injected with PBS, mL-1 β
598 (1 μ g/kg) or Y-27632 (1 mg/kg) + mL-1 β (1 μ g/kg) at day 1 and 2. At day 7, mice were
599 anesthetized by intraperitoneal injection of Avertin (2,2,2-tribromoethanol, Sigma-Aldrich), the
600 thoracic cavity and abdominal cavity were opened, an outlet was cut in the left ventricle of the
601 mice, and then the right ventricle was perfused with phosphate buffer saline (PBS) through the
602 pulmonary artery to remove blood cells in the lung. Next, the lung digestive solution with HBSS
603 1ml, 1 mg/ml collagenase IA, DnaseI (200 mg/ml; Roche), Dispasell (4 U/ml; Gibco) and 5% FBS
604 was injected into the lung cavity, then the lungs were peeled off and digested for 30 min with
605 shaking at 37°C. For the intestinal cell isolation, the intestines are peeled off and put into the
606 intestine digestive solution containing DMEM 10mL, 1 μ M DTT, 0.25 μ M EDTA and 5% FBS, then
607 digested for 30 min with shaking at 37°C. After digestion, the lung and intestinal cells were
608 resuspended in DMEM supplemented with 10% FBS and 1% P/S, subsequently, the cells were
609 infected with 1 MOI authentic SARS-CoV-2 B.1.351 or BF.7 for 24 hours. All procedures were
610 conducted in compliance with a protocol approved by the Institutional Animal Care and Use
611 Committee (IACUC) at Shanghai Institute of Immunity and Infection, Chinese Academy of
612 Sciences.

613 For primary human lung cells, the human lung tissues were cut into small pieces of about 2 mm³
614 and washed three times with HBSS solution containing 1% PS, digested with collagenase type I
615 (100 mg+50 mL PBS) in an incubator at 37°C for 4 hours. Then filtered through a 70 μ m filter and
616 centrifuged at 500 g for 5 min at room temperature. Lysed with 3 mL Red Blood Cell Lysis Buffer
617 for 5min at room temperature, and then centrifuged at 500 g for 5 min at room temperature,
618 washed twice with HBSS solution containing 1% PS. Human lung cells were resuspended in B-
619 ALI Growth Media and seeded into 96-well plates at a density of 4×10^5 cells per mL overnight,
620 infected with 0.5 MOI WT authentic SARS-CoV-2 for 1 hour, then washed with PBS before
621 treating cells with different reagents for 24 hours. The experiments and protocols were approved
622 by the Ethical Review Committee of the Shanghai CDC.

623 **Authentic SARS-CoV-2 infection of BALB/c mice**

624 Specific pathogen-free 6-week-old female BALB/c mice were lightly anesthetized with isoflurane
625 and intranasal treated with PBS, mL-1 β (1 μ g/kg), mL-1RA (150 μ g/kg) + mL-1 β (1 μ g/kg); or
626 PBS, mL-1 β (1 μ g/kg), Y-27632 (1 mg/kg) + mL-1 β (1 μ g/kg) for 1 hour, then intranasal
627 challenged with 5×10^4 FFU of SARS-CoV-2 B.1.351. For booster injection, mice were

628 Intraperitoneal injected with PBS, mL-1 β (1 μ g/kg), mL-1RA (150 μ g/kg) + mL-1 β (1 μ g/kg); or
629 PBS, mL-1 β (1 μ g/kg), Y-27632 (1 mg/kg) + mL-1 β (1 μ g/kg) at 1- and 2-days post infection
630 (dpi). Mice were monitored daily for weight loss. Lungs were removed into Trizol or 4% PFA at 4
631 dpi. All protocols were approved by the Institutional Animal Care and Use Committee of the
632 Guangzhou Medical University.

633 **Pulmonary histopathology**

634 Lungs were collected from mice infected with SARS-CoV-2 at 4 dpi and fixed in 4% PFA (Bioss)
635 for 12 hours followed by dehydrating, embedded in paraffin for sectioning, then stained with
636 hematoxylin and eosin (H&E), immunohistochemistry (IHC) or immunofluorescence (IF). H&E and
637 IHC data were analyzed by PerkinElmer Vectra 3, IF results were analyzed by Olympus
638 SpinSR10 confocal microscope. The pathological scores were judged according to previous work
639 (Curtis, Warnock, Arraj, & Kaltreider, 1990).

640 **Statistics analysis**

641 Bar graphs were presented as mean values \pm standard error of mean (SEM) with individual data
642 points. All statistical analyses were carried out with the Prism software v8.0.2 (GraphPad). Data
643 with multiple groups were analyzed using matched one-way ANOVA followed by Sidak's post hoc
644 comparisons. Statistical significance P values were indicated between compared groups and
645 shown on Figures.

646

647 **Acknowledgments**

648

649 We thank Qihong Guo, Prof. Dimitri Lavillette and Prof. Gary Wong for their experimental
650 supports and reagents used in this work. This study is supported by grants from Natural Science
651 Foundation of China (92269202, 82825001, 92054104, 82402593), National Key R&D Program
652 of China (2022YFC2304700, 2022YFC2303200, 2022YFC2303502), Strategic Priority Research
653 Program of the Chinese Academy of Sciences (XDB0940102), Three-Year Initiative Plan for
654 Strengthening Public Health System Construction in Shanghai (2023-2025) Key Discipline Project
655 (GWVI-11.1-09), Shanghai Municipal Science and Technology Major Project (2019SHZDZX02),
656 Shanghai Natural Science Foundation Projects (24ZR1476700, 24ZR1476600), State Key
657 Laboratory of Respiratory Disease Project (J24411029), Guangdong Basic and Applied Basic
658 Research Foundation (2023A1515010152) and Young Scientists Fund of the Guangzhou
659 National Laboratory (QNPG23-03).

660

661 **References**

- 662 Arabi, Y. M., Mandourah, Y., Al-Hameed, F., Sindi, A. A., Almekhlafi, G. A., Hussein, M. A., . . .
663 Fowler, R. A. (2018). Corticosteroid Therapy for Critically Ill Patients with Middle East
664 Respiratory Syndrome. *Am J Respir Crit Care Med*, 197(6), 757-767. doi:10.1164/rccm.201706-
665 1172OC
- 666 Barnett, K. C., Xie, Y., Asakura, T., Song, D., Liang, K., Taft-Benz, S. A., . . . Ting, J. P. (2023). An
667 epithelial-immune circuit amplifies inflammasome and IL-6 responses to SARS-CoV-2. *Cell Host*
668 *Microbe*, 31(2), 243-259.e246. doi:10.1016/j.chom.2022.12.005
- 669 Belouzard, S., Chu, V. C., & Whittaker, G. R. (2009). Activation of the SARS coronavirus spike
670 protein via sequential proteolytic cleavage at two distinct sites. *Proc Natl Acad Sci U S A*,
671 106(14), 5871-5876. doi:10.1073/pnas.0809524106
- 672 Blanco-Melo, D., Nilsson-Payant, B. E., Liu, W. C., Uhl, S., Hoagland, D., Møller, R., . . . tenOever,
673 B. R. (2020). Imbalanced Host Response to SARS-CoV-2 Drives Development of COVID-19. *Cell*,
674 181(5), 1036-1045.e1039. doi:10.1016/j.cell.2020.04.026

675 Bussani, R., Schneider, E., Zentilin, L., Collesi, C., Ali, H., Braga, L., . . . Giacca, M. (2020).
676 Persistence of viral RNA, pneumocyte syncytia and thrombosis are hallmarks of advanced
677 COVID-19 pathology. *EBioMedicine*, *61*, 103104. doi:10.1016/j.ebiom.2020.103104
678 Cavalli, G., De Luca, G., Campochiaro, C., Della-Torre, E., Ripa, M., Canetti, D., . . . Dagna, L.
679 (2020). Interleukin-1 blockade with high-dose anakinra in patients with COVID-19, acute
680 respiratory distress syndrome, and hyperinflammation: a retrospective cohort study. *Lancet*
681 *Rheumatol*, *2*(6), e325-e331. doi:10.1016/s2665-9913(20)30127-2
682 Chen, L. Y., Zuraw, B. L., Liu, F. T., Huang, S., & Pan, Z. K. (2002). IL-1 receptor-associated kinase
683 and low molecular weight GTPase RhoA signal molecules are required for bacterial
684 lipopolysaccharide-induced cytokine gene transcription. *J Immunol*, *169*(7), 3934-3939.
685 doi:10.4049/jimmunol.169.7.3934
686 Curtis, J. L., Warnock, M. L., Arraj, S. M., & Kaltreider, H. B. (1990). Histologic analysis of an
687 immune response in the lung parenchyma of mice. Angiopathy accompanies inflammatory cell
688 influx. *Am J Pathol*, *137*(3), 689-699.
689 Delespaul, L., Gélabert, C., Lesluyes, T., Le Guellec, S., Pérot, G., Leroy, L., . . . Chibon, F. (2020).
690 Cell-cell fusion of mesenchymal cells with distinct differentiations triggers genomic and
691 transcriptomic remodelling toward tumour aggressiveness. *Sci Rep*, *10*(1), 21634.
692 doi:10.1038/s41598-020-78502-z
693 Della-Torre, E., Criscuolo, E., Lanzillotta, M., Locatelli, M., Clementi, N., Mancini, N., & Dagna, L.
694 (2021). IL-1 and IL-6 inhibition affects the neutralising activity of anti-SARS-CoV-2 antibodies in
695 patients with COVID-19. *Lancet Rheumatol*, *3*(12), e829-e831. doi:10.1016/s2665-
696 9913(21)00321-0
697 Di Paolo, N. C., Miao, E. A., Iwakura, Y., Murali-Krishna, K., Aderem, A., Flavell, R. A., . . .
698 Shayakhmetov, D. M. (2009). Virus binding to a plasma membrane receptor triggers interleukin-
699 1 alpha-mediated proinflammatory macrophage response in vivo. *Immunity*, *31*(1), 110-121.
700 doi:10.1016/j.immuni.2009.04.015
701 Doherty, J. T., Lenhart, K. C., Cameron, M. V., Mack, C. P., Conlon, F. L., & Taylor, J. M. (2011).
702 Skeletal muscle differentiation and fusion are regulated by the BAR-containing Rho-GTPase-
703 activating protein (Rho-GAP), GRAF1. *J Biol Chem*, *286*(29), 25903-25921.
704 doi:10.1074/jbc.M111.243030
705 Dupraz, S., Hilton, B. J., Husch, A., Santos, T. E., Coles, C. H., Stern, S., . . . Bradke, F. (2019). RhoA
706 Controls Axon Extension Independent of Specification in the Developing Brain. *Curr Biol*, *29*(22),
707 3874-3886 e3879. doi:10.1016/j.cub.2019.09.040
708 Eisenbarth, S. C., Colegio, O. R., O'Connor, W., Sutterwala, F. S., & Flavell, R. A. (2008). Crucial
709 role for the Nalp3 inflammasome in the immunostimulatory properties of aluminium adjuvants.
710 *Nature*, *453*(7198), 1122-1126. doi:10.1038/nature06939
711 García-García, A., Pérez de Diego, R., Flores, C., Rinchai, D., Solé-Violán, J., Deyà-Martínez, À., . . .
712 Rodríguez-Gallego, C. (2023). Humans with inherited MyD88 and IRAK-4 deficiencies are
713 predisposed to hypoxemic COVID-19 pneumonia. *J Exp Med*, *220*(5). doi:10.1084/jem.20220170
714 Hadjadj, J., Yatim, N., Barnabei, L., Corneau, A., Boussier, J., Smith, N., . . . Terrier, B. (2020).
715 Impaired type I interferon activity and inflammatory responses in severe COVID-19 patients.
716 *Science*, *369*(6504), 718-724. doi:10.1126/science.abc6027
717 Han, X., Alameh, M. G., Butowska, K., Knox, J. J., Lundgreen, K., Ghattas, M., . . . Mitchell, M. J.
718 (2023). Adjuvant lipidoid-substituted lipid nanoparticles augment the immunogenicity of SARS-
719 CoV-2 mRNA vaccines. *Nat Nanotechnol*. doi:10.1038/s41565-023-01404-4

720 Hilligan, K. L., Namasivayam, S., Clancy, C. S., O'Mard, D., Oland, S. D., Robertson, S. J., . . . Sher,
721 A. (2022). Intravenous administration of BCG protects mice against lethal SARS-CoV-2 challenge.
722 *J Exp Med*, 219(2). doi:10.1084/jem.20211862
723 Huet, T., Beaussier, H., Voisin, O., Jouveshomme, S., Dauriat, G., Lazareth, I., . . . Hayem, G.
724 (2020). Anakinra for severe forms of COVID-19: a cohort study. *Lancet Rheumatol*, 2(7), e393-
725 e400. doi:10.1016/s2665-9913(20)30164-8
726 Karki, R., Sharma, B. R., Tuladhar, S., Williams, E. P., Zalduondo, L., Samir, P., . . . Kanneganti, T.
727 D. (2021). Synergism of TNF- α and IFN- γ Triggers Inflammatory Cell Death, Tissue Damage, and
728 Mortality in SARS-CoV-2 Infection and Cytokine Shock Syndromes. *Cell*, 184(1), 149-168.e117.
729 doi:10.1016/j.cell.2020.11.025
730 Lee, A., Floyd, K., Wu, S., Fang, Z., Tan, T. K., Froggatt, H. M., . . . Pulendran, B. (2023). BCG
731 vaccination stimulates integrated organ immunity by feedback of the adaptive immune
732 response to imprint prolonged innate antiviral resistance. *Nat Immunol*. doi:10.1038/s41590-
733 023-01700-0
734 Lee, N., Allen Chan, K. C., Hui, D. S., Ng, E. K., Wu, A., Chiu, R. W., . . . Lo, Y. M. (2004). Effects of
735 early corticosteroid treatment on plasma SARS-associated Coronavirus RNA concentrations in
736 adult patients. *J Clin Virol*, 31(4), 304-309. doi:10.1016/j.jcv.2004.07.006
737 Li, Z., Li, S., Zhang, G., Peng, W., Chang, Z., Zhang, X., . . . Wu, Y. (2022). An engineered bispecific
738 human monoclonal antibody against SARS-CoV-2. *Nat Immunol*, 23(3), 423-430.
739 doi:10.1038/s41590-022-01138-w
740 Martínez-Mármol, R., Giordano-Santini, R., Kaulich, E., Cho, A. N., Przybyla, M., Riyadh, M. A., . . .
741 Hilliard, M. A. (2023). SARS-CoV-2 infection and viral fusogens cause neuronal and glial fusion
742 that compromises neuronal activity. *Sci Adv*, 9(23), eadg2248. doi:10.1126/sciadv.adg2248
743 Medzhitov, R. (2001). Toll-like receptors and innate immunity. *Nat Rev Immunol*, 1(2), 135-145.
744 doi:10.1038/35100529
745 Nishiyama, T., Kii, I., & Kudo, A. (2004). Inactivation of Rho/ROCK signaling is crucial for the
746 nuclear accumulation of FKHR and myoblast fusion. *J Biol Chem*, 279(45), 47311-47319.
747 doi:10.1074/jbc.M403546200
748 Nobes, C. D., & Hall, A. (1999). Rho GTPases control polarity, protrusion, and adhesion during
749 cell movement. *J Cell Biol*, 144(6), 1235-1244. doi:10.1083/jcb.144.6.1235
750 Pfaender, S., Mar, K. B., Michailidis, E., Kratzel, A., Boys, I. N., V'Kovski, P., . . . Thiel, V. (2020).
751 LY6E impairs coronavirus fusion and confers immune control of viral disease. *Nat Microbiol*,
752 5(11), 1330-1339. doi:10.1038/s41564-020-0769-y
753 Powell, A. E., Anderson, E. C., Davies, P. S., Silk, A. D., Pelz, C., Impey, S., & Wong, M. H. (2011).
754 Fusion between Intestinal epithelial cells and macrophages in a cancer context results in nuclear
755 reprogramming. *Cancer Res*, 71(4), 1497-1505. doi:10.1158/0008-5472.Can-10-3223
756 Priya, R., Gomez, G. A., Budnar, S., Verma, S., Cox, H. L., Hamilton, N. A., & Yap, A. S. (2015).
757 Feedback regulation through myosin II confers robustness on RhoA signalling at E-cadherin
758 junctions. *Nat Cell Biol*, 17(10), 1282-1293. doi:10.1038/ncb3239
759 Rajah, M. M., Bernier, A., Buchrieser, J., & Schwartz, O. (2022). The Mechanism and
760 Consequences of SARS-CoV-2 Spike-Mediated Fusion and Syncytia Formation. *J Mol Biol*, 434(6),
761 167280. doi:10.1016/j.jmb.2021.167280
762 Ren, X., Wen, W., Fan, X., Hou, W., Su, B., Cai, P., . . . Zhang, Z. (2021). COVID-19 immune
763 features revealed by a large-scale single-cell transcriptome atlas. *Cell*, 184(7), 1895-1913 e1819.
764 doi:10.1016/j.cell.2021.01.053
765 Riento, K., & Ridley, A. J. (2003). Rocks: multifunctional kinases in cell behaviour. *Nat Rev Mol*
766 *Cell Biol*, 4(6), 446-456. doi:10.1038/nrm1128

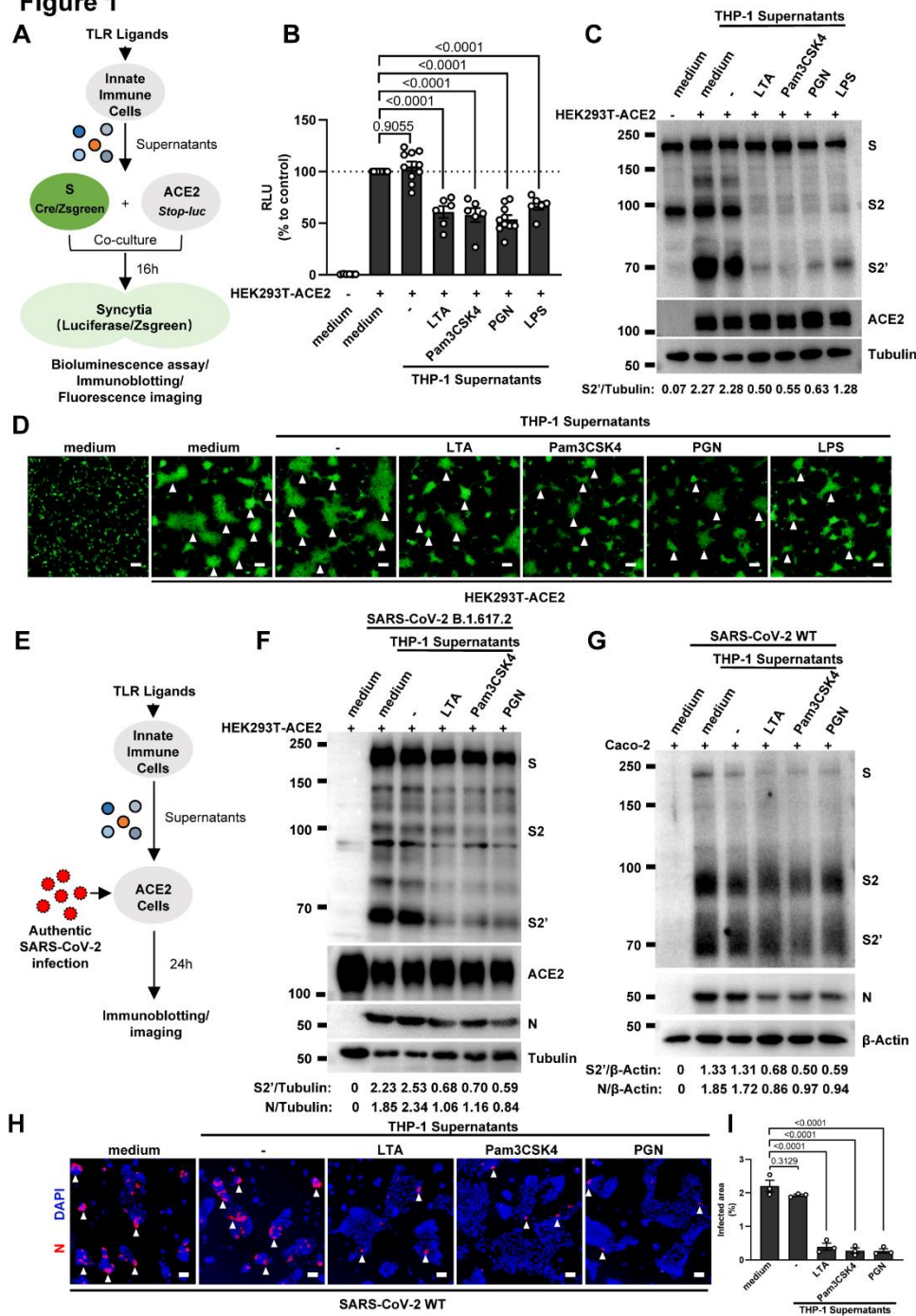
767 Rivas, M. N., Ebinger, J. E., Wu, M., Sun, N., Braun, J., Sobhani, K., . . . Arditi, M. (2021). BCG
768 vaccination history associates with decreased SARS-CoV-2 seroprevalence across a diverse
769 cohort of health care workers. *J Clin Invest*, *131*(2). doi:10.1172/jci145157
770 Rodríguez-Pérez, F., Manford, A. G., Pogson, A., Ingersoll, A. J., Martínez-González, B., & Rape,
771 M. (2021). Ubiquitin-dependent remodeling of the actin cytoskeleton drives cell fusion. *Dev Cell*,
772 *56*(5), 588-601.e589. doi:10.1016/j.devcel.2021.01.016
773 Sefik, E., Qu, R., Junqueira, C., Kaffe, E., Mirza, H., Zhao, J., . . . Flavell, R. A. (2022).
774 Inflammasome activation in infected macrophages drives COVID-19 pathology. *Nature*,
775 *606*(7914), 585-593. doi:10.1038/s41586-022-04802-1
776 Stern, S., Hilton, B. J., Burnside, E. R., Dupraz, S., Handley, E. E., Gonyer, J. M., . . . Bradke, F.
777 (2021). RhoA drives actin compaction to restrict axon regeneration and astrocyte reactivity after
778 CNS injury. *Neuron*, *109*(21), 3436-3455 e3439. doi:10.1016/j.neuron.2021.08.014
779 Straus, M. R., Tang, T., Lai, A. L., Flegel, A., Bidon, M., Freed, J. H., . . . Whittaker, G. R. (2020).
780 Ca(2+) Ions Promote Fusion of Middle East Respiratory Syndrome Coronavirus with Host Cells
781 and Increase Infectivity. *J Virol*, *94*(13). doi:10.1128/jvi.00426-20
782 Sun, L., Guan, R., Lee, I. J., Liu, Y., Chen, M., Wang, J., . . . Chen, Z. (2015). Mechanistic insights
783 into the anchorage of the contractile ring by anillin and Mid1. *Dev Cell*, *33*(4), 413-426.
784 doi:10.1016/j.devcel.2015.03.003
785 Tahtinen, S., Tong, A. J., Himmels, P., Oh, J., Paler-Martinez, A., Kim, L., . . . Mellman, I. (2022). IL-
786 1 and IL-1ra are key regulators of the inflammatory response to RNA vaccines. *Nat Immunol*,
787 *23*(4), 532-542. doi:10.1038/s41590-022-01160-y
788 Tharaux, P.-L., Pialoux, G., Pavot, A., Mariette, X., Hermine, O., Resche-Rigon, M., . . . Renet, S.
789 (2021). Effect of anakinra versus usual care in adults in hospital with COVID-19 and mild-to-
790 moderate pneumonia (CORIMUNO-ANA-1): a randomised controlled trial. *The Lancet*
791 *Respiratory Medicine*, *9*(3), 295-304. doi:[https://doi.org/10.1016/S2213-2600\(20\)30556-7](https://doi.org/10.1016/S2213-2600(20)30556-7)
792 Ucciferri, C., Auricchio, A., Di Nicola, M., Potere, N., Abbate, A., Cipollone, F., . . . Falasca, K.
793 (2020). Canakinumab in a subgroup of patients with COVID-19. *Lancet Rheumatol*, *2*(8), e457-
794 ee458. doi:10.1016/s2665-9913(20)30167-3
795 van der Heijden, M., Versteilen, A. M., Sipkema, P., van Nieuw Amerongen, G. P., Musters, R. J.,
796 & Groeneveld, A. B. (2008). Rho-kinase-dependent F-actin rearrangement is involved in the
797 inhibition of PI3-kinase/Akt during ischemia-reperfusion-induced endothelial cell apoptosis.
798 *Apoptosis*, *13*(3), 404-412. doi:10.1007/s10495-007-0173-6
799 Wang, S., Li, W., Hui, H., Tiwari, S. K., Zhang, Q., Croker, B. A., . . . Rana, T. M. (2020). Cholesterol
800 25-Hydroxylase inhibits SARS-CoV-2 and other coronaviruses by depleting membrane
801 cholesterol. *EMBO J*, *39*(21), e106057. doi:10.15252/embj.2020106057
802 Watanabe, N., Kato, T., Fujita, A., Ishizaki, T., & Narumiya, S. (1999). Cooperation between
803 mDia1 and ROCK in Rho-induced actin reorganization. *Nat Cell Biol*, *1*(3), 136-143.
804 doi:10.1038/11056
805 Weber, A., Wasiliew, P., & Kracht, M. (2010). Interleukin-1beta (IL-1beta) processing pathway.
806 *Sci Signal*, *3*(105), cm2. doi:10.1126/scisignal.3105cm2
807 Xiao, N., Nie, M., Pang, H., Wang, B., Hu, J., Meng, X., . . . Hu, Z. (2021). Integrated cytokine and
808 metabolite analysis reveals immunometabolic reprogramming in COVID-19 patients with
809 therapeutic implications. *Nat Commun*, *12*(1), 1618. doi:10.1038/s41467-021-21907-9
810 Yu, S., Zheng, X., Zhou, B., Li, J., Chen, M., Deng, R., . . . Meng, G. (2022). SARS-CoV-2 spike
811 engagement of ACE2 primes S2' site cleavage and fusion initiation. *Proc Natl Acad Sci U S A*,
812 *119*(1). doi:10.1073/pnas.2111199119

813 Yu, S., Zheng, X., Zhou, Y., Gao, Y., Zhou, B., Zhao, Y., . . . Meng, G. (2023). Antibody-mediated
814 spike activation promotes cell-cell transmission of SARS-CoV-2. *PLoS Pathog*, *19*(11), e1011789.
815 doi:10.1371/journal.ppat.1011789
816 Zhou, P., Yang, X. L., Wang, X. G., Hu, B., Zhang, L., Zhang, W., . . . Shi, Z. L. (2020). A pneumonia
817 outbreak associated with a new coronavirus of probable bat origin. *Nature*, *579*(7798), 270-273.
818 doi:10.1038/s41586-020-2012-7

819

820 **Figures**

Figure 1



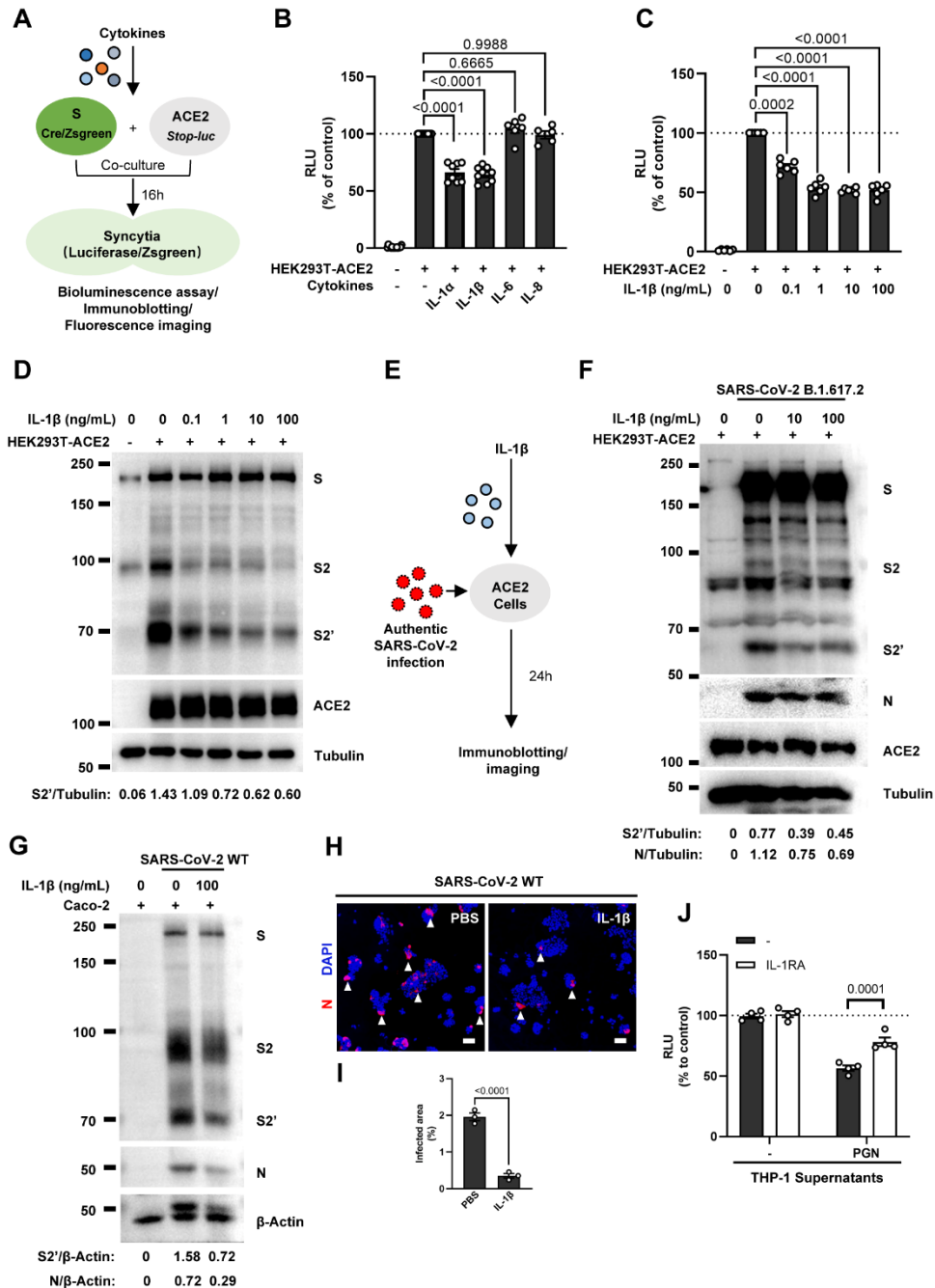
821
822
823

Figure 1. Host factors secreted by activated innate immune cells inhibit SARS-CoV-2-induced cell-cell fusion.

824 (A) Schematics of the cell-cell fusion model used to quantify spike-mediated syncytium formation
825 upon treatment with cell culture supernatants from TLR ligands-stimulated innate immune cells.
826 Cells co-expressing SARS-CoV-2 spike and Cre, were co-cultured with ACE2 and *Stop-luc* co-
827 expressing HEK293T cells for 16 hours, before cell lysates were collected for bioluminescence
828 assay and immunoblotting. Cells co-expressing SARS-CoV-2 spike and Zsgreen, were co-

829 cultured with ACE2 expressing HEK293T cells for 16 hours before fluorescence imaging. **(B)**
830 Luciferase activity (RLU) measured from HEK293T cell lysates collected from THP-1
831 supernatants-treated HEK293T-S and HEK293T-ACE2 described in (A) for 16 hours. FBS free
832 RPMI 1640 served as medium control. Data are representative of six individual repeats and
833 displayed as individual points with mean \pm standard error of the mean (SEM). **(C)** Immunoblots
834 showing full-length spike, S2, cleaved S2' and ACE2 collected from THP-1 supernatants-treated
835 HEK293T-S and HEK293T-ACE2 described in (A) for 16 hours. Blots are representative of three
836 independent experiments. Numbers below the blots indicated the intensity of S2' versus Tubulin.
837 **(D)** Representative fluorescent image captured at 488 nm from THP-1 supernatants-treated
838 HEK293T-S-ZsGreen and HEK293T-ACE2 for 16 hours. **(E)** Schematic presentation of THP-1
839 supernatants pre-treatment on authentic SARS-CoV-2 infected cells. Pre-treatment of HEK293T-
840 ACE2 cells with THP-1 supernatants for 1 hour, then inoculated with 0.5 multiplicity of infection
841 (MOI) Delta or WT authentic SARS-CoV-2 virus. Imaging was performed at 24 hours post-
842 infection (hpi) before cell lysates were harvested for immunoblotting. **(F)** Immunoblots of Delta
843 SARS-CoV-2 S, S2, cleaved S2', N and ACE2 proteins collected from HEK293T-ACE2 cells 24
844 hpi as described in (E). Blots are representative of three individual experiments. Numbers below
845 the blots indicated the intensity of S2' or N versus Tubulin. **(G)** Immunoblots of WT SARS-CoV-2
846 S, S2, cleaved S2' and N proteins collected from Caco-2 cells 24 hpi as described in (E). Blots
847 are representative of three individual experiments. Numbers below the blots indicated the
848 intensity of S2' or N versus β -Actin. **(H)** Immunofluorescent images showing morphology of
849 SARS-CoV-2 infected Caco-2 cells pre-treated with THP-1 supernatants. Anti-SARS-CoV-2 N
850 was stained with Alexa fluor 555, and nuclei were counterstained with DAPI, respectively. White
851 arrow heads (D and H) indicate syncytia formation or infected cells, scale bars are indicative of 50
852 μ m and images are representative of three independent experiments. **(I)** Quantification of the
853 infected area in (H).

Figure 2



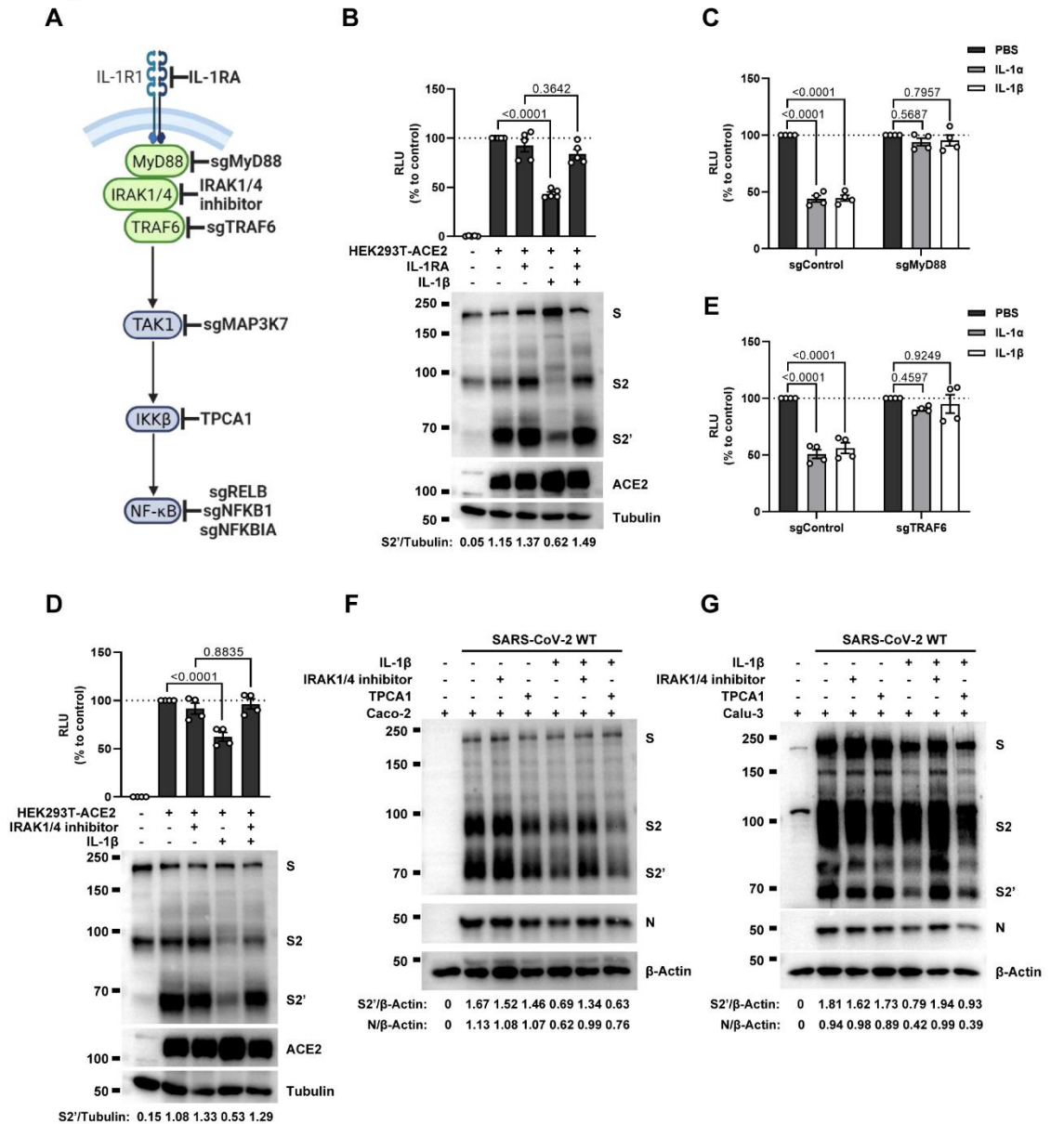
854
855

Figure 2. IL-1 β inhibits SARS-CoV-2-induced cell-cell fusion.

856 (A) Schematics of the cell-cell fusion model used to quantify spike-mediated syncytium formation
857 upon treatment with different cytokines. Cells co-expressing SARS-CoV-2 spike and Cre, were
858 co-cultured with ACE2 and *Stop-luc* co-expressing HEK293T cells for 16 hours, before cell
859 lysates were collected for bioluminescence assay and immunoblotting. Cells co-expressing
860 SARS-CoV-2 spike and ZsGreen, were co-cultured with ACE2 expressing HEK293T cells for 16
861 hours before fluorescence imaging. (B) Luciferase activity (RLU) measured from HEK293T cell
862 lysates collected from different cytokines-treated HEK293T-S and HEK293T-ACE2 described in

863 (A) for 16 hours. IL-1 α (10 ng/mL), IL-1 β (1 ng/mL), IL-6 (100 ng/mL) or IL-8 (100 ng/mL) were
864 added into the cell-cell fusion system. Data are representative of six individual repeats and
865 displayed as individual points with mean \pm SEM. (C) Luciferase activity (RLU) measured from
866 HEK293T cell lysates collected from different concentrations of IL-1 β -treated HEK293T-S and
867 HEK293T-ACE2 for 16 hours. Data are representative of six individual repeats and displayed as
868 individual points with mean \pm SEM. (D) Immunoblots showing full-length spike, S2, cleaved S2'
869 and ACE2 collected from different concentrations of IL-1 β -treated HEK293T-S and HEK293T-
870 ACE2 for 16 hours. Blots are representative of three independent experiments. Numbers below
871 the blots indicated the intensity of S2' versus Tubulin. (E) Schematic presentation of IL-1 β pre-
872 treatment on authentic SARS-CoV-2 infected cells. Pre-treatment of HEK293T-ACE2 cells with
873 different concentrations of IL-1 β for 1 hour, then inoculated with 0.5 MOI Delta or WT authentic
874 SARS-CoV-2 virus. Brightfield images were captured at 24 hours post-infection (hpi) before cell
875 lysates were harvested for immunoblotting. (F) Immunoblots of Delta SARS-CoV-2 S, S2, cleaved
876 S2', N and ACE2 proteins collected from HEK293T-ACE2 cells 24 hpi as described in (E). Blots
877 are representative of three individual experiments. Numbers below the blots indicated the
878 intensity of S2' or N versus Tubulin. (G) Immunoblots of WT SARS-CoV-2 S, S2, cleaved S2' and
879 N proteins collected from Caco-2 cells 24 hpi as described in (E). Blots are representative of
880 three individual experiments. Numbers below the blots indicated the intensity of S2' or N versus
881 β -Actin. (H) Immunofluorescent images showing morphology of SARS-CoV-2-infected Caco-2
882 cells pre-treated with or without IL-1 β . Anti-SARS-CoV-2 N was stained with Alexa fluor 555, and
883 nuclei were counterstained with DAPI, respectively. White arrow heads indicate syncytia
884 formation or infected cells, scale bars are indicative of 50 μ m and images are representative of
885 three independent experiments. (I) Quantification of the infected area in (H). (J) Luciferase
886 activity (RLU) measured from THP-1 supernatants-treated HEK293T-S and HEK293T-ACE2 in
887 the presence or absence of IL-1RA. Data are representative of four individual repeats and
888 displayed as individual points with mean \pm SEM.

Figure 3

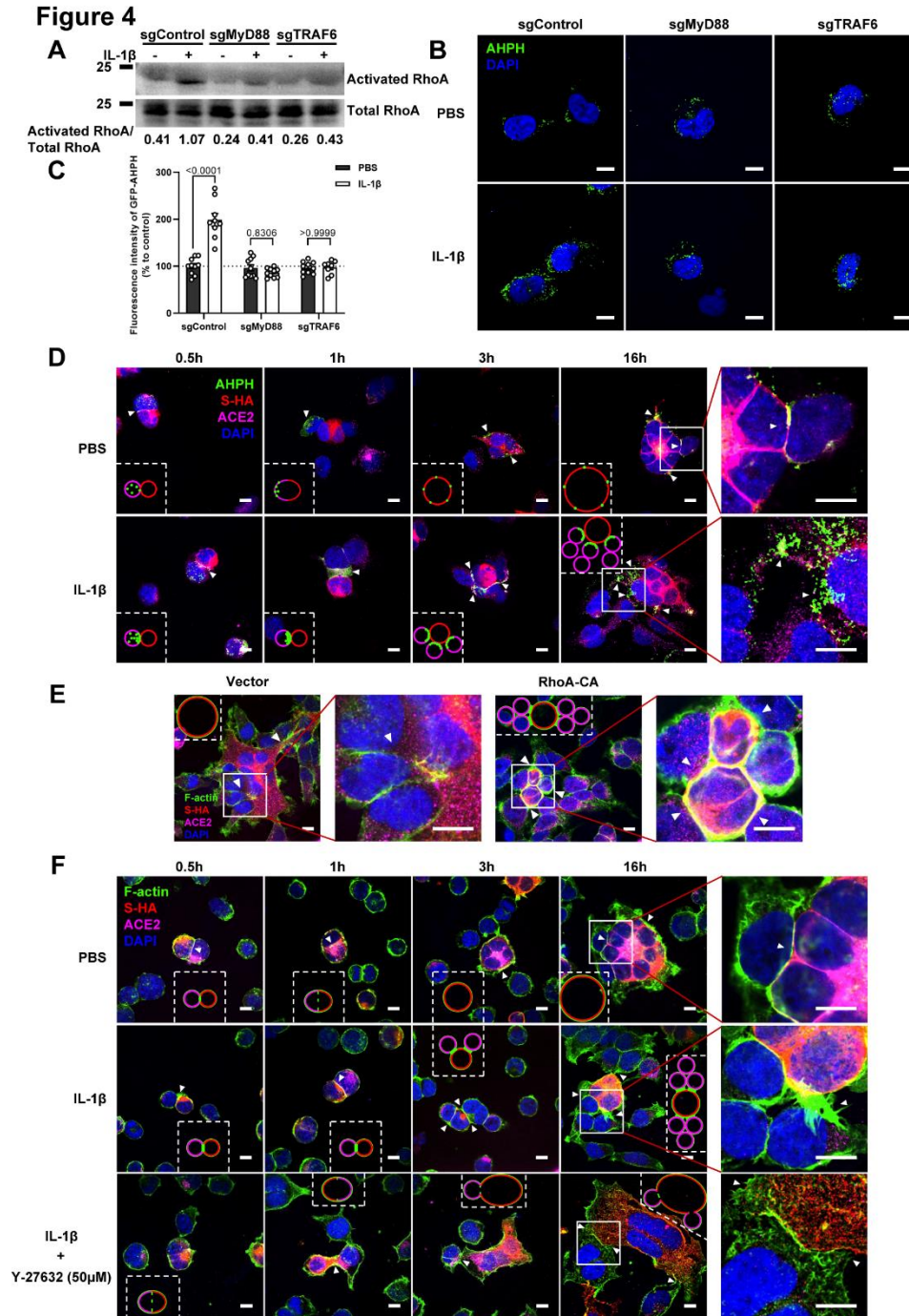


889
890
891

Figure 3. IL-1β inhibits SARS-CoV-2-induced cell-cell fusion through the IL-1R1/MyD88/IRAK/TRAF6 pathway.

892 (A) Schematics of gene knockout or inhibitor treatment in the IL-1 receptor pathway. (B)
893 Luciferase activity (RLU) measured from HEK293T cell lysates and immunoblots showing full-
894 length spike, S2, cleaved S2' and ACE2 collected from HEK293T-S and HEK293T-ACE2 pre-
895 treated with 1000 ng/mL IL-1RA for 30 min, then treated with 1 ng/mL IL-1β for 16 hours. Data
896 and blots are representative of five individual repeats. Numbers below the blots indicated the
897 intensity of S2' versus Tubulin. (C) Luciferase activity (RLU) measured from cell lysates collected
898 from 10 ng/mL IL-1α or 1 ng/mL IL-1β-treated sgControl or sgMyD88 HEK293T cell-cell fusion
899 system for 16 hours. Data are representative of four individual repeats and displayed as individual
900 points with mean ±SEM. (D) Luciferase activity (RLU) measured from HEK293T cell lysates and
901 immunoblots showing full-length spike, S2, cleaved S2' and ACE2 collected from HEK293T-S
902 and HEK293T-ACE2 pre-treated with 2μM IRAK1/4 inhibitor for 30 min, then treated with 1 ng/mL

903 IL-1 β for 16 hours. Data and blots are representative of four individual repeats. Numbers below
904 the blots indicated the intensity of S2' versus Tubulin. **(E)** Luciferase activity (RLU) measured
905 from cell lysates collected from 10 ng/mL IL-1 α or 1 ng/mL IL-1 β -treated sgControl or sgTRAF6
906 HEK293T cell-cell fusion system for 16 hours. Data are representative of four individual repeats
907 and displayed as individual points with mean \pm SEM. **(F)** Immunoblots showing full-length spike,
908 S2, cleaved S2' and N collected from Caco-2 cells, which were pre-treated with 2 μ M IRAK1/4
909 inhibitor and 10 ng/mL IL-1 β for 1 hour, then infected with authentic SARS-CoV-2 for 24 hours.
910 Blots are representative of three independent experiments. Numbers below the blots indicated
911 the intensity of S2' or N versus β -Actin. **(G)** Immunoblots showing full-length spike, S2, cleaved
912 S2' and N collected from Calu-3 cells, which were infected with authentic SARS-CoV-2 for 1 hour,
913 then washed with PBS before treated with 2 μ M IRAK1/4 inhibitor and 10 ng/mL IL-1 β for 24
914 hours. Blots are representative of three independent experiments. Numbers below the blots
915 indicated the intensity of S2' or N versus β -Actin.



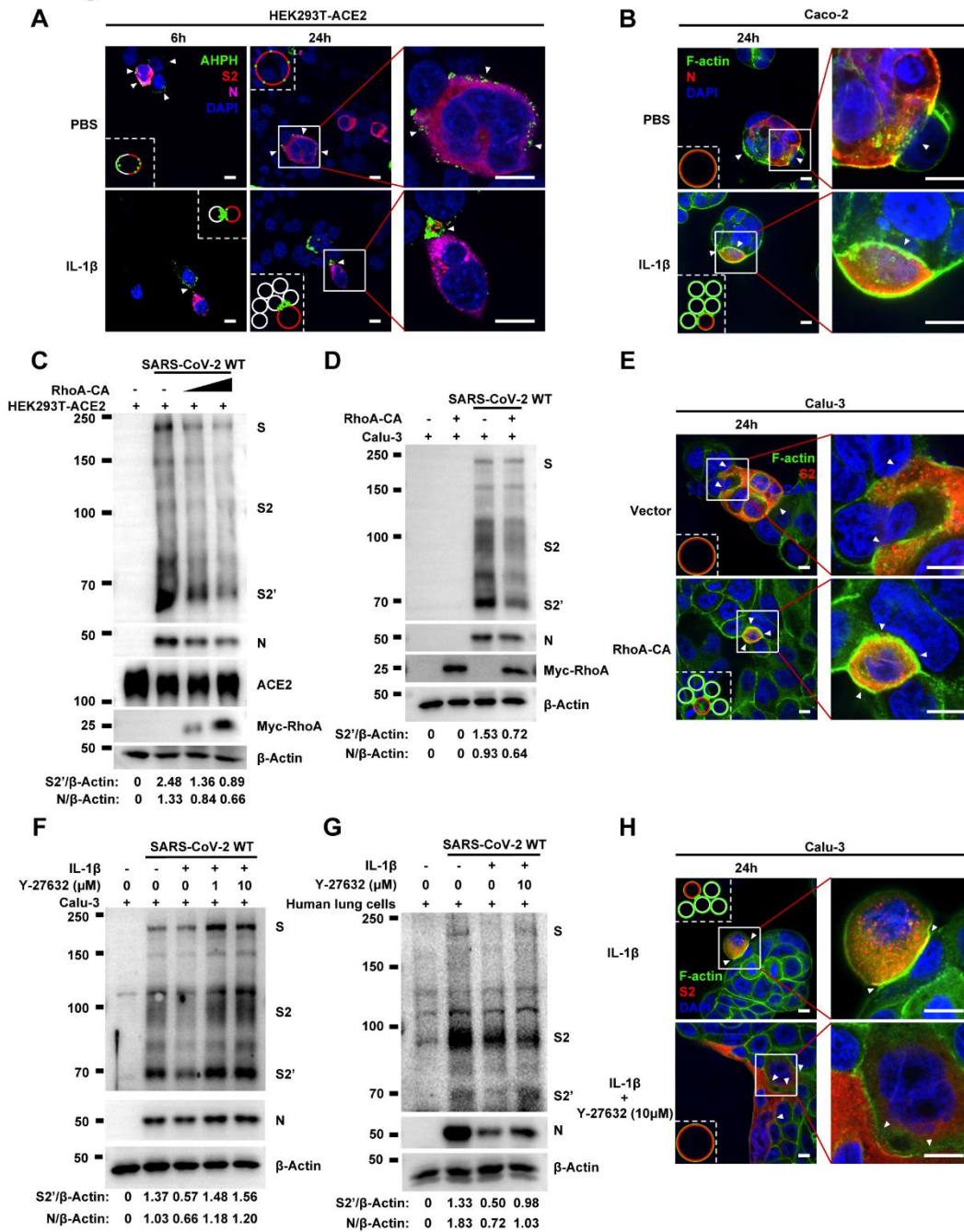
916
917
918

Figure 4. IL-1 β inhibits SARS-CoV-2-induced cell-cell fusion through RhoA/ROCK mediated actin bundles assembly at cell-cell junction.

919 (A) GTP-RhoA pull-down assay to detect the active level of RhoA in sgControl, sgMyD88 and
920 sgTRAF6 HEK293T cells after 1 ng/mL IL-1 β treatment for 30 min. Immunoblots showing
921 activated RhoA and total RhoA. Blots are representative of three independent experiments.
922 Numbers below the blots indicated the intensity of active RhoA versus total RhoA. (B)
923 Representative confocal images of GFP-AHPH after 1 ng/mL IL-1 β treatment for 30 min in
924 sgControl, sgMyD88 and sgTRAF6 HEK293T cells. Scale bars, 10 μ m. (C) Quantification of

925 fluorescence intensity of GFP-AHPH in (B). Data are representative of eight individual repeats.
926 **(D)** Representative confocal images of GFP-AHPH localization with or without 1 ng/mL IL-1 β
927 treatment at different time points of syncytia formation in HEK293T-S-HA and HEK293T-ACE2
928 cells. Schematics with green dots in the white dashed line boxes representing GFP-AHPH, red
929 cycles representing S-expressing cells, and magenta cycles representing ACE2-expressing cells.
930 White arrow heads indicate the localization of GFP-AHPH, scale bars, 10 μ m. Images are
931 representative of three independent experiments. **(E)** Representative confocal images of F-actin
932 stained with phalloidin-488 in transfected vector or 20 ng RhoA-CA HEK293T-S-HA and
933 HEK293T-ACE2 cells. Schematics with green lines in the white dashed line boxes representing
934 actin bundles, red cycles representing S-expressing cells, and magenta cycles representing
935 ACE2-expressing cells. Scale bars, 10 μ m. Images are representative of three independent
936 experiments. **(F)** Representative confocal images of F-actin stained with phalloidin-488 in the
937 presence or absence of 1 ng/mL IL-1 β or 50 μ M Y-27632 treatment at different time points of
938 syncytia formation in HEK293T-S-HA and HEK293T-ACE2 cells. Schematics with green lines in
939 the white dashed line boxes representing actin bundles, red cycles representing S-expressing
940 cells, and magenta cycles representing ACE2-expressing cells. White arrow heads (E and F)
941 indicate the enrichment or disappearance of F-actin, scale bars, 10 μ m. Images are
942 representative of three independent experiments.

Figure 5



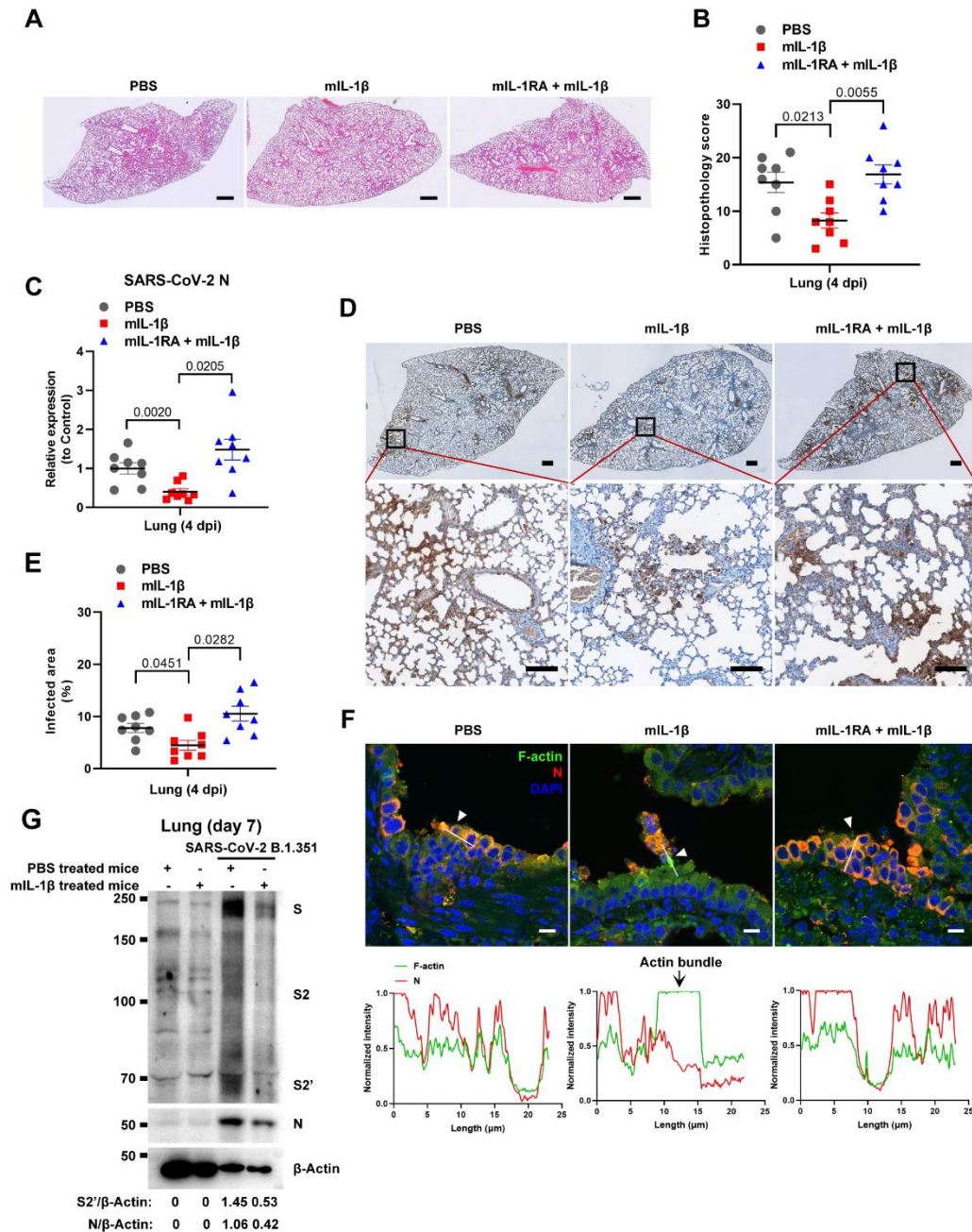
943
944
945

Figure 5. Activation of RhoA/ROCK pathway prevents authentic SARS-CoV-2-induced cell-cell fusion via forming actin bundles.

946 (A) Representative confocal images of GFP-AHPH localization with or without 1 ng/mL IL-1β
947 treatment in 0.5 MOI WT authentic SARS-CoV-2 infected HEK293T-ACE2 cells at 6 hpi and
948 hpi. Schematics with green dots in the white dashed line boxes representing GFP-AHPH, red
949 cycles representing SARS-CoV-2 infected cells, and white cycles representing neighboring cells.
950 White arrow heads indicate the localization of GFP-AHPH, scale bars, 10 μm. Images are
951 representative of three independent experiments. (B) Representative confocal images of F-actin

952 stained with phalloidin-488 in the presence or absence of 1 ng/mL IL-1 β treatment upon 0.5 MOI
953 WT authentic SARS-CoV-2 infection of Caco-2 cells at 24 hpi. Schematics with green lines in the
954 white dashed line boxes representing actin bundles, red cycles representing SARS-CoV-2-
955 infected cells, and white cycles representing neighboring cells. Scale bars, 10 μ m. Images are
956 representative of three independent experiments. **(C)** Immunoblots of WT SARS-CoV-2 S, S2,
957 cleaved S2', N and Myc-RhoA collected from HEK293T-ACE2 cells, which were transfected with
958 vector, 10 ng or 20 ng RhoA-CA before infection with 0.5 MOI authentic SARS-CoV-2 WT strain
959 for 24 hours. Blots are representative of three individual experiments. Numbers below the blots
960 indicated the intensity of S2' or N versus β -Actin. **(D)** Immunoblots of WT SARS-CoV-2 S, S2,
961 cleaved S2', N and Myc-RhoA collected from lentivirus-transduced Calu-3 cells expressing vector
962 or RhoA-CA, infected with WT authentic SARS-CoV-2 for 24 hours. Blots are representative of
963 three individual experiments. Numbers below the blots indicated the intensity of S2' or N versus
964 β -Actin. **(E)** Representative confocal images of F-actin stained with phalloidin-488 from Calu-3
965 cells described in (D). Schematics with green lines in the white dashed line boxes representing
966 actin bundles, red cycles representing S-expressing cells, scale bars, 10 μ m. Images are
967 representative of four independent experiments. **(F, G)** Immunoblots of WT SARS-CoV-2 S, S2,
968 cleaved S2' and N collected from Calu-3 cells **(F)** or primary human lung cells **(G)**, which were
969 infected with authentic SARS-CoV-2 for 1 hour, then washed with PBS before being treated with
970 different concentrations of Y-27632 and 10 ng/mL IL-1 β for 24 hours. Blots are representative of
971 three independent experiments. Numbers below the blots indicated the intensity of S2' or N
972 versus β -Actin. **(H)** Representative confocal images of F-actin stained with phalloidin-488 in Calu-
973 3 cells described in (F). Schematics with green lines in the white dashed line boxes representing
974 actin bundles, red cycles representing S-expressing cells. White arrow heads (B, E and H)
975 indicate the enrichment or disappearance of F-actin, scale bars, 10 μ m. Images are
976 representative of four independent experiments.

Figure 6



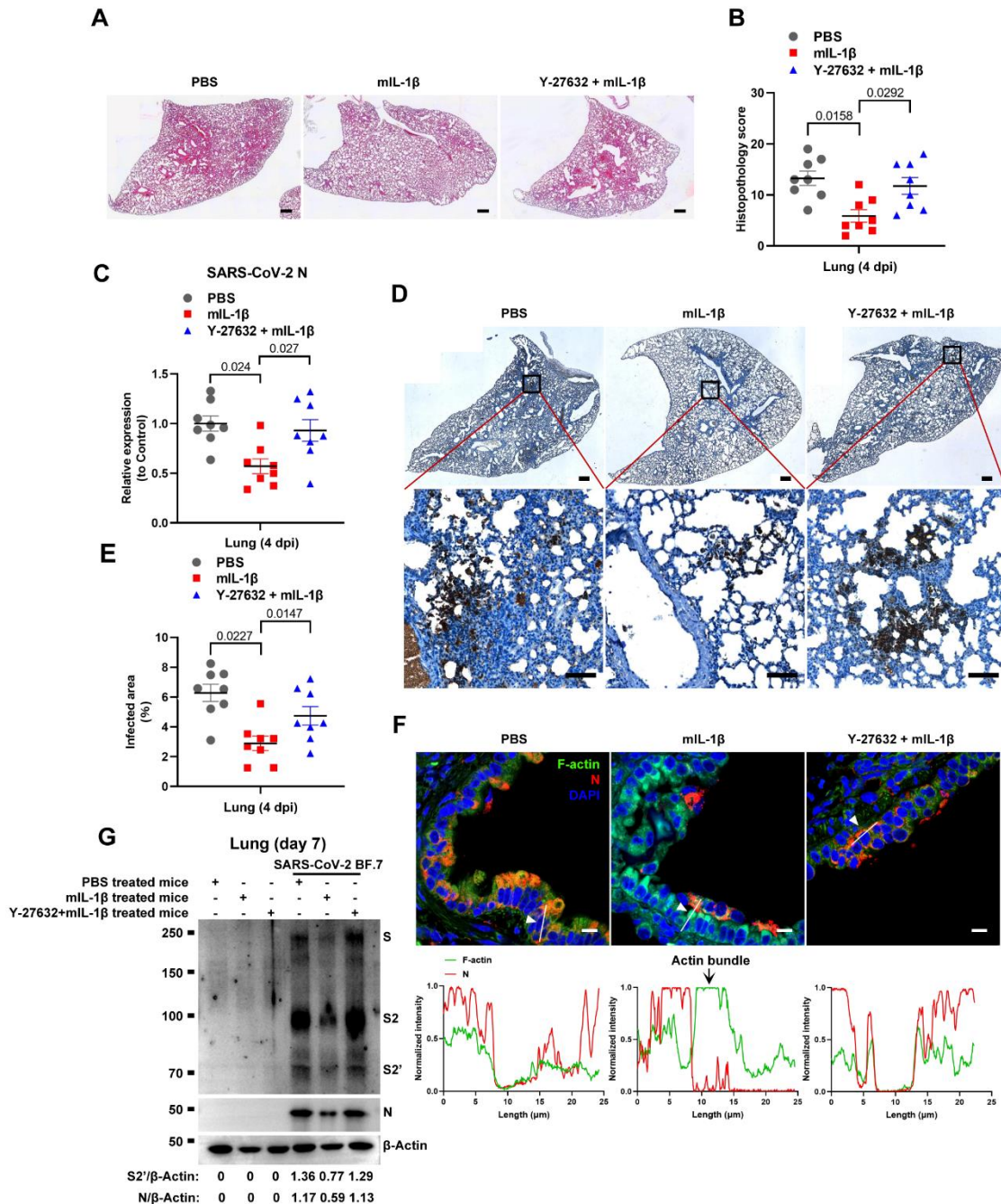
977
978
979

Figure 6. IL-1 β restricts SARS-CoV-2 transmission via induction of actin bundles in the lung *in vivo*.

980 (A, B) Representative images of H&E-stained lung sections (A) and histopathology scores (B)
981 from PBS; 1 μ g/kg mL-1 β ; 150 μ g/kg mL-1RA + mL-1 β pre-treated mice infected with SARS-
982 CoV-2 at 4 days post-infection (dpi), scale bars are indicative of 500 μ m and images are
983 representative of eight samples. (C) qPCR analysis of SARS-CoV-2 N mRNA collected from
984 infected lung tissues at 4 dpi. (D) Immunohistochemistry analysis of SARS-CoV-2 N staining in
985 the lung tissue slices at 4 dpi, scale bars are indicative of 500 μ m (top panel), 50 μ m (bottom

986 panel) and images are representative of eight samples. **(E)** The percentages of SARS-CoV-2-
987 infected area in **(D)** were quantified. **(F)** Representative confocal images of F-actin stained with
988 phalloidin-488 and SARS-CoV-2 N in the area 1 of lung tissue at 4 dpi. White arrow heads
989 indicate syncytia formation or infected cells, scale bars are indicative of 10 μm and images are
990 representative of three samples (Top). White lines indicate SARS-CoV-2 cell-cell transmission
991 and quantify with fluorescence intensity of F-actin and SARS-CoV-2 N (Bottom). **(G)** Immunoblots
992 of SARS-CoV-2 S, S2, cleaved S2' and N proteins collected from SARS-CoV-2 B.1.351-infected
993 lung tissue cells, which were isolated from BALB/c mice treated with or without 1 $\mu\text{g}/\text{kg}$ mL-1 β at
994 day 7. Blots are representative of three individual mouse. Numbers below the blots indicated the
995 intensity of S2' or N versus β -Actin.

Figure 7



996
997
998

Figure 7. Prevention of IL-1β-induced actin bundles by ROCK inhibitor Y-27632 promotes SARS-CoV-2 transmission *in vivo*.

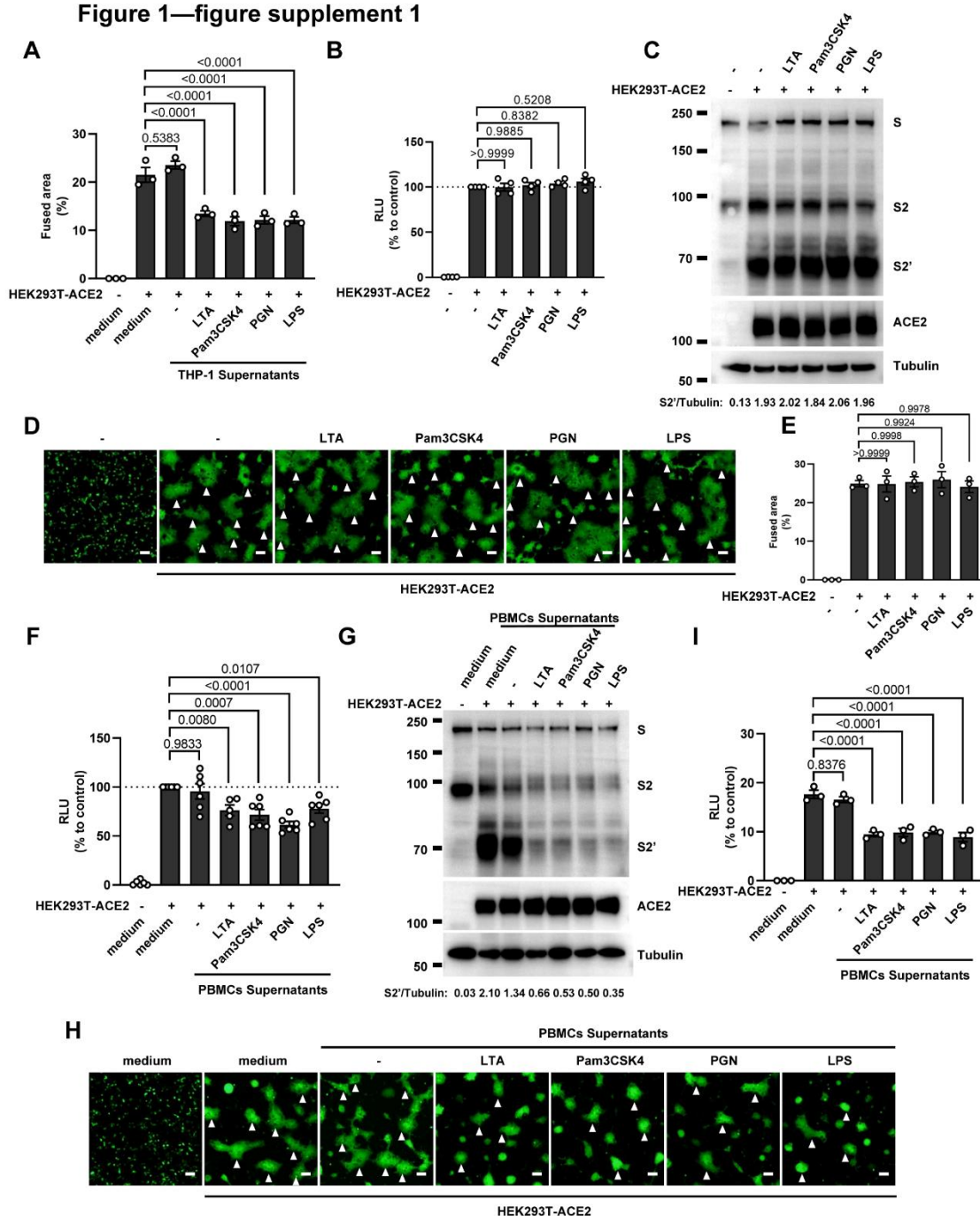
999 (A, B) Representative images of H&E-stained lung sections (A) and histopathology scores (B)
 1000 from PBS; 1 μg/kg mL-1β; 1mg/kg Y-27632 + mL-1β pre-treated mice infected with SARS-CoV-
 1001 2 at 4 days post-infection (dpi), scale bars are indicative of 500 μm and images are
 1002 representative of eight samples. (C) qPCR analysis of SARS-CoV-2 N mRNA collected from
 1003 infected lung tissues at 4 dpi. (D) Immunohistochemistry analysis of SARS-CoV-2 N staining in
 1004 the lung tissue slices at 4 dpi, scale bars are indicative of 500 μm (top panel), 50 μm (bottom

1005 panel) and images are representative of eight samples. (E) The percentages of SARS-CoV-2
1006 infected area in (D) were quantified. (F) Representative confocal images of F-actin stained with
1007 phalloidin-488 and SARS-CoV-2 N in the area 1 of lung tissue at 4 dpi. White arrow heads
1008 indicate syncytia formation or infected cells, scale bars are indicative of 10 μ m and images are
1009 representative of three samples (Top). White lines indicate SARS-CoV-2 cell-cell transmission
1010 and quantify with fluorescence intensity of F-actin and SARS-CoV-2 N (Bottom). (G) Immunoblots
1011 of SARS-CoV-2 S, S2, cleaved S2' and N proteins collected from authentic SARS-CoV-2 BF.7-
1012 infected lung tissue cells, which were isolated from BALB/c mice treated with PBS, 1 μ g/kg mL-
1013 1 β or 1mg/kg Y-27632 + 1 μ g/kg mL-1 β at day 7. Blots are representative of three individual
1014 mouse. Numbers below the blots indicated the intensity of S2' or N versus β -Actin.

1015

Supplemental Figures

Figure 1—figure supplement 1



1016

1017

1018

Figure 1—figure supplement 1. Host factors secreted by activated PBMCs inhibit SARS-CoV-2 spike-induced cell-cell fusion, but TLR ligands alone have no effect.

1019

1020

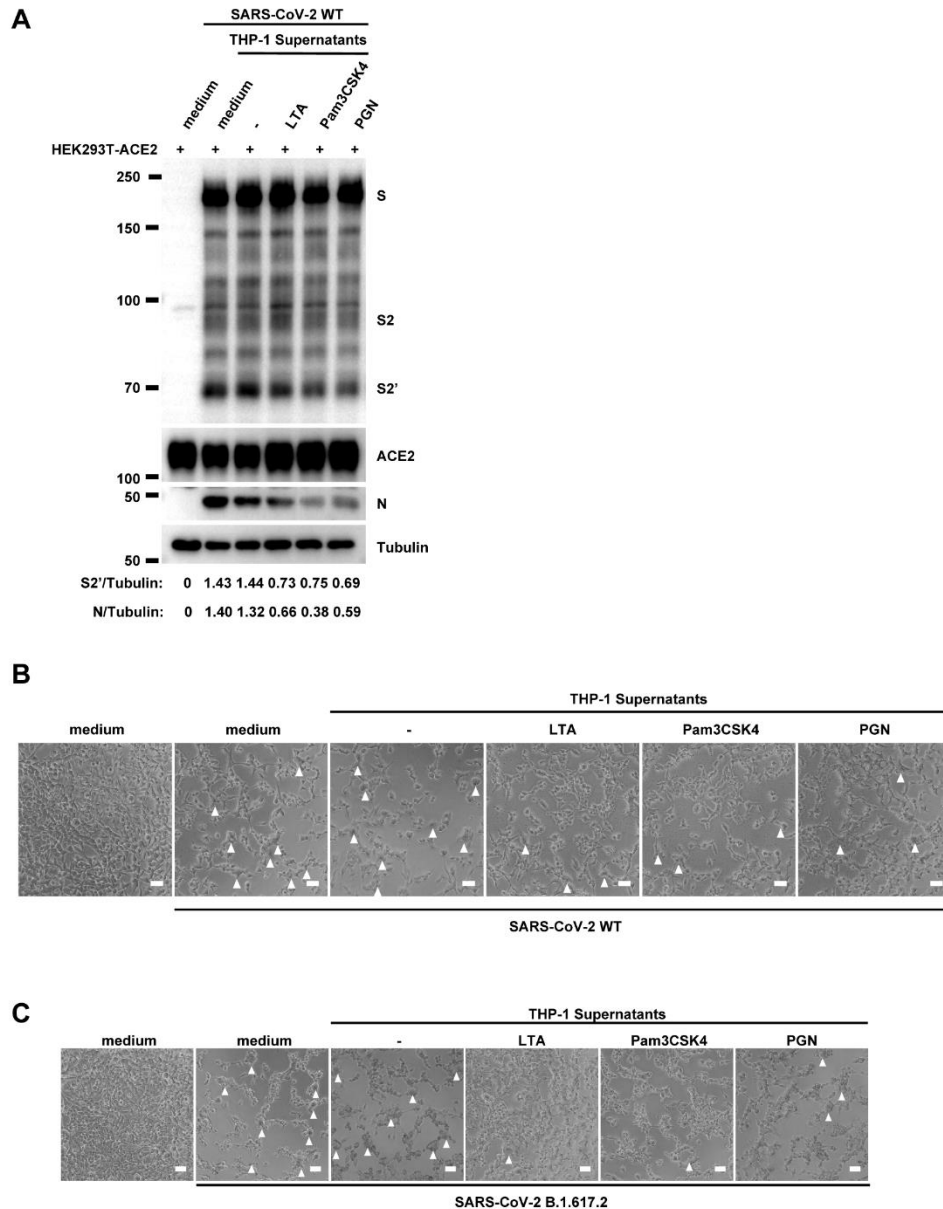
1021

1022

(A) Quantification of the fused area in Figure 1D. (B) Luciferase activity (RLU) measured from HEK293T cell lysates collected from TLR ligands treated HEK293T-S and HEK293T-ACE2 for 16 hours. Data are representative of four individual repeats and displayed as individual points with mean ± standard error of the mean (SEM). (C) Immunoblots showing full-length spike, S2,

1023 cleaved S2' and ACE2 collected from TLR ligands-treated HEK293T-S and HEK293T-ACE2 for
1024 16 hours. Blots are representative of three independent experiments. Numbers below the blots
1025 indicated the intensity of S2' versus Tubulin. **(D)** Representative fluorescent image captured at
1026 488 nm from TLR ligands treated HEK293T-S-Zsgreen and HEK293T-ACE2 for 16 hours. **(E)**
1027 Quantification of the infected area in (D). **(F)** Luciferase activity (RLU) measured from HEK293T
1028 cell lysates collected from PBMCs supernatants-treated HEK293T-S and HEK293T-ACE2 for 16
1029 hours. 1% FBS RPMI 1640 served as medium control. Data are representative of five individual
1030 repeats and displayed as individual points with mean \pm SEM. **(G)** Immunoblots showing full-length
1031 spike, S2, cleaved S2' and ACE2 collected from PBMCs supernatants-treated HEK293T-S and
1032 HEK293T-ACE2 for 16 hours. Blots are representative of three independent experiments.
1033 Numbers below the blots indicated the intensity of S2' versus Tubulin. **(H)** Representative
1034 fluorescent image captured at 488 nm from PBMCs supernatants-treated HEK293T-S-Zsgreen
1035 and HEK293T-ACE2 for 16 hours. White arrow heads (D and H) indicate syncytia formation.
1036 Scale bars, 50 μ m. Images are representative of three individual repeats. **(I)** Quantification of the
1037 fused area in (H).

Figure 1—figure supplement 2

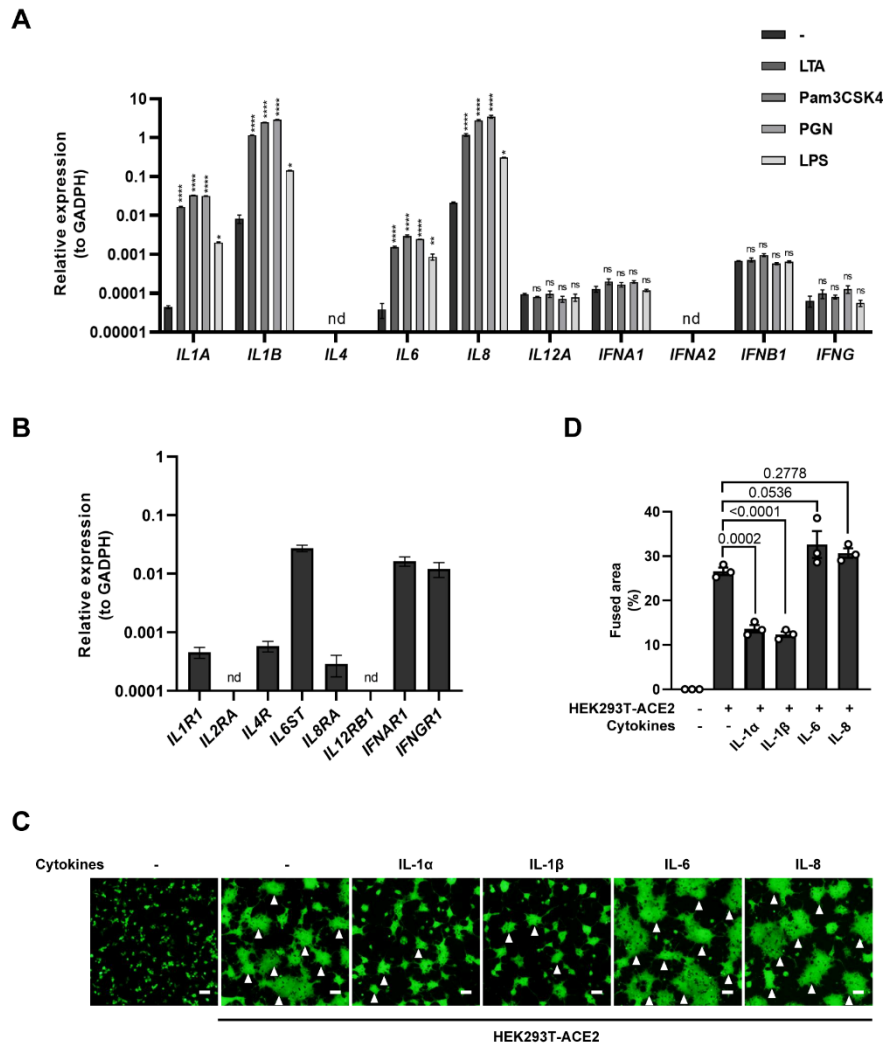


1038
1039
1040

Figure 1—figure supplement 2. Host factors secreted by activated THP-1 cells inhibit authentic SARS-CoV-2-induced cell-cell fusion.

1041 (A) Immunoblots of WT SARS-CoV-2 S, S2, cleaved S2' and N proteins collected from HEK293T-
1042 ACE2 cells 24 hpi as described in Figure 1E. Blots are representative of three individual
1043 experiments. Numbers below the blots indicated the intensity of S2' or N versus Tubulin. (B, C)
1044 Bright field images of 0.5 MOI WT (B) or Delta (C) SARS-CoV-2-infected HEK293T-ACE2 cells
1045 pre-treated with THP-1 supernatants. White arrow heads indicate syncytia formation, scale bars
1046 are indicative of 50 μ m, and images are representative of three independent experiments.

Figure 2—figure supplement 1



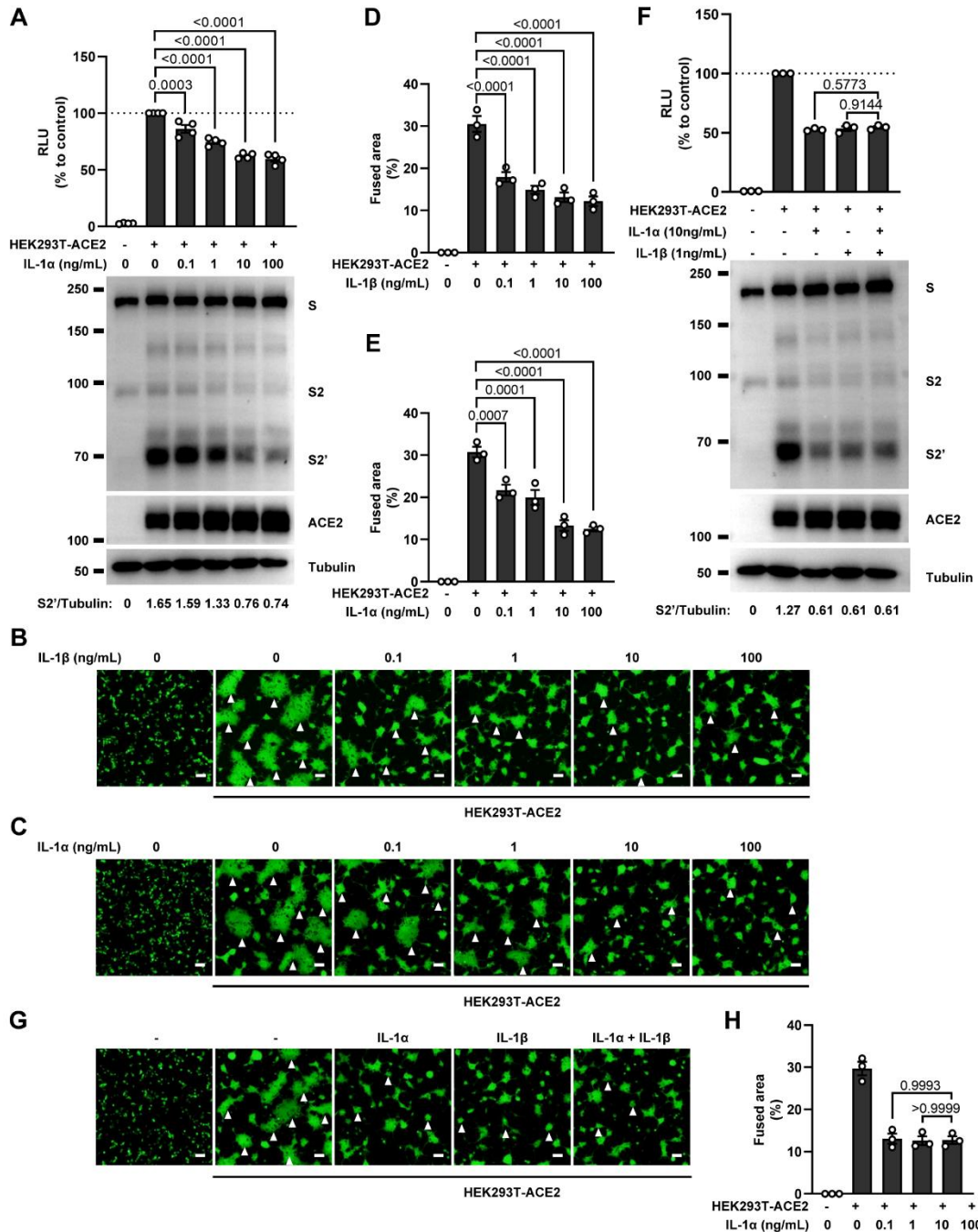
1047
1048
1049
1050

Figure 2—figure supplement 1. mRNA levels of different cytokine genes in THP-1 cells and selected cytokine receptor genes in HEK293T cells, as well as fluorescent images indicating cell-cell fusion in the presence of indicated cytokines.

1051
1052
1053
1054
1055
1056
1057

(A) mRNA levels of different cytokine genes in THP-1 cells after TLR ligands stimulation for 4 hours. Data are representative of three individual repeats. (B) mRNA levels of indicated cytokine receptor genes in HEK293T cells. Data are representative of five individual repeats. (C) Representative fluorescent image captured at 488 nm from different cytokines-treated HEK293T-S-ZsGreen and HEK293T-ACE2 for 16 hours. White arrow heads indicate syncytia formation. Scale bars, 50 μ m. Images are representative of three individual repeats. (D) Quantification of the fused area in (C).

Figure 2—figure supplement 2



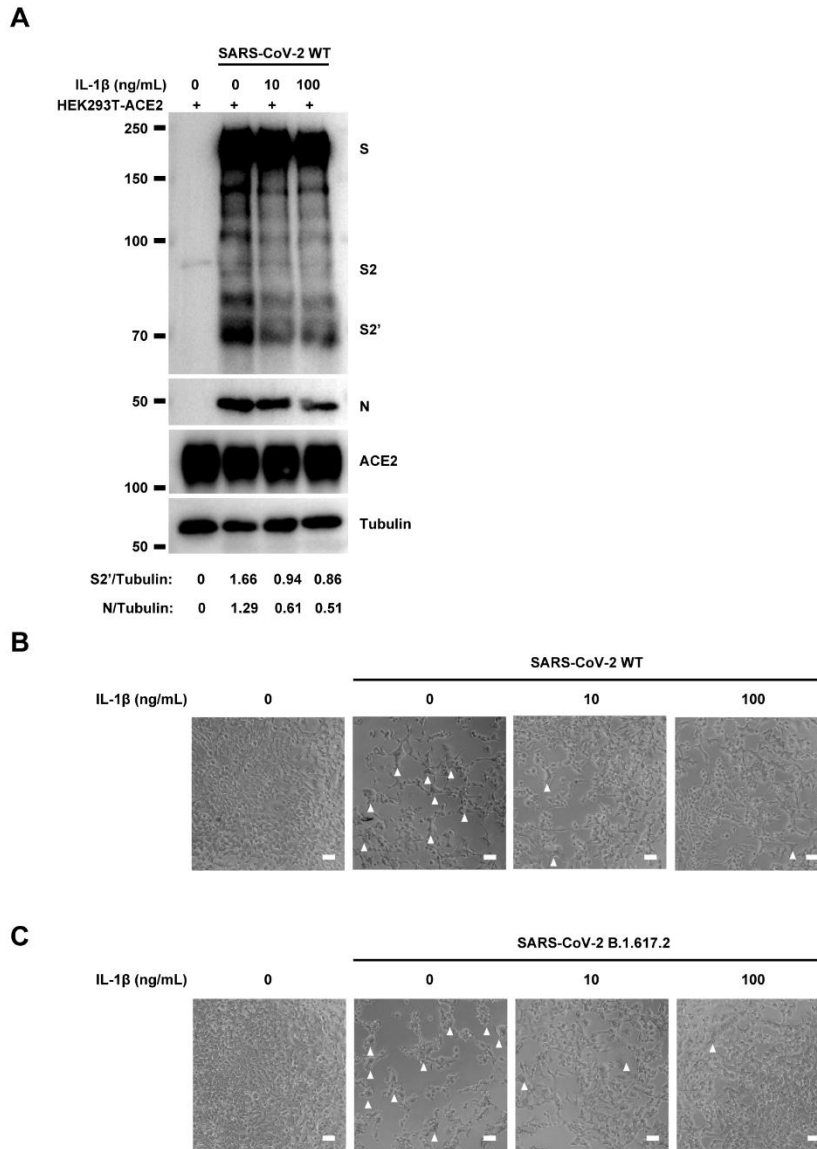
1058
1059
1060

Figure 2—figure supplement 2. No synergistic inhibition of SARS-CoV-2 spike-induced cell-cell fusion by IL-1α and IL-1β co-treatment.

1061 (A) Luciferase activity (RLU) measured from HEK293T cell lysates and immunoblots showing full-
1062 length spike, S2, cleaved S2' and ACE2 collected from different concentrations of IL-1α-treated
1063 HEK293T-S and HEK293T-ACE2 for 16 hours. Data and blots are representative of four
1064 individual repeats. Numbers below the blots indicated the intensity of S2' versus Tubulin. (B, C)
1065 Representative fluorescent image captured at 488 nm from different concentrations of IL-1β (B)
1066 or IL-1α (C) treated HEK293T-S-ZsGreen and HEK293T-ACE2 for 16 hours. (D) Quantification of

1067 the fused area in (B). **(E)** Quantification of the fused area in (C). **(F)** Luciferase activity (RLU)
1068 measured from HEK293T cell lysates and immunoblots showing full-length spike, S2, cleaved S2'
1069 and ACE2 collected from IL-1 α and IL-1 β co-treated HEK293T-S and HEK293T-ACE2 for 16
1070 hours. Data and blots are representative of three individual repeats. Numbers below the blots
1071 indicated the intensity of S2' versus Tubulin. **(G)** Representative fluorescent image captured at
1072 488 nm from IL-1 α and IL-1 β co-treated HEK293T-S-Zsfgreen and HEK293T-ACE2 for 16 hours.
1073 White arrow heads (B, C and G) indicate syncytia formation. Scale bars, 50 μ m. Images are
1074 representative of three individual repeats. **(E)** Quantification of the fused area in (G).

Figure 2—figure supplement 3

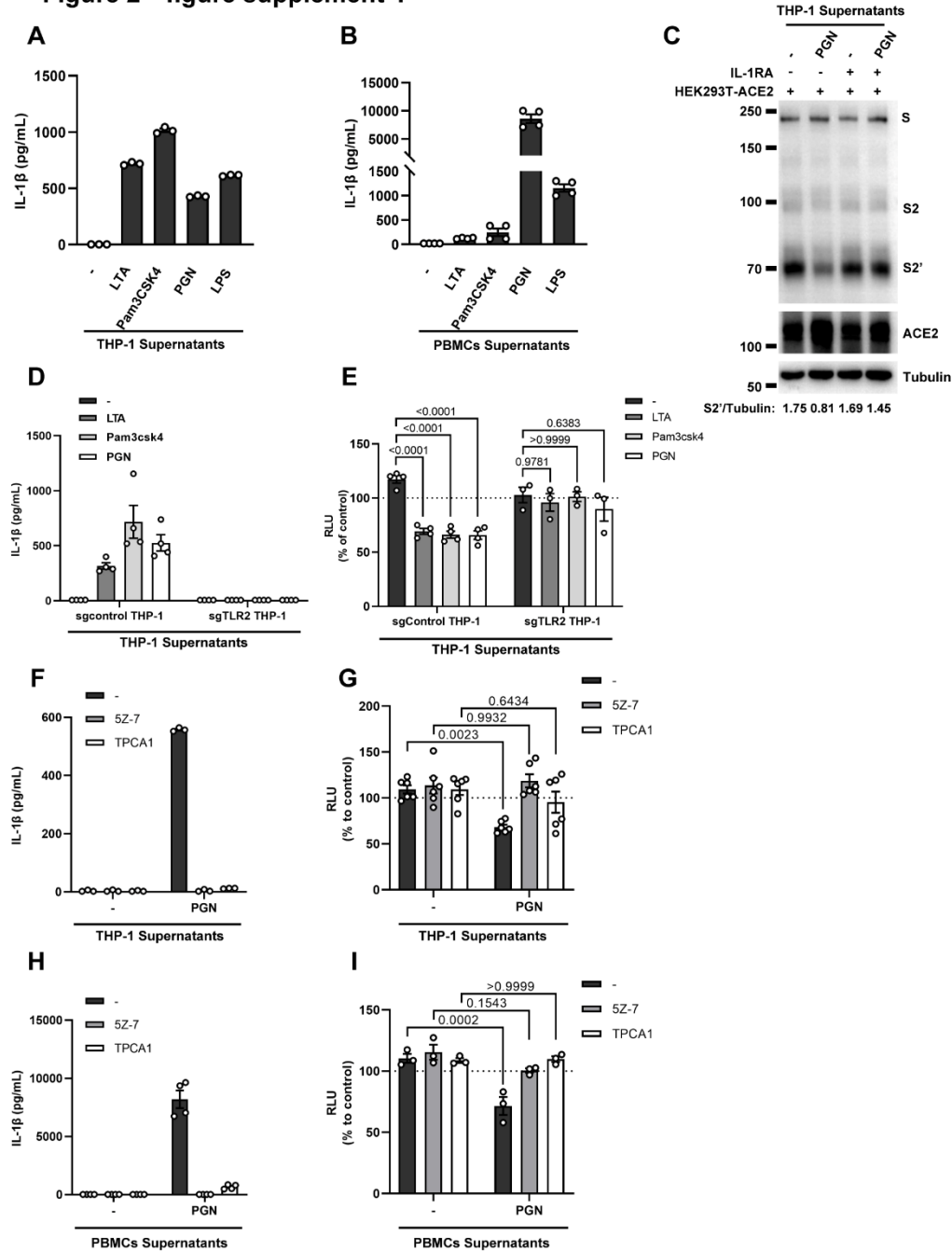


1075
1076
1077

Figure 2—figure supplement 3. IL-1 β inhibits authentic SARS-CoV-2-induced cell-cell fusion.

1078 (A) Immunoblots of WT SARS-CoV-2 S, S2, cleaved S2' and N proteins collected from HEK293T-
1079 ACE2 cells 24 hpi as described in Figure 2E. Blots are representative of three individual
1080 experiments. Numbers below the blots indicated the intensity of S2' or N versus Tubulin. (B, C)
1081 Bright field images of 0.5 MOI WT (B) or Delta (C) SARS-CoV-2 infected HEK293T-ACE2 cells
1082 pre-treated with different concentrations of IL-1 β . White arrow heads indicate syncytia formation,
1083 scale bars are indicative of 50 μ m, and images are representative of three independent
1084 experiments.

Figure 2—figure supplement 4



1085
1086
1087

Figure 2—figure supplement 4. IL-1β is an important host factor from innate immune cells inhibiting SARS-CoV-2 spike-induced cell-cell fusion.

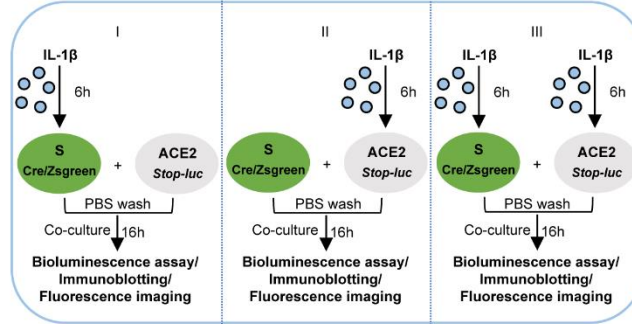
1088
1089
1090
1091
1092
1093

(A, B) ELISA of IL-1β concentrations in supernatants from THP-1 (A) and PBMCs (B) after TLR ligands stimulation. Data are representative of three individual repeats. (C) immunoblots showing full-length spike, S2, cleaved S2' and ACE2 collected from THP-1 supernatants-treated HEK293T-S and HEK293T-ACE2 in the presence or absence of IL-1RA. Blots are representative of three individual repeats. Numbers below the blots indicated the intensity of S2' versus Tubulin. (D) ELISA of IL-1β concentrations in supernatants from sgControl and sgTLR2 THP-1 cells after

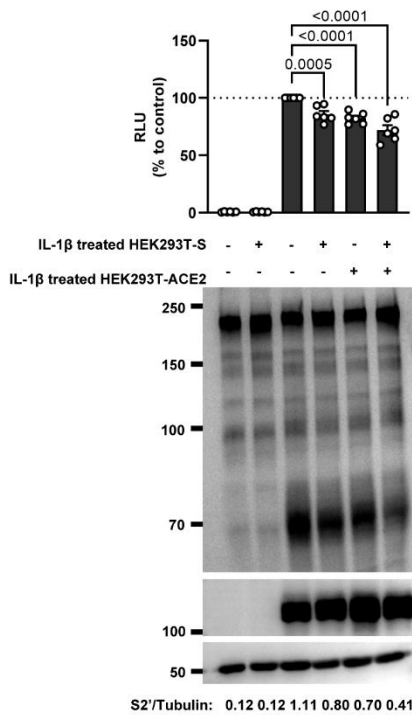
1094 TLR ligands stimulation. Data are representative of four individual repeats. **(E)** Luciferase activity
1095 (RLU) measured from HEK293T cell lysates collected from sgControl and sgTLR2 THP-1
1096 supernatants-treated HEK293T-S and HEK293T-ACE2 for 16 hours. FBS free RPMI 1640 served
1097 as medium control. Data are representative of three individual repeats and displayed as individual
1098 points with mean \pm SEM. **(F)** ELISA of IL-1 β concentrations in supernatants from TAK1/IKK β
1099 inhibitors-treated THP-1 cells after PGN stimulation. Data are representative of three individual
1100 repeats. **(G)** Luciferase activity (RLU) measured from HEK293T cell lysates collected from
1101 TAK1/IKK β inhibitors pre-treated THP-1 supernatants added onto HEK293T-S and HEK293T-
1102 ACE2 cells for 16 hours. FBS free RPMI 1640 served as medium control. Data are representative
1103 of three individual repeats and displayed as individual points with mean \pm SEM. **(H)** ELISA of IL-
1104 1 β concentrations in supernatants from TAK1/IKK β inhibitors-treated PBMCs after PGN
1105 stimulation. Data are representative of three individual repeats. **(I)** Luciferase activity (RLU)
1106 measured from HEK293T cell lysates collected from TAK1/IKK β inhibitors pre-treated PBMCs
1107 supernatants added onto HEK293T-S and HEK293T-ACE2 cells for 16 hours. 1% FBS RPMI
1108 1640 served as medium control. Data are representative of three individual repeats and displayed
1109 as individual points with mean \pm SEM.

Figure 2—figure supplement 5

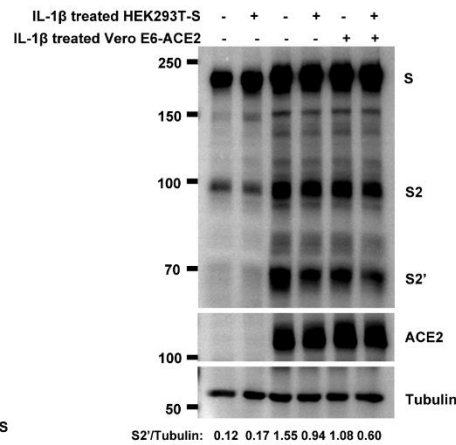
A



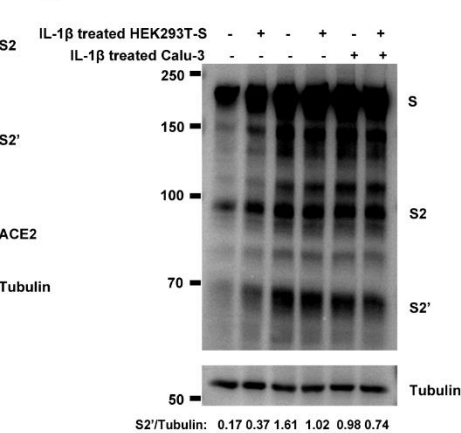
B



C



D



1110
1111
1112

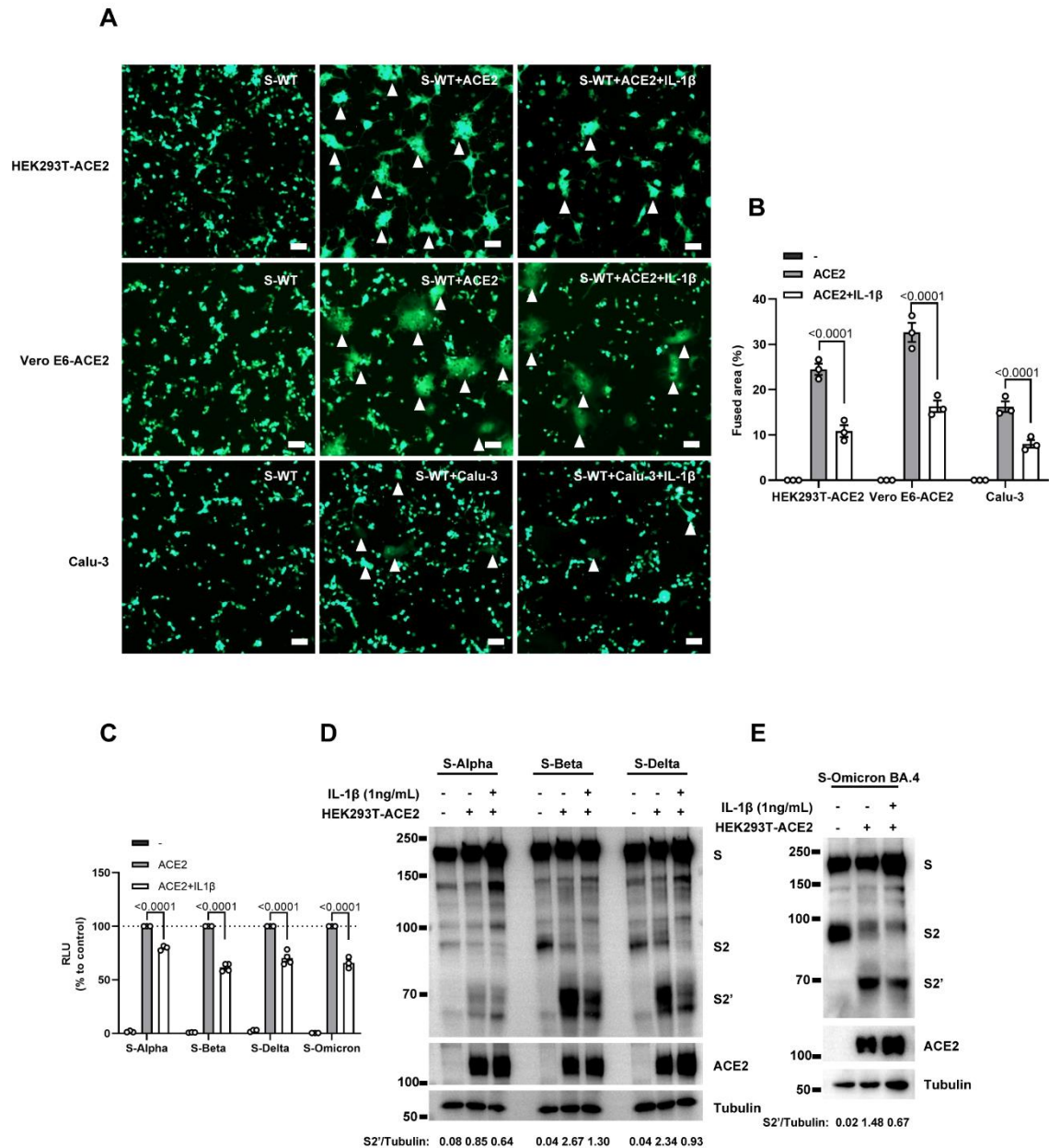
Figure 2—figure supplement 5. IL-1β inhibits SARS-CoV-2-induced cell-cell fusion through acting on both donor and acceptor cells.

1113
1114
1115
1116
1117
1118

(A) Schematics of the cell-cell fusion model used to determine cell types affected by IL-1β. Pre-treated HEK293T-S or HEK293T-ACE2 cells or both with 1 ng/mL IL-1β for 6 hours, then co-cultured for 16 hours after washing with PBS. Cells co-expressing SARS-CoV-2 spike and Cre, were co-cultured with ACE2 and *Stop-luc* co-expressing HEK293T cells for 16 hours, before cell lysates were collected for bioluminescence assay and immunoblotting. Cells co-expressing SARS-CoV-2 spike and Zsgreen, were co-cultured with ACE2 expressing HEK293T cells for 16

1119 hours before fluorescence imaging. **(B)** Luciferase activity (RLU) measured from HEK293T cell
1120 lysates and immunoblots showing full-length spike, S2, cleaved S2' and ACE2 collected from
1121 different treatments of IL-1 β described in (A) for 16 hours. Data and blots are representative of six
1122 individual repeats. Numbers below the blots indicated the intensity of S2' versus Tubulin. **(C)**
1123 Immunoblots showing full-length spike, S2, cleaved S2' and ACE2 collected from 1 ng/mL IL-1 β -
1124 treated HEK293T-S and Vero E6-ACE2 for 16 hours. Blots are representative of three
1125 independent experiments. Numbers below the blots indicated the intensity of S2' versus Tubulin.
1126 **(D)** Immunoblots showing full-length spike, S2 and cleaved S2' collected from 1 ng/mL IL-1 β -
1127 treated HEK293T-S and Calu-3 for 16 hours. Blots are representative of three independent
1128 experiments. Numbers below the blots indicated the intensity of S2' versus Tubulin.

Figure 2—figure supplement 6



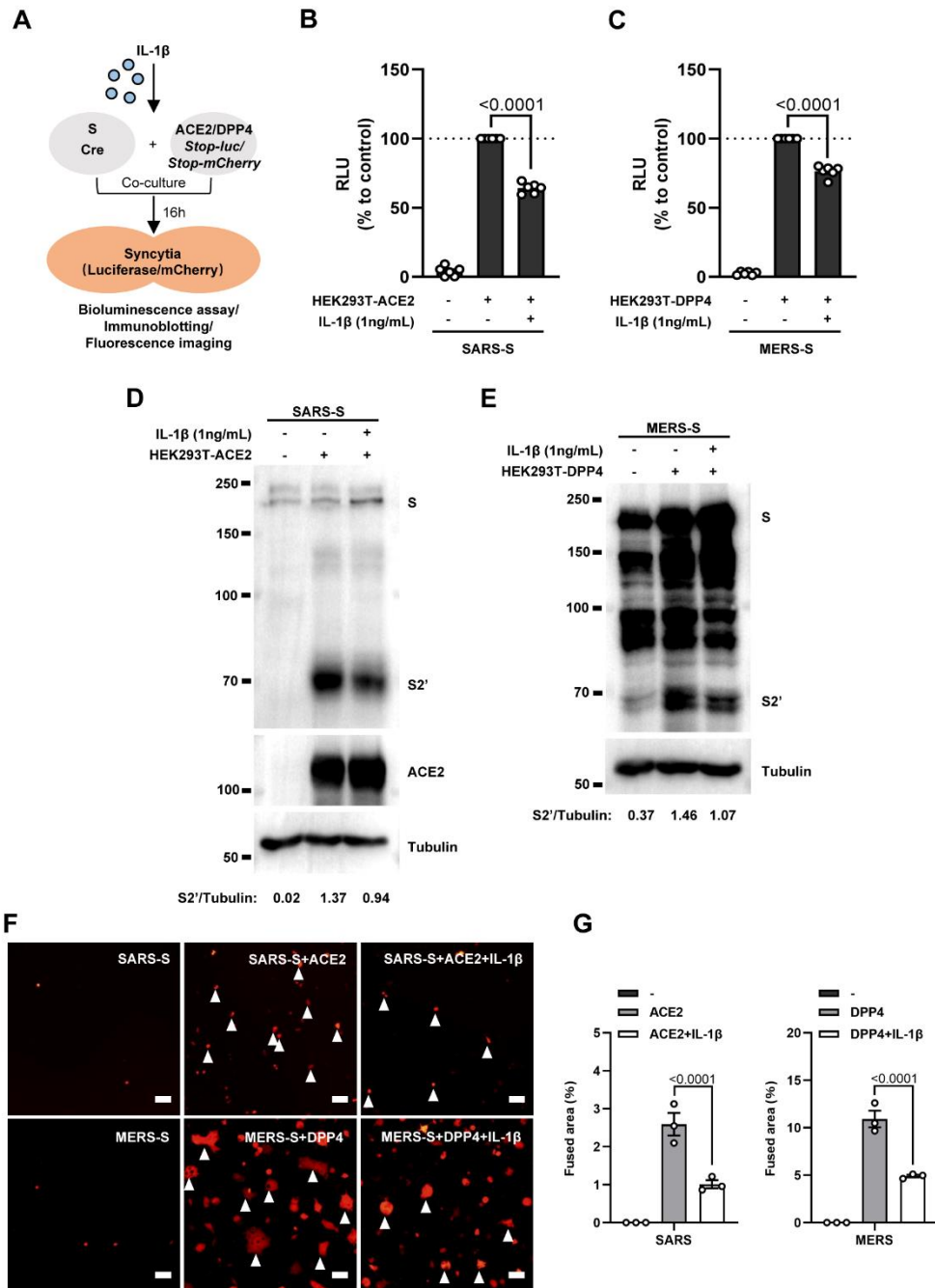
1129
1130
1131

Figure 2—figure supplement 6. IL-1β inhibits SARS-CoV-2 spike-induced syncytia formation in different cells.

1132 (A) Representative fluorescent image captured at 488 nm from HEK293T-S-ZsGreen co-cultured
1133 with HEK293T-ACE2, Vero E6-ACE2 and Calu-3 for 16 hours with or without 1 ng/mL IL-1β.
1134 White arrow heads indicate syncytia formation. Scale bars, 50 μm. Images are representative of
1135 three individual repeats. (B) Quantification of the fused area in (A). (C) Luciferase activity (RLU)
1136 measured from HEK293T cell lysates from 1 ng/mL IL-1β-treated HEK293T-S (S-Alpha, S-Beta,
1137 S-Delta, S-Omicron BA.4) and HEK293T-ACE2 for 16 hours. Data are representative of four
1138 individual repeats and displayed as individual points with mean ±SEM. (D, E) Immunoblots

1139 showing full-length spike, S2, cleaved S2' and ACE2 collected from 1 ng/mL IL-1 β -treated
1140 HEK293T-S (S-Alpha, S-Beta, S-Delta **(D)**, S-Omicron BA.4 **(E)**) and HEK293T-ACE2 for 16
1141 hours. Blots are representative of three independent experiments. Numbers below the blots
1142 indicated the intensity of S2' versus Tubulin.

Figure 2—figure supplement 7



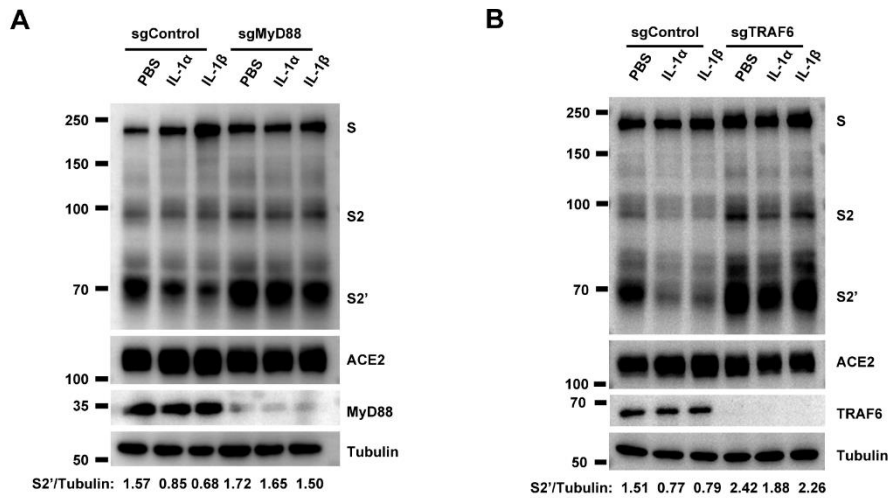
1143
1144
1145

Figure 2—figure supplement 7. IL-1β inhibits SARS-CoV and MERS-CoV spike-induced cell-cell fusion.

1146 (A) Schematics of the cell-cell fusion model used to quantify SARS-CoV and MERS-CoV spike-
1147 mediated syncytia formation upon IL-1β treatment. Cells co-expressing SARS-CoV or MERS-
1148 CoV spike and Cre, were co-cultured with ACE2 or DPP4 and *Stop-luc* co-expressing HEK293T
1149 cells for 16 hours, before cell lysates were collected for bioluminescence assay and
1150 immunoblotting. Cells co-expressing SARS-CoV or MERS-CoV spike and Cre, were co-cultured
1151 with ACE2 or DPP4 and *Stop-mCherry* co-expressing HEK293T cells for 16 hours before

1152 fluorescence imaging. **(B)** Luciferase activity (RLU) measured from HEK293T cell lysates from 1
1153 ng/mL IL-1 β treated HEK293T-S (SARS-S) and HEK293T-ACE2 for 16 hours. Data are
1154 representative of four individual repeats and displayed as individual points with mean \pm SEM. **(C)**
1155 Luciferase activity (RLU) measured from HEK293T cell lysates from 1 ng/mL IL-1 β -treated
1156 HEK293T-S (MERS-S) and HEK293T-DPP4 for 16 hours. Data are representative of four
1157 individual repeats and displayed as individual points with mean \pm SEM. **(D)** Immunoblots showing
1158 SARS-CoV full-length spike, cleaved S2' and ACE2 collected from 1 ng/mL IL-1 β -treated
1159 HEK293T-S (SARS-S) and HEK293T-ACE2 for 16 hours. Blots are representative of three
1160 independent experiments. Numbers below the blots indicated the intensity of S2' versus Tubulin.
1161 **(E)** Immunoblots showing MERS-CoV full-length spike, cleaved S2' collected from 1 ng/mL IL-1 β -
1162 treated HEK293T-S (MERS-S) and HEK293T-DPP4 for 16 hours. Blots are representative of
1163 three independent experiments. Numbers below the blots indicated the intensity of S2' versus
1164 Tubulin. **(F)** Representative fluorescent images captured at 594 nm from 1 ng/mL IL-1 β -treated
1165 HEK293T-S (SARS-S) and HEK293T-ACE2 or HEK293T-S (MERS-S) and HEK293T-DPP4 for
1166 16 hours. White arrow heads indicate syncytia formation. Scale bars, 50 μ m. Images are
1167 representative of three individual experiments. **(G)** Quantification of the fused area in (F).

Figure 3—figure supplement 1



1168

1169

1170

Figure 3—figure supplement 1. IL-1 β inhibits SARS-CoV-2 spike-induced cell-cell fusion through the IL-1R1/MyD88/IRAK/TRAF6 pathway.

1171

1172

1173

1174

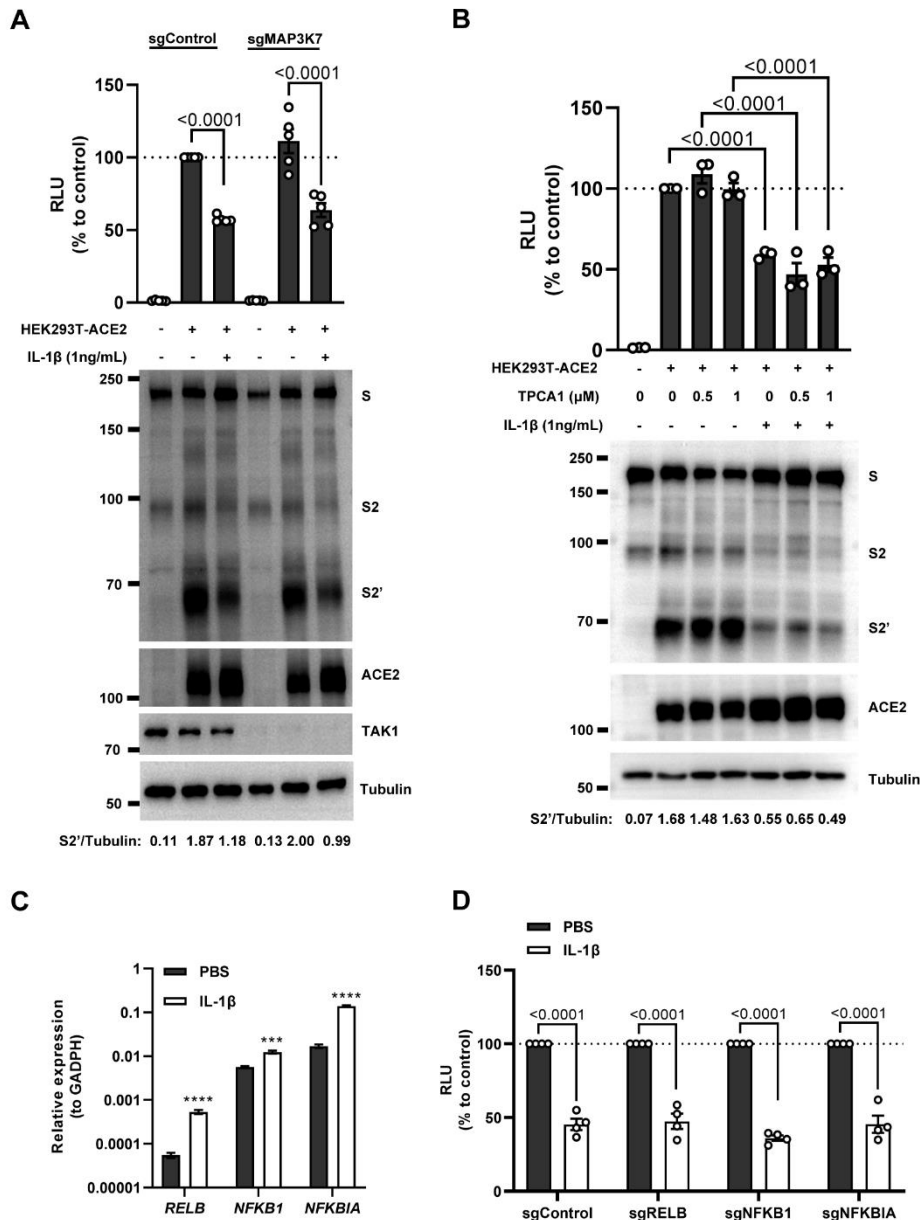
1175

1176

1177

(A) Immunoblots showing full-length spike, S2 and cleaved S2', ACE2 and MyD88 collected from 10 ng/mL IL-1 α or 1 ng/mL IL-1 β treated sgControl or sgMyD88 HEK293T cell-cell fusion system for 16 hours. Blots are representative of three independent experiments. Numbers below the blots indicated the intensity of S2' versus Tubulin. (B) Immunoblots showing full-length spike, S2 and cleaved S2', ACE2 and TRAF6 collected from 10 ng/mL IL-1 α or 1 ng/mL IL-1 β treated sgControl or sgTRAF6 HEK293T cell-cell fusion system for 16 hours. Blots are representative of three independent experiments. Numbers below the blots indicated the intensity of S2' versus Tubulin.

Figure 3—figure supplement 2



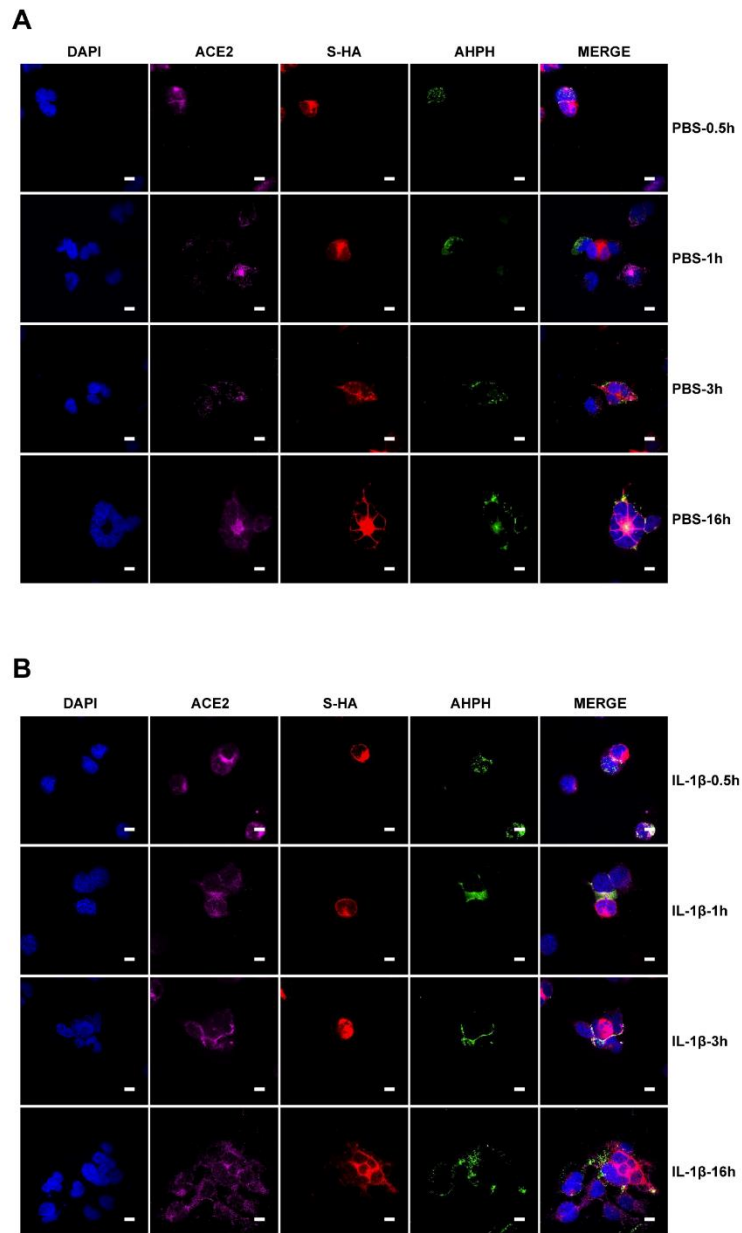
1178

1179 **Figure 3—figure supplement 2. IL-1β inhibits SARS-CoV-2 spike-induced cell-cell fusion**
 1180 **independent from the TAK1/IKKβ/NF-κB pathway.**

1181 (A) Luciferase activity (RLU) measured from cell lysates and immunoblots showing full-length
 1182 spike, S2 and cleaved S2', ACE2 collected from 1 ng/mL IL-1β treated sgControl or sgTAK1
 1183 HEK293T cell-cell fusion system for 16 hours. Data and blots are representative of five individual
 1184 repeats. Numbers below the blots indicated the intensity of S2' versus Tubulin. (B) Luciferase
 1185 activity (RLU) measured from HEK293T cell lysates and immunoblots showing full-length spike,
 1186 S2 and cleaved S2', ACE2 collected from HEK293T-S and HEK293T-ACE2 pre-treated with
 1187 different concentrations of TPCA1 for 30 min, then treated with 1 ng/mL IL-1β for 16 hours. Data
 1188 and blots are representative of three individual repeats. Numbers below the blots indicated the

1189 intensity of S2' versus Tubulin. **(C)** mRNA levels of NF- κ B pathway-related genes in HEK293T
1190 cells after 1 ng/mL IL-1 β for 4 hours. Data are representative of three individual repeats. **(D)**
1191 Luciferase activity (RLU) measured from cell lysates collected from 1 ng/mL IL-1 β -treated
1192 sgControl, sgRELB, sgNFKB1 or sgNFKBIA HEK293T cell-cell fusion system for 16 hours. Data
1193 are representative of four individual repeats and displayed as individual points with mean \pm SEM.

Figure 4—figure supplement 1



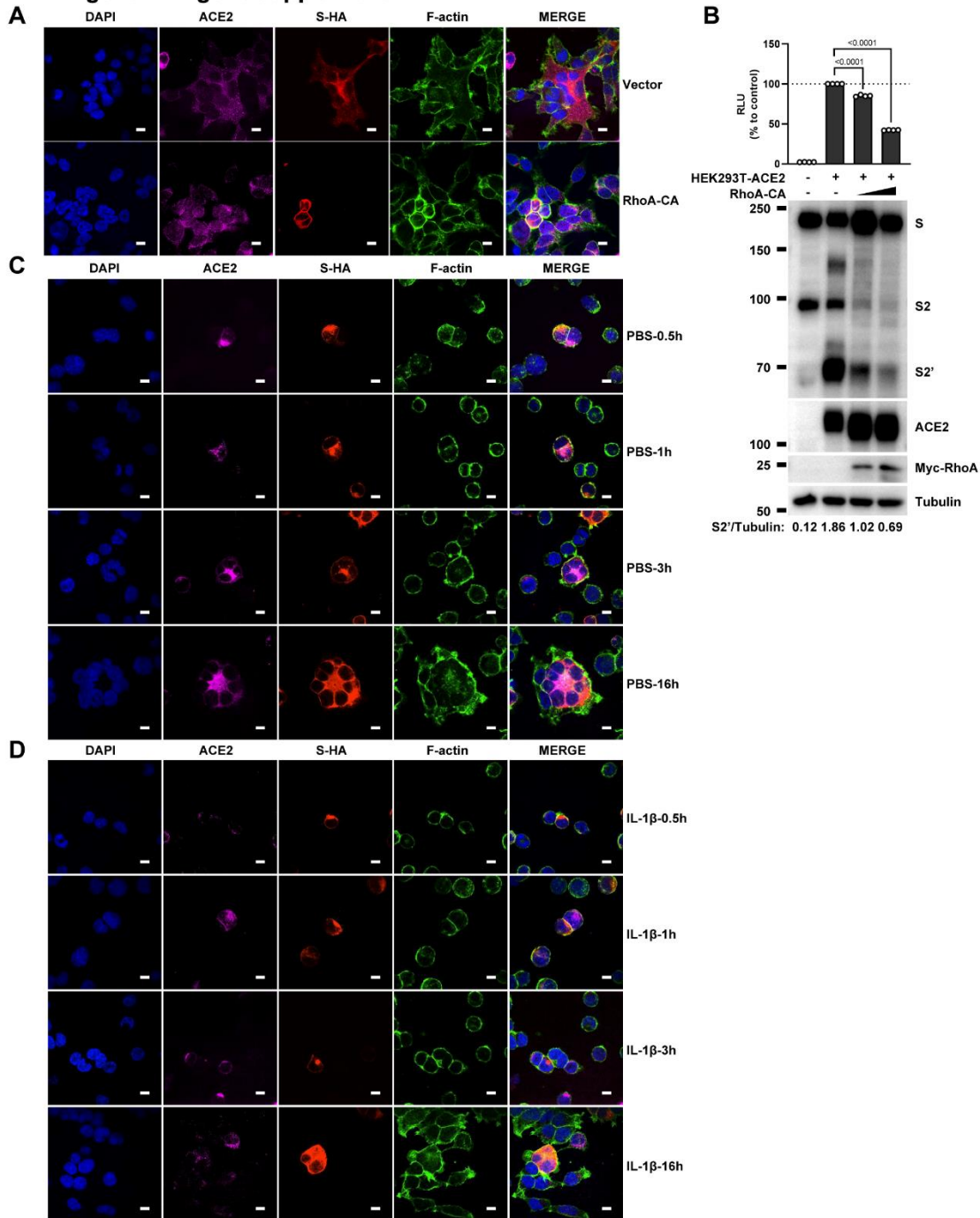
1194
1195

Figure 4—figure supplement 1. Single-channel confocal images.

1196
1197

(A) Single-channel confocal images of Figure 4D top panel. **(B)** Single-channel confocal images of Figure 4D bottom panel.

Figure 4—figure supplement 2



1198
1199

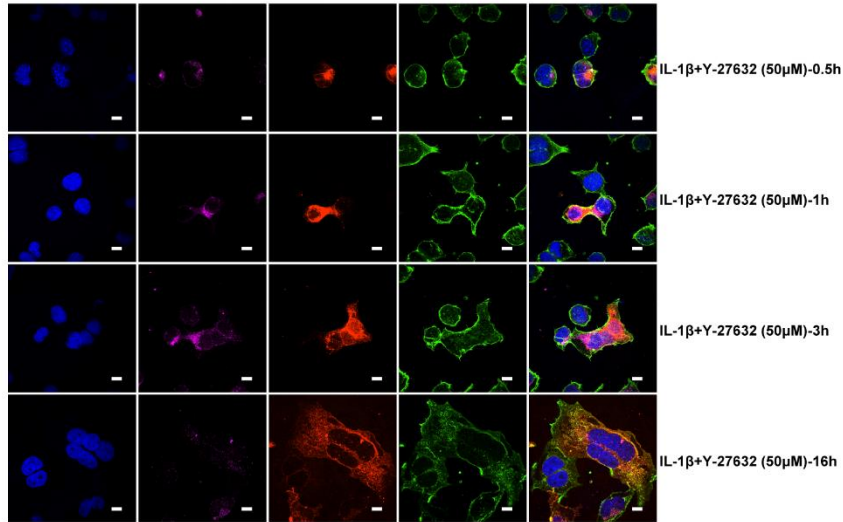
Figure 4—figure supplement 2. Single-channel confocal images.

1200 (A) Single-channel confocal images of Figure 4E. (B) Luciferase activity (RLU) measured from
1201 HEK293T cell lysates and immunoblots showing full-length spike, S2, cleaved S2', ACE2 and
1202 Myc-RhoA collected from transfected vector, 10 ng or 20 ng constitutively active RhoA mutant
1203 (RhoA-CA) both in HEK293T-S and HEK293T-ACE2 cells. Data and blots are representative of
1204 four individual repeats. Numbers below the blots indicated the intensity of S2' versus Tubulin. (C)
1205 Single-channel confocal images of Figure 4F top panel. (D) Single-channel confocal images of
1206 Figure 4F middle panel.

1207

Figure 4—figure supplement 3

A



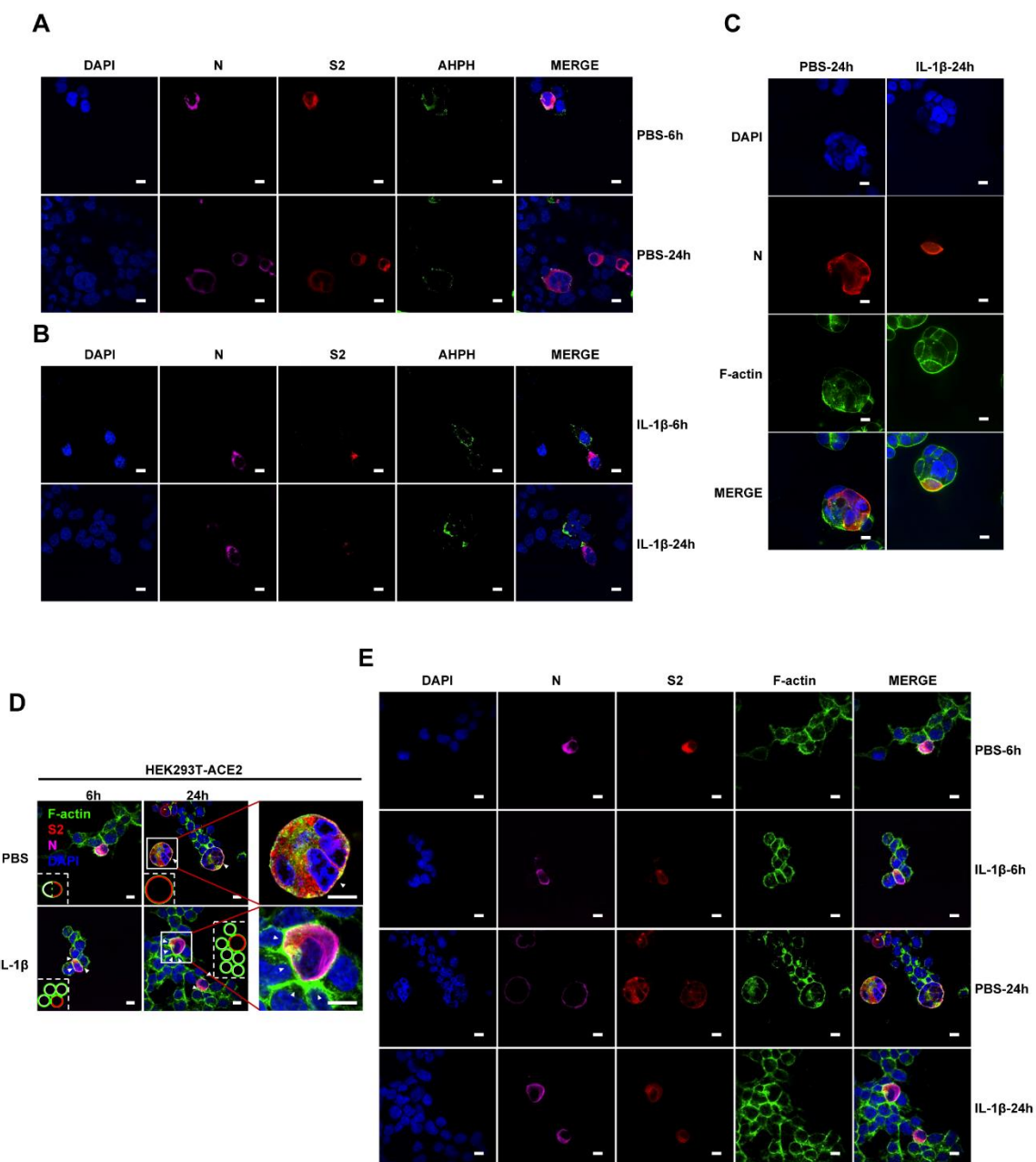
1208

1209 **Figure 4—figure supplement 3. Single-channel confocal images.**

1210 **(A)** Single-channel confocal images of Figure 4F bottom panel.

1211

Figure 5—figure supplement 1



1212

1213

Figure 5—figure supplement 1. Single-channel confocal images.

1214

1215

1216

1217

1218

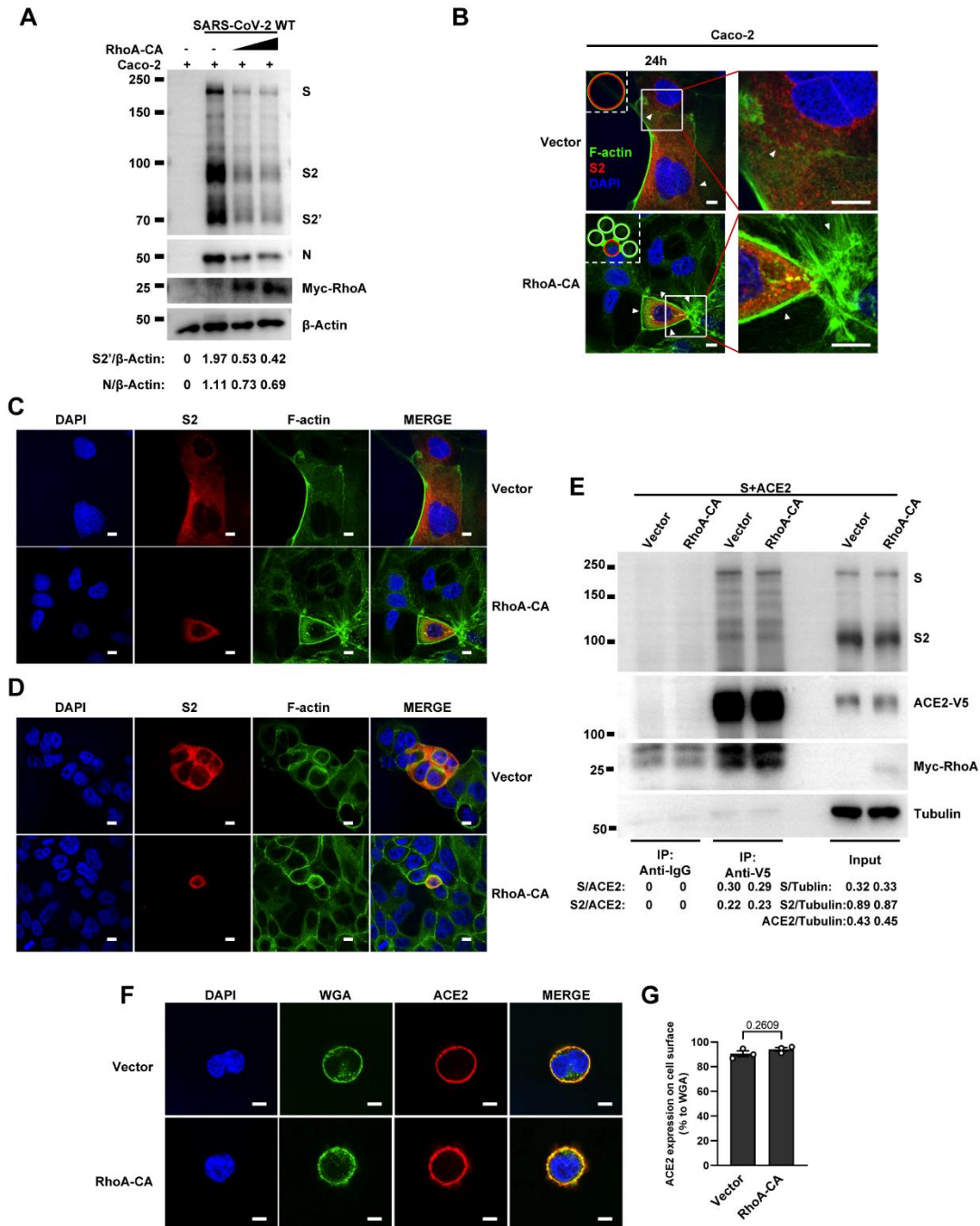
(A) Single-channel confocal images of Figure 5A top panel. (B) Single-channel confocal images of Figure 5A bottom panel. (C) Single-channel confocal images of Figure 5B. (D) Representative confocal images of F-actin stained with phalloidin-488 in the presence or absence of 1 ng/mL IL-1β treatment in 0.5 MOI WT authentic SARS-CoV-2 infected HEK293T-ACE2 cells at 6 or 24 hpi. Schematics with green lines in the white dashed line boxes representing actin bundles, red cycles

56

1219 representing SARS-CoV-2 infected cells, and white cycles representing neighboring cells. White
1220 arrow heads indicate the enrichment or disappearance of F-actin, scale bars, 10 μm . Images are
1221 representative of four independent experiments. **(E)** Single-channel confocal images of **(D)**.

1222

Figure 5—figure supplement 2



1223
1224
1225

Figure 5—figure supplement 2. RhoA-CA does not affect Spike protein binding to ACE2 or ACE2 distribution on the cell surface.

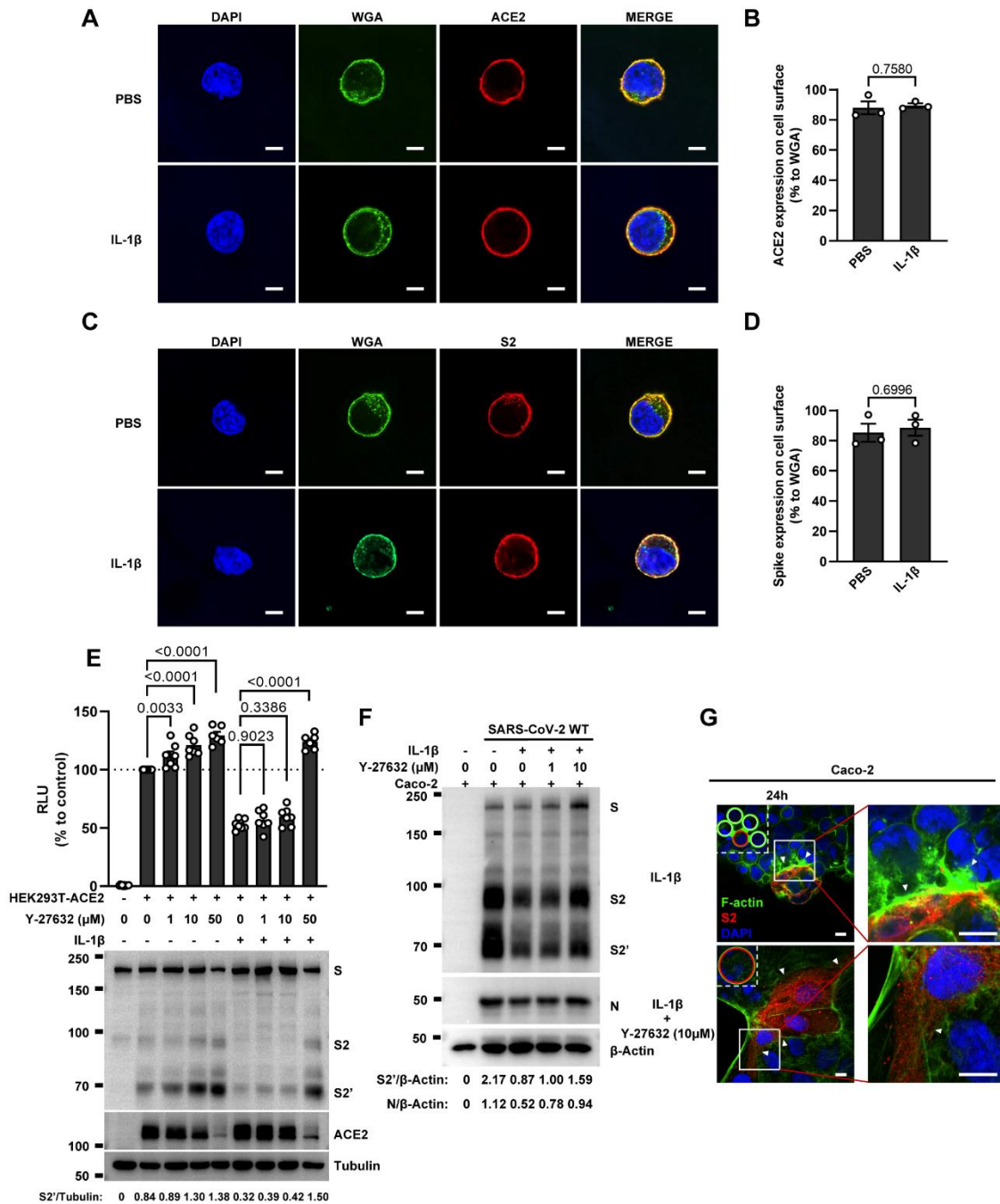
1226 (A) Immunoblots of WT SARS-CoV-2 S, S2, cleaved S2', N and Myc-RhoA collected from Caco-2
1227 cells, which were transfected with vector, 10 ng or 20 ng RhoA-CA before infection with 0.5 MOI
1228 WT authentic SARS-CoV-2 for 24 hours. Blots are representative of three individual experiments.
1229 Numbers below the blots indicated the intensity of S2' or N versus β -Actin. (B) Representative

58

1230 confocal images of F-actin stained with phalloidin-488 from Caco-2 cells described in (A).
1231 Schematics with green lines in the white dashed line boxes representing actin bundles, red circles
1232 representing S-expressing cells. White arrow heads indicate the enrichment or disappearance of
1233 F-actin, scale bars, 10 μm . Images are representative of four independent experiments. **(C)**
1234 Single-channel confocal images of (B). **(D)** Single-channel confocal images of Figure 5E. **(E)** Co-
1235 immunoprecipitation (IP) and input controls of full-length spike protein after anti-V5 or anti-IgG
1236 pulldown from cell lysates mixed between HEK293T cells expressing ACE2-V5-6his or Spike
1237 protein with vector or RhoA-CA (10 ng). Blots are representative of three individual experiments.
1238 Numbers below the blots indicated the intensity of S or S2 versus ACE2 in IP group and S, S2 or
1239 ACE2 versus Tubulin in input group. **(F)** Representative confocal images of Wheat Germ
1240 Agglutinin (WGA, cell surface marker) and ACE2 from HEK293T cells co-transfected with ACE2
1241 and vector or RhoA-CA (10 ng). Scale bars, 10 μm . Images are representative of three
1242 independent experiments. **(G)** Quantification of the relative ACE2 expression on the cell surface
1243 in (F).

1244

Figure 5—figure supplement 3



1245
1246
1247

Figure 5—figure supplement 3. IL-1β does not affect ACE2 and Spike distribution on the cell surface.

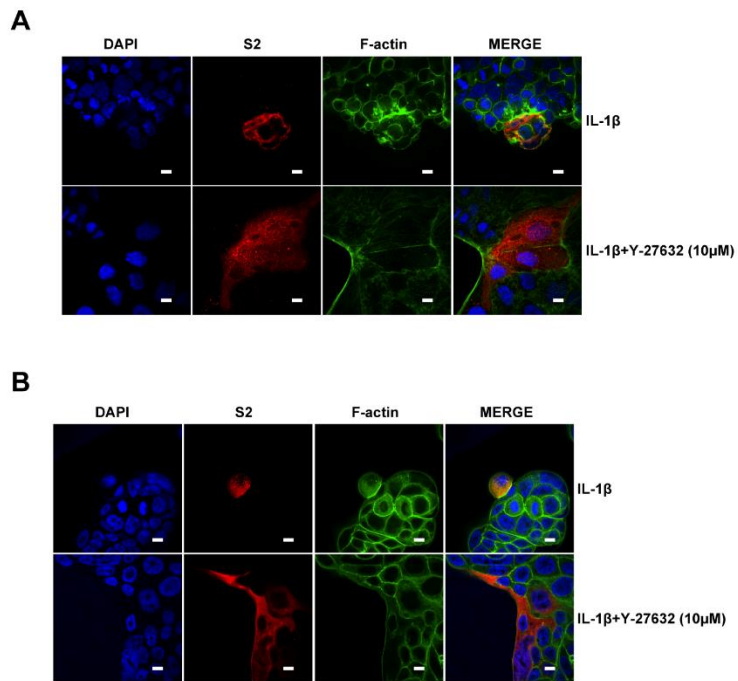
1248
1249
1250
1251

(A) Representative confocal images of Wheat Germ Agglutinin (WGA) and ACE2 from HEK293T cells transfected with ACE2 and treated with PBS or IL-1β. Scale bars, 10 μm. Images are representative of three independent experiments. (B) Quantification of the relative ACE2 expression on the cell surface in (A). (C) Representative confocal images of WGA and Spike from

1252 HEK293T cells transfected with Spike and treated with PBS or IL-1 β . Scale bars, 10 μ m. Images
1253 are representative of three independent experiments. **(D)** Quantification of the relative Spike
1254 expression on the cell surface in (C). **(E)** Luciferase activity (RLU) measured from HEK293T cell
1255 lysates and immunoblots showing full-length spike, S2 and cleaved S2', ACE2 collected from
1256 HEK293T-S and HEK293T-ACE2 pre-treated with different concentrations of Y-27632 for 30 min,
1257 then treated with 1 ng/mL IL-1 β for 16 hours. Data and blots are representative of three
1258 independent experiments. Numbers below the blots indicated the intensity of S2' versus Tubulin.
1259 **(F)** Immunoblots of WT SARS-CoV-2 S, S2, cleaved S2' and N collected from Caco-2 cells, which
1260 were treated with different concentrations of Y-27632 and 10 ng/mL IL-1 β for 1 hour, then
1261 infected with 0.5 MOI WT authentic SARS-CoV-2 for 24 hours. Blots are representative of three
1262 individual experiments. Numbers below the blots indicated the intensity of S2' or N versus β -
1263 Actin. **(G)** Representative confocal images of F-actin stained with phalloidin-488 in Caco-2 cells
1264 described in (F). Schematics with green lines in the white dashed line boxes representing actin
1265 bundles, red cycles representing S-expressing cells. White arrow heads indicate the enrichment
1266 or disappearance of F-actin, scale bars, 10 μ m. Images are representative of four independent
1267 experiments.

1268

Figure 5—figure supplement 4



1269

1270

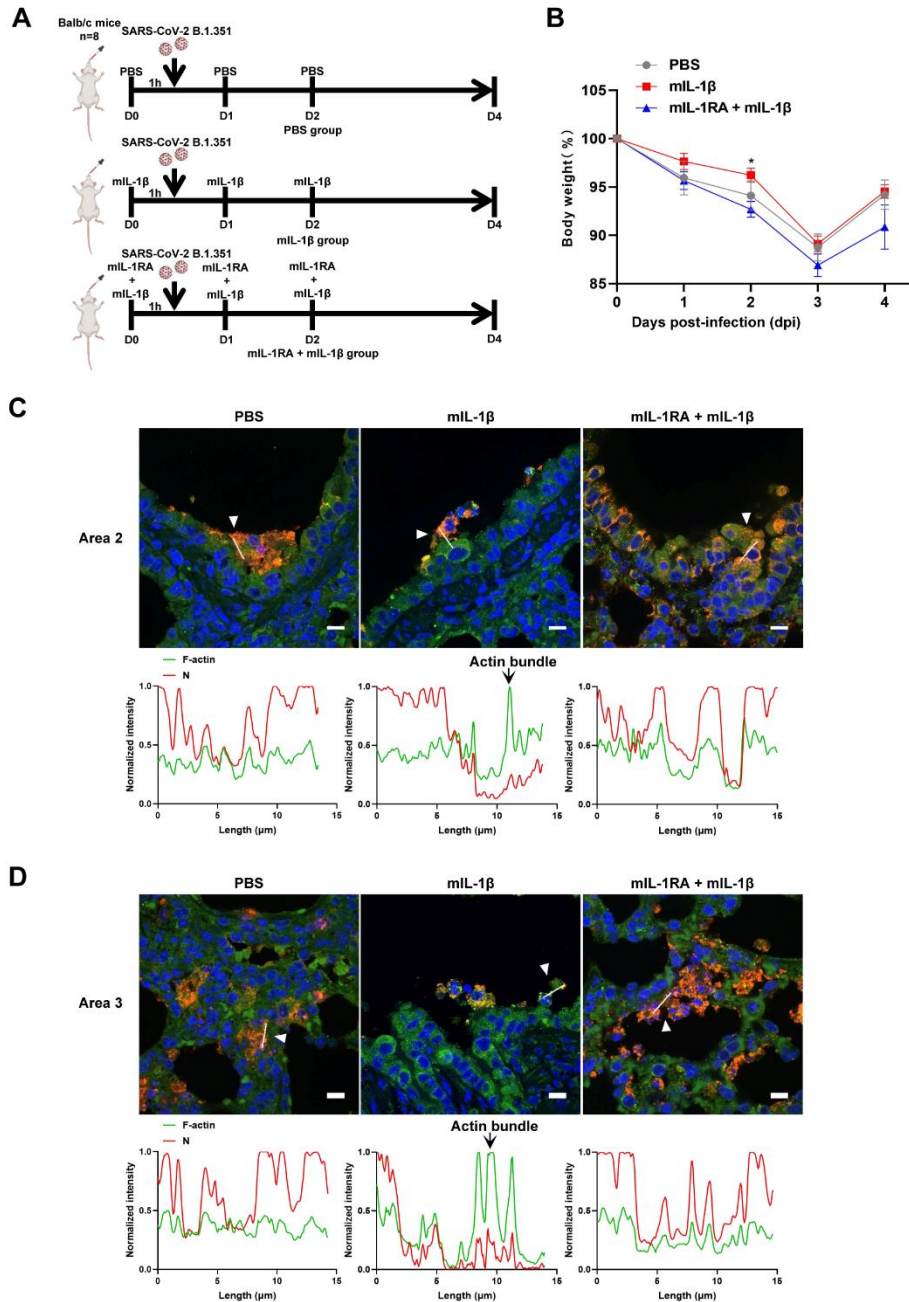
Figure 5—figure supplement 4. Single-channel confocal images.

1271

1272

(A) Single-channel confocal images of Figure 5—figure supplement 3G. (B) Single-channel confocal images of Figure 5H.

Figure 6—figure supplement 1



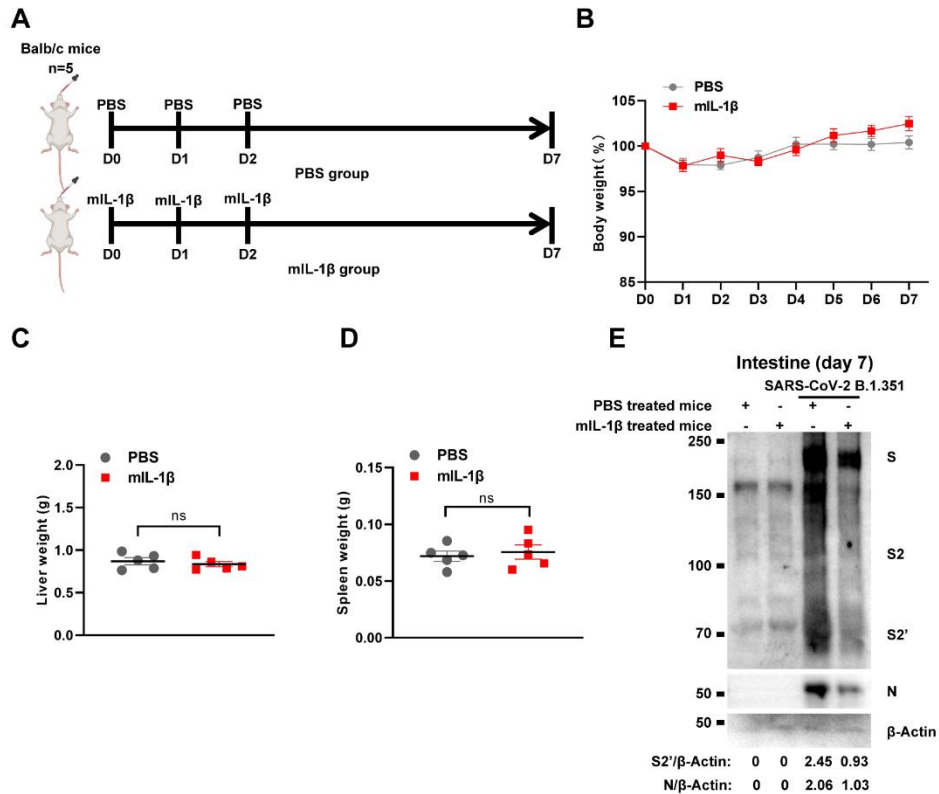
1273
1274
1275

Figure 6—figure supplement 1. IL-1 β reduces the weight loss and viral transmission upon SARS-CoV-2 infection *in vivo*.

1276 (A) Schematic for a murine model of authentic SARS-CoV-2 infection, PBS control (n=8); 1 μ g/kg
1277 mL-1 β (n=8); 150 μ g/kg mL-1RA + 1 μ g/kg mL-1 β (n=8) were administered 1 hour before
1278 intranasal challenge with 5×10^4 FFU of SARS-CoV-2 B.1.351; mice were then intraperitoneal
1279 injection with PBS, mL-1 β and mL-1RA + mL-1 β at 1 dpi and 2 dpi, before sacrificed at 4 dpi. (B)
1280 The body weights were assessed daily for weight loss after SARS-CoV-2 infection. (C, D)
1281 Representative confocal images of F-actin stained with phalloidin-488 and SARS-CoV-2 N in the

1282 area 2 and area 3 of lung tissue at 4 dpi. White arrow heads indicate syncytia formation or
1283 infected cells, scale bars are indicative of 10 μm and images are representative of three samples
1284 (Top). White lines indicate SARS-CoV-2 cell-cell transmission and quantify with fluorescence
1285 intensity of F-actin and SARS-CoV-2 N (Bottom).
1286

Figure 6—figure supplement 2

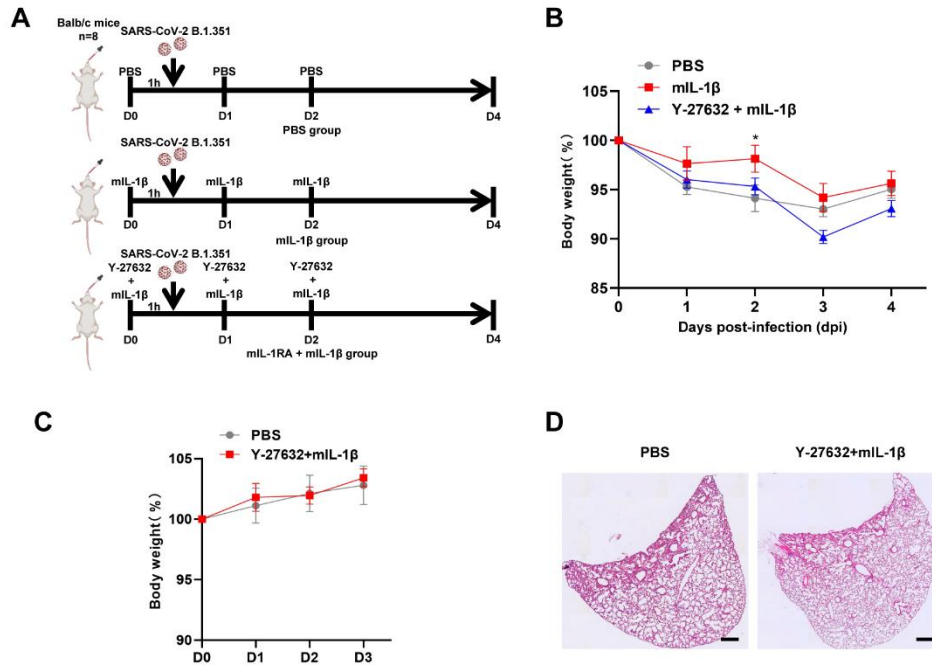


1287
1288
1289

Figure 6—figure supplement 2. Treatment with 1 µg/kg mL-1β protects mouse lung and intestinal tissue cells against SARS-CoV-2 infection without toxicity *in vivo*.

1290 (A) Schematic of PBS (n=5) and mL-1β (n=5) treated BALB/c mice. (B) The body weights were
1291 assessed daily for weight loss. Liver (C) and spleen (D) weights were assessed at day 7. (E)
1292 Immunoblots of SARS-CoV-2 S, S2, cleaved S2' and N proteins collected from SARS-CoV-2
1293 B.1.351 infected intestine tissue cells, which isolated from BALB/c mice treated with or without 1
1294 µg/kg mL-1β at day 7. Blots are representative of three individual mouse. Numbers below the
1295 blots indicated the intensity of S2' or N versus β-Actin.

Figure 7—figure supplement 1

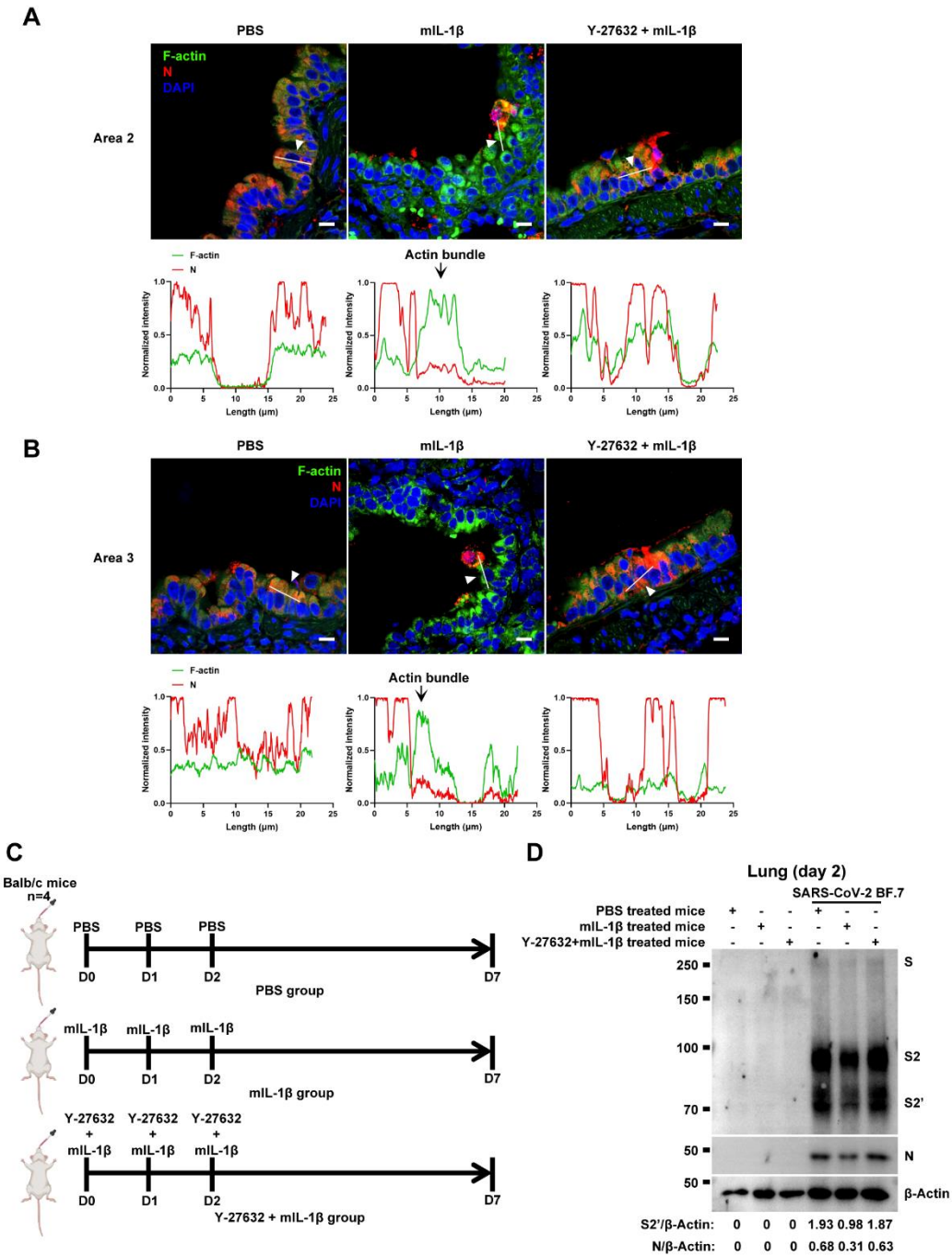


1296
1297
1298

Figure 7—figure supplement 1. Y-27632+IL-1β do not cause weight loss and lung injury in uninfected BALB/c mice.

1299 (A) Schematic for a murine model of authentic SARS-CoV-2 infection, PBS control (n=8); 1 μg/kg
1300 mL-1β (n=8); 1mg/kg Y-27632 + 1 μg/kg mL-1β (n=8) were administered 1 hour before
1301 intranasal challenge with 5×10^4 FFU of SARS-CoV-2 B.1.351; mice were then intraperitoneal
1302 injection with PBS, mL-1β and Y-27632 + mL-1β at 1 dpi and 2 dpi, before sacrificed at 4 dpi. (B)
1303 The body weights were assessed daily for weight loss after SARS-CoV-2 infection. (C) The body
1304 weights were assessed daily from PBS or Y-27632 + mL-1β treated uninfected mice. (D)
1305 Representative images of H&E-stained lung sections from PBS or Y-27632 + mL-1β-treated
1306 uninfected mice at day7, scale bars are indicative of 500 μm and images are representative of
1307 four samples.

Figure 7—figure supplement 2



1308
1309
1310

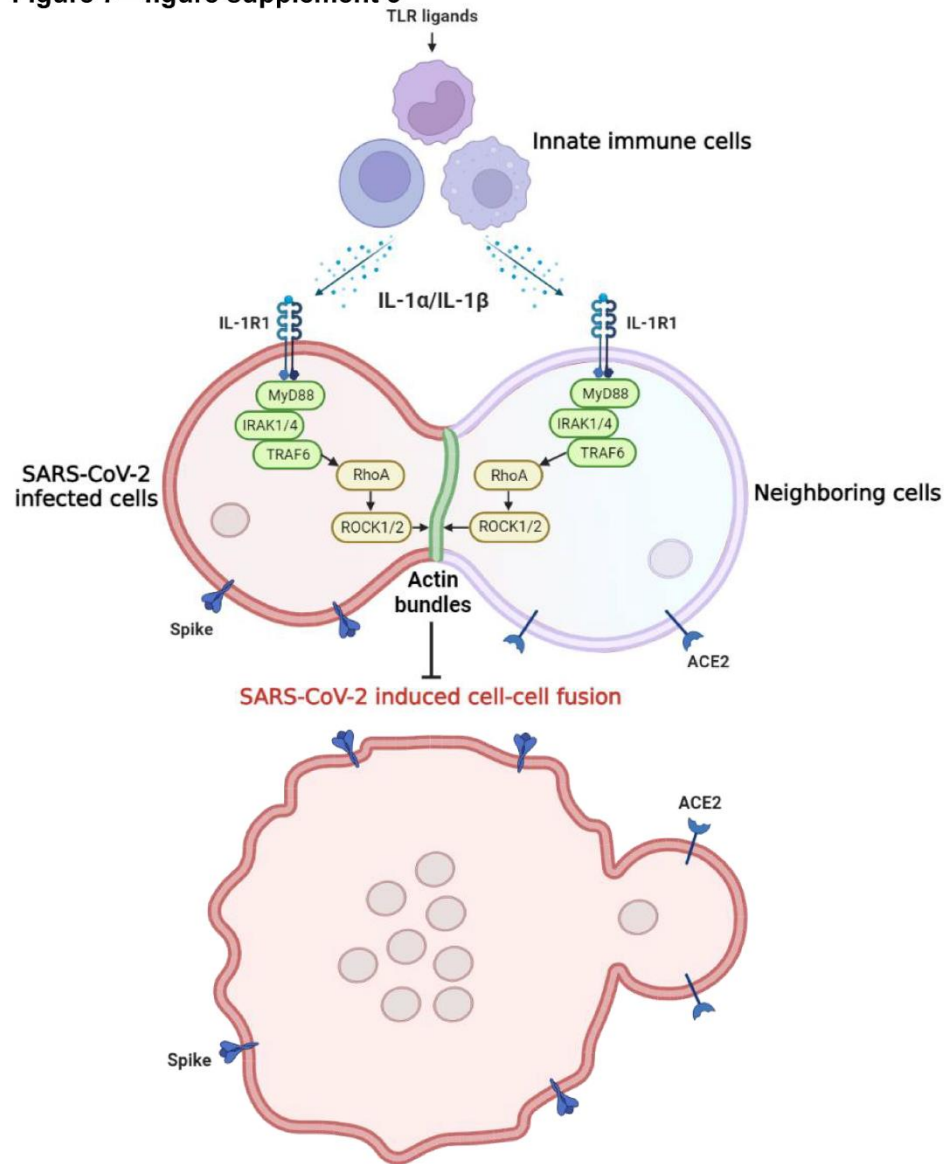
Figure 7—figure supplement 2. Y-27632 treatment prevents the formation of IL-1β-induced actin bundles at cell-cell junctions *in vivo*.

1311
1312
1313
1314
1315
1316

(A, B) Representative confocal images of F-actin stained with phalloidin-488 and SARS-CoV-2 N in the area 2 and area 3 of lung tissue at 4 dpi. White arrow heads indicate syncytia formation or infected cells, scale bars are indicative of 10 μm and images are representative of three samples (Top). White lines indicate SARS-CoV-2 cell-cell transmission and quantify with fluorescence intensity of F-actin and SARS-CoV-2 N (Bottom). (C) Schematic of PBS, mL-1β and Y-27632 + mL-1β treated BALB/c mice. (D) Immunoblots of SARS-CoV-2 S, S2, cleaved S2' and N proteins

1317 collected from authentic SARS-CoV-2 BF.7 infected lung tissue cells, which were isolated from
1318 BALB/c mice treated with PBS, 1 µg/kg mL-1β or 1mg/kg Y-27632 + 1 µg/kg mL-1β at day 2.
1319 Blots are representative of three individual mouse. Numbers below the blots indicated the
1320 intensity of S2' or N versus β-Actin.

Figure 7—figure supplement 3



1321
1322

Figure 7—figure supplement 3. Graphical abstract.

1323 Host factors secreted from innate immune cells upon TLR ligands stimulation, including
1324 interleukin-1 β (IL-1 β) and IL-1 α , act on both SARS-CoV-2 infected cells expressing spike protein
1325 and neighboring cells expressing ACE2 receptor via IL-1R1-MyD88-IRAK-TRAF6 signaling
1326 pathway, which leads to strong enrichment of activated RhoA at cell-cell junction, resulting in the
1327 formation of ROCK-mediated actin bundle to prevent SARS-CoV-2 induced cell-cell fusion and
1328 further viral transmission through syncytia formation.

1329 **Table S1. Primer sequences for RT-qPCR.**

Gene	Forward 5'-3'	Reverse 5'-3'
<i>IL1A</i>	CAGCCAGAGAGGGAGTCATTT	TGTCTGGAAC TTTGGCCATCTT
<i>IL1B</i>	CAGAAGTACCTGAGCTCGCC	AGATTCGTAGCTGGATGCCG
<i>IL4</i>	CTTTGCTGCCTCCAAGAACACA	GAACTGCCGGAGCACAGTC
<i>IL6</i>	CCACCGGGAACGAAAGAGAA	GAGAAGGCAACTGGACCGAA
<i>IL8</i>	ACTCCAAACCTTTCCACCCC	TTCTCAGCCCTCTTCAAAACTT
<i>IL12A</i>	CTCCAGAAGGCCAGACAAACTC	AGGCCAGGCAACTCCCATTAG
<i>IFNA1</i>	TGACTCATACACCAGGTCACG	GGTCATAGTTATAGCAGGGGTGA
<i>IFNA2</i>	CTTGTGCCTGGGAGGTTGTC	AGGTGAGCTGGCATAACGAATC
<i>IFNB1</i>	GGCACAAACAGGTAGTAGGCG	GAGAAGCACAAACAGGAGAGC
<i>IFNG</i>	AGCCAACCTAAGCAAGATCCC	TGCCATTAAGCACTGGCTC
<i>IL1R1</i>	GGTAGACGCACCCTCTGAAG	TCAGCCTCCAGAGAAGAAATCA
<i>IL2RA</i>	AGGGCTCTACACAGAGGTCC	GTGACGAGGCAGGAAGTCTC
<i>IL4R</i>	AAAACGACCCGGCAGATTTT	GGCTCCCTGTAGGAGTTGTG
<i>IL6ST</i>	ACAGCATCCAGTGTACCTTT	TCCCCTCGTTCACAATGCAA
<i>IL8RA</i>	AGTTCTTGGCACGTCATCGT	CCCCTGAAGACACCAGTTCC
<i>IL12RB1</i>	TTCAGCATCGAAGTGCAGGT	TTCAGGCCAAGGTAGCCAAG
<i>IFNAR1</i>	TGTAAGTGGTGGGATCTGCG	ACTCATCGCTCCTGTTCCAC
<i>IFNGR1</i>	TAGCAGCATGGCTCTCCTCTTTC	AGTTGGTGTAGGCACTGAGGAC
<i>RELB</i>	GATCGTCCACCAGACCGTG	GAAACGGCGAGCGAGAGT
<i>NFKB1</i>	TTTGGGAAGGCCTGAACAAATG	GGGATGGCCTTCACATACA
<i>NFKBIA</i>	TGTGCTTCGAGTGACTGACC	TCACCCACATCACTGAACG
SARS-CoV-2-N	GGGGAAC T TCTCCTGCTAGAAT	CAGACATTTTGCTCTCAAGCTG
<i>GAPDH</i>	CGGGAAGGAAATGAATGGGC	GGAAAAGCATCACCCGGAGG

1330

1331 **Table S2. Primer sequences for sgRNA.**

Gene	sgRNA
<i>TLR2</i>	TGGAAACGTTAACAATCCGG
<i>MyD88</i>	GGGGATCAGTCGCTTCTGAT
<i>TRAF6</i>	GAAGCAGTGCAAACGCCATG
<i>MAP3K7</i>	GATCGACTACAAGGAGATCG
<i>RELB</i>	GGGCGGCGTCTTGAACACAA
<i>NFKB1</i>	GTCACTCTAACGTATGCAAC
<i>NFKBIA</i>	CTGGACGACCGCCACGACAG

1332

1333